Implementation of nitrogen cycle in the CLASSIC land model

Ali Asaadi and Vivek. K. Arora

Canadian Centre for Climate Modelling and Analysis, Environment Canada, University of Victoria, Victoria, B.C., V8W 2Y2, Canada

1   **Abstract**

3   A terrestrial nitrogen (N) cycle model is coupled to carbon (C) cycle in the framework of the Canadian Land

4   Surface Scheme Including biogeochemical Cycles (CLASSIC). CLASSIC currently models physical and

5   biogeochemical processes and simulates fluxes of water, energy, and CO_2 at the land-atmosphere

6   boundary. Similar to most models, gross primary productivity in CLASSIC increases in response to

7   increasing atmospheric CO_2 concentration. In the current model version, a downregulation

8   parameterization emulates the effect of nutrient constraints and scales down potential photosynthesis

9   rates, using a globally constant scalar, as a function of increasing CO_2. In the new model when nitrogen

10 (N) and carbon (C) cycles are coupled, cycling of N through the coupled soil-vegetation system facilitates

11 the simulation of leaf N content and maximum carboxylation capacity (V_{cmax}) prognostically. An increase

12 in atmospheric CO_2 decreases leaf N content, and therefore V_{cmax}, allowing the simulation of

13 photosynthesis downregulation as a function of N supply. All primary N cycle processes, that represent

14 the coupled soil-vegetation system, are modelled explicitly. These include biological N fixation, treatment

15 of externally specified N deposition and fertilization application, uptake of N by plants, transfer of N to

16 litter via litterfall, mineralization, immobilization, nitrification, denitrification, ammonia volatilization,

17 leaching, and the gaseous fluxes of NO, N_2O, and N_2. The interactions between terrestrial C and N cycles

18 are evaluated by perturbing the coupled soil-vegetation system in CLASSIC with one forcing at a time over

19 the 1850-2017 historical period. These forcings include the increase in atmospheric CO_2, change in

20 climate, increase in N deposition, and increasing crop area and fertilizer input, over the historical period.

21 Increase in atmospheric CO_2 increases the C:N ratio of vegetation; climate warming over the historical

22 period increases N mineralization and leads to a decrease in vegetation C:N ratio; N deposition also

23 decreases vegetation C:N ratio; and fertilizer input increases leaching, NH_3 volatilization, and gaseous

24 losses of N_2, N_2O, and NO. These model responses are consistent with conceptual understanding of the

25 coupled C and N cycles. The simulated terrestrial carbon sink over the 1959-2017 period, from the

26 simulation with all forcings, is 2.0 Pg C/yr and compares reasonably well with the quasi observation-based

27 estimate from the 2019 Global Carbon Project (2.1 Pg C/yr). The contribution of increasing CO_2, climate

28 change, and N deposition to carbon uptake by land over the historical period (1850-2017) is calculated to

29 be 84%, 2%, and 14%, respectively.

1. Introduction

The uptake of carbon (C) by land and ocean in response to the increase in anthropogenic fossil fuel emissions of CO_2 has served to slow down the growth rate of atmospheric CO_2 since the start of the industrial revolution. At present, about 55% of total carbon emitted into the atmosphere is taken up by land and ocean (Le Quéré et al., 2018; Friedlingstein et al., 2019). It is of great policy, societal, and scientific relevance whether land and ocean will continue to provide this ecosystem service. Over land, as long as photosynthesis is not water limited, the uptake of carbon in response to increasing anthropogenic CO_2 emissions is driven by two primary factors, 1) the CO_2 fertilization of the terrestrial biosphere, and 2) the increase in temperature, both of which are associated with increasing $[CO_2]$. The CO_2 fertilization effect increases photosynthesis rates for about 80% of the world's vegetation that uses the C_3 photosynthetic pathway and is currently limited by $[CO_2]$ (Still et al., 2003; Zhu et al., 2016). The remaining 20% of vegetation uses the C_4 photosynthetic pathway that is much less sensitive to $[CO_2]$. Warming increases carbon uptake by vegetation in mid-high latitude regions where growth is currently limited by low temperatures (Zeng et al., 2011).

Even when atmospheric CO_2 is not limiting for photosynthesis, and near surface air temperature is optimal, vegetation cannot photosynthesize at its maximum possible rate if available water and nutrients (most importantly nitrogen (N) and phosphorus (P)) constrain photosynthesis (Vitousek and Howarth, 1991; Reich et al., 2006b). In the absence of water and nutrients, photosynthesis simply cannot occur. N is a major component of chlorophyll (the compound through which plants photosynthesize) and amino acids (that are the building blocks of proteins). The constraint imposed by available water and nutrients implies that the carbon

53 uptake by land over the historical period in response to increasing [CO_2] is lower than what it

54 would have been if water and nutrients were not limiting. This lower than maximum theoretically

55 possible rate of increase of photosynthesis in response to increasing atmospheric CO_2 is referred

56 to as downregulation (Faria et al., 1996; Sanz-Sáez et al., 2010). Typically, however, the term

57 downregulation of photosynthesis is used only in the context of nutrients and not water.

58 Downregulation is defined as a decrease in photosynthetic capacity of plants grown at elevated

59 CO_2 in comparison to plants grown at baseline CO_2 (McGuire et al., 1995). However, despite the

60 decrease in photosynthetic capacity, the photosynthesis rate for plants grown at elevated CO_2 is

61 still higher than the rate for plants grown and measured at baseline CO_2 because of higher

62 background CO_2.

63   Earth system models (ESMs) that explicitly represent coupling of the global carbon cycle

64 and physical climate system processes are the only tools available at present that, in a physically

65 consistent way, are able to project how land and ocean carbon cycles will respond to future

66 changes in [CO_2]. Such models are routinely compared to one another under the auspices of the

67 Coupled Model Intercomparison Project (CMIP) every 6-7 years. The most recent and sixth phase

68 of CMIP (CMIP6) is currently underway (Eyring et al., 2016). Interactions between carbon cycle

69 and climate in ESMs have been compared under the umbrella of the Coupled Climate-Carbon

70 Cycle Model Intercomparison Project (C^4MIP) (Jones et al., 2016) which is an approved MIP of

71 the CMIP. Comparison of land and ocean carbon uptake in C^4MIP studies (Friedlingstein et al.,

72 2006; Arora et al., 2013, 2020) indicate that the inter-model uncertainty in future land carbon

73 uptake across ESMs is more than three times than the uncertainty for the ocean carbon uptake.

74 The reason for widely varying estimates of future land carbon uptake across models is that our

75 understanding of biological processes that determine land carbon uptake is much less advanced

76 than the physical processes which primarily determine carbon uptake over the ocean. In the

77 current generation of terrestrial ecosystem models, other than photosynthesis for which a

78 theoretical framework exists, almost all of the other biological processes are represented on the

79 basis of empirical observations and parameterized in one way or another. In addition, not all

80 models include N and P cycles. In the absence of an explicit representation of nutrient constraints

81 on photosynthesis, land models in ESMs parameterize downregulation of photosynthesis in other

82 ways that reduce the rate of increase of photosynthesis to values below its theoretically

83 maximum possible rate, as [CO_2] increases (e.g., Arora et al., 2009). Comparison of models across

84 5th and 6th phase of CMIP shows that the fraction of models with land N cycle is increasing (Arora

85 et al., 2013, 2020).

86   The nutrient constraints on photosynthesis are well recognized (Vitousek and Howarth,

87 1991; Arneth et al., 2010). Terrestrial carbon cycle models neglect of nutrient limitation on

88 photosynthesis has been questioned from an ecological perspective (Reich et al., 2006a) and it

89 has been argued that without nutrient constraints these models will overestimate future land

90 carbon uptake (Hungate et al., 2003). Since in the real world photosynthesis downregulation does

91 indeed occur due to nutrient constraints, it may be argued that more confidence can be placed

92 in future projections of models that explicitly model the interactions between the terrestrial C

93 and N cycles rather than parameterize it in some other way.

94   Here, we present the implementation of N cycle in the Canadian Land Surface Scheme

95 Including biogeochemical Cycles (CLASSIC) model, which serves as the land component in the

96 family of Canadian Earth System Models (Arora et al., 2009, 2011; Swart et al., 2019). Section 2

97   briefly describes existing physical and carbon cycle components and processes of the CLASSIC

98   model. The conceptual basis of the new N cycle model and its parameterizations are described

99   in Section 3. Section 4 outlines the methodology and data sets that we have used to perform

100   various simulations over the 1850-2017 historical period to assess the realism of the coupled C

101   and N cycles in CLASSIC in response to various forcings. Results from these simulations over the

102   historical period are presented in Section 5 and finally discussion and conclusions are presented

103   in Section 6.

104   **2. The CLASSIC land model**

105   **2.1 The physical and carbon biogeochemical processes**

106   The CLASSIC model is the successor to, and based on, the coupled Canadian Land Surface

107   Scheme (CLASS; Verseghy, 1991; Verseghy et al., 1993) and Canadian Terrestrial Ecosystem

108   Model (CTEM; Arora and Boer, 2005; Melton and Arora, 2016). CLASS and CTEM model physical

109   and biogeochemical processes in CLASSIC, respectively. Both CLASS and CTEM have a long history

110   of development as described in Melton et al. (2019) who also provide an overview of the CLASSIC

111   land model and describe its new technical developments that launched CLASSIC as a community

112   model. CLASSIC simulates land-atmosphere fluxes of water, energy, momentum, CO_2, and CH_4.

113   The CLASSIC model can be run at a point scale, e.g. using meteorological and geophysical data

114   from a FluxNet site, or over a spatial domain, that may be global or regional, using gridded data.

115   We briefly summarize the primary physical and carbon biogeochemical processes of CLASSIC here

116   that are relevant in the context of implementation of the N cycle in the model.

117   **2.1.1 Physical processes**

118   The physical processes of CLASSIC which simulate fluxes of water, energy and momentum,

119   are calculated over vegetated, snow, and bare fractions at a sub-daily time step of 30 minutes.

120   The vegetation is described in terms of four plant functional types (PFTs): needleleaf trees,

121   broadleaf trees, crops, and grasses. The fractional coverage of these four PFTs are specified in

122   the current study over the historical period. The structural attributes of vegetation are described

123   by leaf area index (LAI), vegetation height, canopy mass, and rooting distribution through the soil

124   layers and these are all simulated dynamically by the biogeochemical module of CLASSIC. In the

125   model version used here, 20 ground layers starting with 10 layers of 0.1 m thickness are used.

126   The thickness of layers gradually increases to 30 m for a total ground depth of over 61 m. The

127   depth to bedrock varies geographically and is specified based on a soil depth data set. Liquid and

128   frozen soil moisture contents, and soil temperature, are determined prognostically for

129   permeable soil layers. CLASSIC also prognostically models the temperature, mass, albedo, and

130   density of a single layer snow pack (when the climate permits snow to exist). Interception and

131   throughfall of rain and snow by the canopy, and the subsequent unloading of snow, are also

132   modelled. The energy and water balance over the land surface, and the transfer of heat and

133   moisture through soil, affect the temperature and soil moisture content of soil layers all of which

134   consequently affect the carbon and nitrogen cycle processes.

135

136   **2.1.2 Biogeochemical processes**

137   The biogeochemical processes in CLASSIC are based on CTEM, and described in detail in

138   the appendix of Melton and Arora (2016). The biogeochemical component of CLASSIC simulates

139   the land-atmosphere exchange of CO_2 and while doing so simulates vegetation as a dynamic

140   component. The biogeochemical module of CLASSIC uses information about net radiation, and

141   liquid and frozen soil moisture contents of all the soil layers along with air temperature to

142   simulate photosynthesis and prognostically calculates amount of carbon in the model's three live

143   (leaves, stem, and root) and two dead (litter and soil) carbon pools for each PFT. The litter and

144   soil carbon pools are not tracked for each soil layer. Litter is assumed to be near surface and an

145   exponential distribution for soil carbon is assumed with values decreasing with soil depth.

146   Photosynthesis in CLASSIC is modelled at the same sub-daily time as the physical processes. The

147   remainder of the biogeochemical processes are modelled at a daily time step. These include: 1)

148   autotrophic and heterotrophic respirations from all the live and dead carbon pools, respectively,

149   2) allocation of photosynthate from leaves to stem and roots, 3) leaf phenology, 4) turnover of

150   live vegetation components that generates litter, 5) mortality, 6) land use change (LUC), 7) fire

151   (Arora and Melton, 2018), and 8) competition between PFTs for space (not switched on in this

152   study).

153   Figure A1 in the appendix shows the existing structure of CLASSIC's carbon pools along

154   with the addition of non-structural carbohydrate pools for each of the model's live vegetation

155   components. The non-structural pools are not yet represented in the current operational version

156   of CLASSIC (Melton et al., 2019). The addition of non-structural carbohydrate pools is explained

157   in Asaadi et al. (2018) and helps improve leaf phenology for cold deciduous tree PFTs. The N cycle

158   model presented here is built on the research version of CLASSIC that consists of non-structural

159   and structural carbon pools for the leaves (L), stem (S), and root (R) components and the two

160   dead carbon pools in litter or detritus (D) and soil or humus (H) (Figure A1). We briefly describe

161   these carbon pools and fluxes between them, since N cycle pools and fluxes are closely tied to

162   carbon pools and fluxes. The gross primary productivity (GPP) flux enters the leaves from the

163   atmosphere. This non-structural photosynthate is allocated between leaves, stem, and roots. The

164   non-structural carbon then moves into the structural carbohydrates pool. Once this conversion

165   occurs structural carbon cannot be converted back to non-structural labile carbon. The model

166   attempts to maintain a minimum fraction of non-structural to total carbon in each component of

167   about 0.05 (Asaadi et al., 2018). Non-structural carbon is moved from stem and root components

168   to leaves, at the time of leaf onset for deciduous PFTs, and this is termed reallocation. The

169   movement of non-structural carbon is indicated by red arrows. Maintenance and growth

170   respiration (indicated by subscript m and g in Figure A1), which together constitute autotrophic

171   respiration, occur from the non-structural components of the three live vegetation components.

172   Litterfall from the structural and non-structural components of the vegetation components

173   contributes to the litter pool. Leaf litterfall is generated due to normal turnover of leaves as well

174   as cold and drought stresses, and reduction in day length. Stem and root litter is generated due

175   to their turnover based on their specified life spans. Heterotrophic respiration occurs from the

176   litter and soil carbon pools depending on soil moisture and temperature, and humified litter is

177   moved from litter to the soil carbon pool.

178   All these terrestrial ecosystem processes and the amount of carbon in the live and dead

179   carbon pools are modelled explicitly for nine PFTs that map directly onto the four base PFTs used

180   in the physics module of CLASSIC. Needleleaf trees are divided into their deciduous and

181   evergreen phenotypes, broadleaf trees are divided into cold deciduous, drought deciduous, and

182   evergreen phenotypes, and crops and grasses are divided based on their photosynthetic

183   pathways into C_3 and C_4 versions. The sub-division of PFTs is required for modelling

184   biogeochemical processes. For instance, simulating leaf phenology requires the distinction

185   between evergreen and deciduous phenotypes of needleleaf and broadleaf trees. However, once

186   LAI is known, a physical process (such as the interception of rain and snow by canopy leaves) does

187   not need to know the underlying evergreen or deciduous nature of leaves.

188   The prognostically determined biomasses in leaves, stem, and roots are used to calculate

189   structural vegetation attributes that are required by the physics module. Leaf biomass is used to

190   calculate LAI using PFT-dependent specific leaf area. Stem biomass is used to calculate vegetation

191   height for tree and crop PFTs, and LAI is used to calculate vegetation height for grasses. Finally,

192   root biomass is used to calculate rooting depth and distribution which determines the fraction of

193   roots in each soil layer. Only total root biomass is tracked; fine and coarse root biomasses are not

194   separately tracked. Fraction of fine roots is calculated as a function of total root biomass, as

195   shown later.

196   The approach for calculating photosynthesis in CLASSIC is based on the standard Farquhar

197   et al. (1980) model for C_3 photosynthetic pathway, and Collatz et al. (1992) for the C_4

198   photosynthetic pathway and presented in detail in Arora (2003). The model calculates gross

199   photosynthesis rate that is co-limited by the photosynthetic enzyme Rubisco, by the amount of

200   available light, and by the capacity to transport photosynthetic products for C_3 plants or the CO_2-

201   limited capacity for C_4 plants. In the real world, the maximum Rubsico limited rate (V_{cmax}) depends

202   on the leaf N content since photosynthetic capacity and leaf N are strongly correlated (Evans,

203   1989; Field and Mooney, 1986; Garnier et al., 1999). In the current operational version of

204   CLASSIC, the N cycle is not represented and the PFT-dependent values of V_{cmax} are therefore

205   specified based on Kattge et al. (2009) who compile V_{cmax} values using observation-based data

206   from more than 700 measurements. Along with available light, and the capacity to transport

207   photosynthetic products, the GPP in the model is determined by specified PFT-dependent values

208   of V_{cmax}.

209   In the current CLASSIC version a parameterization of photosynthesis downregulation is included

210   which, in the absence of the N cycle, implicitly attempts to simulate the effects of nutrient

211   constraints. This parameterization, based on approaches which express GPP as a logarithmic

212   function of [CO_2] (Cao et al., 2001; Alexandrov and Oikawa, 2002), is explained in detail in Arora

213   et al. (2009) and briefly summarized here. To parameterize photosynthesis downregulation with

214   increasing [CO_2] the unconstrained or potential GPP (for each time step and each PFT in a grid

215   cell) is multiplied by the global scalar $\xi(c)$

216
$$G = \xi(c)\, G_p \tag{1}$$

217
$$\xi(c) = \frac{1 + \gamma_d \ln(c/c_0)}{1 + \gamma_p \ln(c/c_0)} \tag{2}$$

218   where c is [CO_2] at time t and its initial value is c_0, the parameter γ_p indicates the "potential" rate

219   of increase of GPP with [CO_2] (indicated by the subscript p), the parameter γ_d represents the

220   downregulated rate of increase of GPP with [CO_2] (indicated by the subscript d). When $\gamma_d < \gamma_p$

221   the modelled gross primary productivity (G) increases in response to [CO_2] at a rate determined

222   by the value of γ_d. In the absence of the N cycle, the term $\xi(c)$ thus emulates down-regulation

223   of photosynthesis as CO_2 increases. For example, values of γ_d=0.35 and γ_p=0.90, yield a value of

224    $\xi(c)$ = 0.87 (indicating a 13% downregulation) for c=390 ppm (corresponding to year 2010) and

225   c_0=285 ppm.

226   Note that while the original model version does not include N cycle, it is capable of

227   simulating realistic geographical distribution of GPP that partly comes from the specification of

228   observation-based V_{cmax} values (which implicitly takes into account C and N interactions in a non-

229   dynamic way) but more so the fact that the geographical distribution of GPP (and therefore net

230   primary productivity, NPP), to the first order, depends on climate. The specified V_{cmax} values for

231   the 9 PFTs in CLASSIC vary by about 2 times, from about 35 to 75 μ-mol CO_2 m^{-2} s^{-1}. The simulated

232   GPP in the model, however, varies from zero in the Sahara desert to about 3000 gC m^{-2} $year^{-1}$ in

233   the Amazonian rainforest indicating the overarching control of climate in determining the

234   geographical distribution of GPP. This is further illustrated by the Miami NPP model, for instance,

235   which is able to simulate the geographical distribution of NPP using only mean annual

236   temperature and precipitation (Leith, 1975) since both the C and N cycles are governed primarily

237   by climate. The current version of CLASSIC is also able to reasonably simulate the terrestrial C

238   sink over the second half of the 20th century and early 21st century. CLASSIC (with its former

239   CLASS-CTEM name) has regularly contributed to the annual Trends in Net Land–Atmosphere

240   Carbon Exchange (TRENDY) model intercomparison since 2016 which contributes results to the

241   Global Carbon Project's annual assessments – the most recent one being Friedlingstein et al.

242   (2019). What is then the purpose of coupling C and N cycles?

243

244   **3. Implementation of the N cycle in CLASSIC**

245   The primary objective of implementation of the N cycle is to model V_{cmax} as a function of

246   leaf N content so as to make the use of multiplier $\xi(c)$ obsolete in the model, and allow to project

247 future carbon uptake that is constrained by available N. Modelling of leaf N content as a

248 prognostic variable, however, requires modelling the full N cycle over land. N enters the soil in

249 the inorganic mineral form through biological fixation of N, fertilizer application, and atmospheric

250 N deposition in the form of ammonium and nitrate. N cycling through plants implies uptake of

251 inorganic mineral N by plants, its return to soil through litter generation in the organic form, and

252 its conversion back to mineral form during decomposition of organic matter in litter and soil.

253 Finally, N leaves the coupled soil-vegetation system through leaching in runoff and through

254 various gaseous forms to the atmosphere. This section describes how these processes are

255 implemented and parameterized in the CLASSIC modelling framework. While the first order

256 interactions between C and N cycles are described well by the current climate, their temporal

257 dynamics over time require to explicitly model these processes.

258   Globally, terrestrial N cycle processes are even less constrained than the C cycle

259 processes. As a result, the model structure and parameterizations are based on conceptual

260 understanding and mostly empirical observations of N cycle related biological processes. We

261 attempt to achieve balance between a parsimonious and simple model structure and the ability

262 to represent the primary feedbacks and interactions between different model components.

263 **3.1 Model structure, and N pools and fluxes**

264   N is associated with each of the model's three live vegetation components and the two

265 dead carbon pools (shown in Figure A1). In addition, separate mineral pools of ammonium (NH_4^+)

266 and nitrate (NO_3^-) are considered. Figure 1 shows the C and N pools together in one graphic along

267 with the fluxes of N and C between various pools. The structural and non-structural N pools in

268   root are written as $N_{R,S}$ and $N_{R,NS}$, respectively, and similarly for stem ($N_{S,S}$ and $N_{S,NS}$) and leaves

269   ($N_{L,S}$ and $N_{L,NS}$), and together the structural and non-structural pools make up the total N pools

270   in leaf ($N_L = N_{L,S} + N_{L,NS}$), root ($N_R = N_{R,S} + N_{R,NS}$), and stem ($N_S = N_{S,S} + N_{S,NS}$) components.

271   The fluxes between the pools in Figure 1 characterize the prognostic nature of the pools as

272   defined by the rate change equations summarized in section A1 in the appendix. The model

273   structure allows the C:N ratio of the live leaves ($C : N_L = C_L/N_L$), stem ($C : N_S = C_S/N_S$), and root

274   ($C : N_R = C_R/N_R$) components, and the dead litter (or debris) pool ($C : N_D = C_D/N_D$) to evolve

275   prognostically. The C:N ratio of soil organic matter ($C : N_H = C_H/N_H$), however, is assumed to be

276   constant at 13 following Wania et al. (2012) (see also references therein). The implications of this

277   assumption are discussed later.

278   The individual terms of the rate change equations of the 10 prognostic N pools (equations

279   A1 through A8, and equations A10 and A11 in the appendix), corresponding to Figure 1, are

280   specified or parameterized as explained in the following sections. These parameterizations are

281   divided into three groups and related to 1) N inputs, 2) N cycling in vegetation and soil, and 3) N

282   cycling in mineral pools and N outputs.

283

284   **3.2 N inputs**

285   **3.2.1 Biological N fixation**

286   Biological N fixation (BNF, B_{NH4}) is caused by both free living bacteria in the soil and by

287   bacteria symbiotically living within nodules of host plants' roots. Here, the bacteria convert free

288   nitrogen from the atmosphere to ammonium, which is used by the host plants. Like any other

289   microbial activity, BNF is limited both by drier soil moisture conditions and cold temperatures.

290   Cleveland et al. (1999) attempt to capture this by parameterizing BNF as a function of actual

291   evapotranspiration (AET). AET is a function primarily of soil moisture (through precipitation and

292   soil water balance) and available energy. In places where vegetation exists, AET is also affected

293   by vegetation characteristics including LAI and rooting depth. Here, we parameterize BNF (B_{NH4},

294   gN m^{-2} day^{-1}) as a function of modelled soil moisture and temperature to depth of 0.5 m

295   (following the use of similar depth by Xu-Ri and Prentice (2008)) which yields a very similar

296   geographical distribution of BNF as the Cleveland et al. (1999) approach as seen later in Section

297   4.

$$B_{NH4} = \left(\sum_c \alpha_c f_c + \sum_n \alpha_n f_n + \right) f(T_{0.5}) \, f(\theta_{0.5})$$
$$f(T_{0.5}) = 2^{(T_{0.5}-25)/10}$$
$$f(\theta_{0.5}) = \min\left(0, \max\left(1, \frac{\theta_{0.5}-\theta_w}{\theta_{fc}-\theta_w}\right)\right)$$

298   (3)

299   where α_c and α_n (gN m^{-2} day^{-1}) are BNF coefficients for crop (*c*) and non-crop or natural (*n*) PFTs,

300   which are area weighted using the fractional coverages f_c and f_n of crop and non-crop PFTs that

301   are present in a grid cell, $f(T)$ is the dependence on soil temperature based on a Q$_{10}$ formulation

302   and $f(\theta)$ is the dependence on soil moisture which varies between 0 and 1. θ_{fc} and θ_w are the

303   soil moisture at field capacity and wilting points, respectively. $T_{0.5}$ (°C) and $\theta_{0.5}$ (m^3 m^{-3}) in

304   equation (3) are averaged over the 0.5 m soil depth over which BNF is assumed to occur. We do

305   not make the distinction between symbiotic and non-symbiotic BNF since this requires explicit

306   knowledge of geographical distribution of N fixing PFTs which are not represented separately in

307   our base set of nine PFTs. A higher value of α_c is used compared to α_n to account for the use of

308   N fixing plants over agricultural areas. Biological nitrogen fixation has been an essential

309   component of many farming systems for considerable periods, with evidence for the agricultural

310   use of legumes dating back more than 4,000 years (O'Hara, 1998). A higher α_c than α_n is also

311   consistent with Fowler et al. (2013) who report BNF of 58 and 60 Tg N yr^{-1} for natural and

312   agricultural ecosystems for present day. Since the area of natural ecosystems is about five times

313   the current cropland area, this implies BNF rate per unit land area is higher for crop ecosystems

314   than for natural ecosystems. Values of α_c than α_n and other model parameters are summarized

315   in Table A1.

316   Similar to Cleveland et al. (1999), our approach does not lead to a significant change in

317   BNF with increasing atmospheric CO_2, other than through changes in soil moisture and

318   temperature. At least two meta-analyses, however, suggest that an increase in atmospheric CO_2

319   does lead to an increase in BNF through increased symbiotic activity associated with an increase

320   in both nodule mass and number (McGuire et al., 1995; Liang et al., 2016). Models have

321   attempted to capture this by simulating BNF as a function of NPP (Thornton et al., 2007; Wania

322   et al., 2012). The caveat with this approach and the implications of our BNF approach are

323   discussed in Section 6.

324   **3.2.2 Atmospheric N deposition**

325   Atmospheric N deposition is externally specified. The model reads in spatially- and

326   temporally-varying annual deposition rates from a file. Deposition is assumed to occur at the

327   same rate throughout the year so the same daily rate (gN m^{-2} day^{-1}) is used for all days of a given

328   year. If separate information for ammonium (NH_4^+) and nitrate (NO_3^-) deposition rates is available

329   then it is used otherwise deposition is assumed to be split equally between NH_4^+ and NO_3^-

330   (indicated as P_{NH4} and P_{NO3} in equations A1 and A2).

3.2.3 Fertilizer application

332   Geographically and temporally varying annual fertilizer application rates (F_{NH4}) are also

333   specified externally and read in from a file. Fertilizer application occurs over the C_3 and C_4 crop

334   fractions of grid cells. Agricultural management practices are difficult to model since they vary

335   widely between countries and even from farmer to farmer. For simplicity, we assume fertilizer is

336   applied at the same daily fertilizer application rate (gN m^{-2} day^{-1}) throughout the year in the

337   tropics (between 30°S and 30°N), given the possibility of multiple crop rotations in a given year.

338   Between the 30° and 90° latitudes in both northern and southern hemispheres, we assume that

339   fertilizer application starts on the spring equinox and ends on the fall equinox. The annual

340   fertilizer application rate is thus distributed over around 180 days. This provides somewhat more

341   realism, than using the same treatment as in tropical regions, since extra-tropical agricultural

342   areas typically do not experience multiple crop rotations in a given year. The prior knowledge of

343   start and end days for fertilizer application makes it easier to figure out how much fertilizer is to

344   be applied each day and helps ensure that the annual amount read from the externally specified

345   file is consistently applied.

346

3.3 N cycling in plants and soil

348   Plant roots take up mineral N from soil and then allocate it to leaves and stem to maintain

349   an optimal C:N ratio of each component. Both active and passive plant uptakes of N (from both

350   the NH_4^+ and NO_3^- pools; explained in Sections 3.3.2 and 3.3.3) are explicitly modelled. The active

351   N uptake is modelled as a function of fine root biomass, and passive N uptake depends on the

352   transpiration flux. The modelled plant N uptake also depends on its N demand. Higher N demand

353   leads to higher mineral N uptake from soil as explained below. Litterfall from vegetation

354   contributes to the litter pool and decomposition of litter transfers humified litter to the soil

355   organic matter pool. Decomposition of litter and soil organic matter returns mineralized N back

356   to the NH_4^+ pool, closing the soil-vegetation N cycle loop.

3.3.1 Plant N demand

358   Plant N demand is calculated based on the fraction of NPP allocated to leaves, stem, and

359   root components and their specified minimum PFT-dependent C:N ratios, similar to other models

360   (Xu-Ri and Prentice, 2008; Jiang et al., 2019). The assumption is that plants always want to

361   achieve their desired minimum C:N ratios if enough N is available.

$$\Delta_{WP} = \Delta_L + \Delta_R + \Delta_S$$
$$\Delta_i = \frac{\max\left(0, NPP \cdot a_{i,C}\right)}{C{:}N_{i,\min}}, \quad i = L, S, R \tag{4}$$

363   where the whole plant N demand (Δ_{WP}) is the sum of N demand for the leaves (Δ_L), stem (Δ_S),

364   and root (Δ_R) components, $a_{i,C}, \ i = L, S, R$ is the fraction of NPP (i.e., carbon as indicated by

365   letter C in the subscript, gC m^{-2} day^{-1}) allocated to leaf, stem, and root components, and

366     $C{:}N_{i,\min}, i = L, S, R$ are their specified minimum C:N ratios (see Table A1 for these and all other

367   model parameters). A caveat with this approach when applied at the daily time step, for

368   biogeochemical processes in our model, is that during periods of time when NPP is negative due

369   to adverse climatic conditions (e.g., during winter or drought seasons), the calculated demand is

370 negative. If positive NPP implies there is demand for N, negative NPP cannot be taken to imply

371 that N must be lost from vegetation. As a result, from a plant's perspective, N demand is assumed

372 to be zero during periods of negative NPP. N demand is also set to zero when all leaves have been

373 shed (i.e., when GPP is zero). At the global scale, this leads to about 15% higher annual N demand

374 than would be the case if negative NPP values were taken into consideration.

375

376 **3.3.2 Passive N uptake**

377 N demand is weighed against passive and active N uptake. Passive N uptake depends on

378 the concentration of mineral N in the soil and the water taken up by the plants through their

379 roots as a result of transpiration. We assume that plants have no control over N that comes into

380 the plant through this passive uptake. This is consistent with existing empirical evidence that too

381 much N in soil will cause N toxicity (Goyal and Huffaker, 1984), although we do not model N

382 toxicity in our framework. If the N demand for the current time step cannot be met by passive N

383 uptake then a plant compensates for the deficit (i.e., the remaining demand) through active N

384 uptake.

385 The NH_4^+ concentration in the soil moisture within the rooting zone, referred to as $[NH_4]$

386 (gN gH_2O^{-1}), is calculated as

$$[NH_4] = \frac{N_{\mathrm{NH4}}}{\sum_{i=1}^{i \le r_d} 10^6 \, \theta_i \, z_i} \tag{5}$$

388 where N_{NH4} is ammonium pool size (gN m^{-2}), θ_i is the volumetric soil moisture content for soil

389 layer i (m^3 m^{-3}), z_i is the thickness of soil layer i (m), r_d is the soil layer in which the 99% rooting

390 depth lies as dynamically simulated by the biogeochemical module of CLASSIC following Arora

391 and Boer (2003). The 10^6 term converts units of the denominator term to gH_2O m^{-2}. NO$_3^-$

392 concentration ([NO$_3$], gN gH_2O^{-1}) in the rooting zone is found in a similar fashion. The

393 transpiration flux q_t (Kg H$_2$O m^{-2} s^{-1}) (calculated in the physics module of CLASSIC) is multiplied

394 by [NH$_4$] and [NO$_3$] (gN gH_2O^{-1}) to obtain passive uptake of NH$_4^+$ and NO$_3^-$ (gN m^{-2} day^{-1}) as

395
$$U_{p,NH4} = 86400 \times 10^3 \, \beta \, q_t[NH_4]$$
$$U_{p,NO3} = 86400 \times 10^3 \, \beta \, q_t[NO_3]$$
(6)

396 where the multiplier 86400$\times 10^3$ converts q_t to units of gH$_2$O m^{-2} day^{-1}, and β (see Table A1) is

397 the dimensionless mineral N distribution coefficient with a value less than 1 that accounts for the

398 fact that NH$_4^+$ and NO$_3^-$ available in the soil are not well mixed in the soil moisture solution, and

399 not completely accessible to roots, to be taken up by plants.

400 **3.3.3 Active N uptake**

401   The active plant N uptake is parameterized as a function of fine root biomass and the size

402 of NH$_4^+$ and NO$_3^-$ pools in a manner similar to Gerber et al. (2010) and Wania et al. (2012). The

403 distribution of fine roots across the soil layers is ignored. CLASSIC does not explicitly model fine

404 root biomass. We therefore calculate the fraction of fine root biomass using an empirical

405 relationship that is very similar to the relationship developed by Kurz et al. (1996) (their equation

406 5) but also works below total root biomass of 0.33 Kg C m^{-2} (the Kurz et al. (1996) relationship

407 yields a fraction of fine root more than 1.0 below this threshold). The fraction of fine root biomass

408 (f_r) is given by

409
$$f_r = 1 - \frac{C_R}{C_R + 0.6}$$
(7)

410   where C_R is the root biomass (KgC m^{-2}) simulated by the biogeochemical module of CLASSIC.

411   Equation (7) yields fine root fraction approaching 1.0 as C_R approaches 0, so at very low root

412   biomass values all roots are considered fine roots. For grasses the fraction of fine root biomass is

413   set to 1. The maximum or potential active N uptake for NH$_4^+$ and NO$_3^-$ is given by

$$U_{a,pot,\text{NH4}} = \frac{\varepsilon\, f_r\, C_R\, N_{\text{NH4}}}{k_{p,\frac{1}{2}}\, r_d + N_{\text{NH4}} + N_{\text{NO3}}}$$

414   (8)

$$U_{a,pot,\text{NO3}} = \frac{\varepsilon\, f_r\, C_R\, N_{\text{NO3}}}{k_{p,\frac{1}{2}}\, r_d + N_{\text{NH4}} + N_{\text{NO3}}}$$

415   where ε (see Table A1) is the efficiency of fine roots to take up N per unit fine root mass per day

416   (gN gC^{-1} day^{-1}), $k_{p,\frac{1}{2}}$ (see Table A1) is the half saturation constant (gN m^{-3}), and N_{NH4} and N_{NO3}

417   are the ammonium and nitrate pool sizes (gN m^{-2}) as mentioned earlier. Depending on the

418   geographical location and the time of the year, if passive uptake alone can satisfy plant N demand

419   the actual active N uptake of NH$_4^+$ ($U_{a,actual,\text{NH4}}$) and NO$_3^-$ ($U_{a,actual,\text{NO3}}$) is set to zero.

420   Conversely, during other times both passive and potential active N uptakes may not be able to

421   satisfy the demand and in this case actual active N uptake is equal to its potential rate. At times

422   other than these, the actual active uptake is lower than its potential value. This adjustment of

423   actual active uptake is illustrated in equation (9).

$$\text{if } \left(\Delta_{WP} \leq U_{p,NH4} + U_{p,NO3} \right)$$
$$U_{a,actual,\text{NH4}} = 0$$
$$U_{a,actual,\text{NO3}} = 0$$

$$\text{if } \left(\Delta_{WP} > U_{p,NH4} + U_{p,NO3} \right) \wedge \left(\Delta_{WP} < U_{p,NH4} + U_{p,NO3} + U_{a,pot,\text{NH4}} + U_{a,pot,\text{NH4}} \right)$$

424
$$U_{a,actual,\text{NH4}} = \left(\Delta_{WP} - U_{p,NH4} - U_{p,NO3} \right) \frac{U_{a,pot,\text{NH4}}}{U_{a,pot,\text{NH4}} + U_{a,pot,\text{NH4}}}$$
(9)
$$U_{a,actual,\text{NO3}} = \left(\Delta_{WP} - U_{p,NH4} - U_{p,NO3} \right) \frac{U_{a,pot,\text{NO3}}}{U_{a,pot,\text{NH4}} + U_{a,pot,\text{NH4}}}$$

$$\text{if } \left(\Delta_{WP} \geq U_{p,NH4} + U_{p,NO3} + U_{a,pot,\text{NH4}} + U_{a,pot,\text{NO3}} \right)$$
$$U_{a,actual,\text{NH4}} = U_{a,pot,\text{NH4}}$$
$$U_{a,actual,\text{NO3}} = U_{a,pot,\text{NO3}}$$

425   Finally, the total N uptake (U), uptake of NH_4^+ (U_{NH4}) and NO_3^- (U_{NO3}), are calculated as

426
$$U = U_{p,NH4} + U_{p,NO3} + U_{a,actual,\text{NH4}} + U_{a,actual,\text{NO3}}$$
$$U_{NH4} = U_{p,NH4} + U_{a,actual,\text{NH4}}$$
(10)
$$U_{NO3} = U_{p,NO3} + U_{a,actual,\text{NO3}}$$

427

428   **3.3.4 Litterfall**

429   Nitrogen litterfall from the vegetation components is directly tied to the carbon litterfall

430   calculated by the phenology module of CLASSIC through their current C:N ratios.

431
$$LF_i = \frac{(1-r_L)\, LF_{i,C}}{C:N_i}, i = L, S, R$$
(11)

432   where $LF_{i,C}$ is the carbon litterfall rate (gC day^{-1}) for component i, calculated by the phenology

433   module of CLASSIC, and division by its current C:N ratio yields the nitrogen litterfall rate, r_L (see

434   Table A1) is the leaf resorption coefficient that simulates the resorption of N from leaves of

435   deciduous tree PFTs before they are shed and $r_i = 0, i = R, S$. Litter from each vegetation

436   component is proportioned between structural and non-structural components according to

437   their pool sizes.

438   **3.3.5 Allocation and reallocation**

439   Plant N uptake by roots is allocated to leaves and stem to satisfy their N demand. When

440   plant N demand is greater than zero, total N uptake (U) is divided between leaves, stem, and root

441   components in proportion to their demands such that the allocation fractions for N ($a_i, i =$

442   L, S, R) are calculated as

443
$$a_i = \frac{\Delta_i}{\Delta_{WP}} \ , i = L, S, R$$
$$A_{R2L} = a_L \ (U_{NH4} + U_{NO3})$$
$$A_{R2S} = a_S \ (U_{NH4} + U_{NO3})$$
(12)

444   where A_{R2L} and A_{R2S} are the amounts of N allocated from root to leaves and stem components,

445   respectively, as shown in equations (A5) and (A7). During periods of negative NPP due to adverse

446   climatic conditions (e.g., during winter or drought seasons) the plant N demand is set to zero but

447   passive N uptake, associated with transpiration, may still be occurring if the leaves are still on.

448   Even though there is no N demand, passive N uptake still needs to be partitioned among the

449   vegetation components. During periods of negative NPP allocation fractions for N are, therefore,

450   calculated in proportion to the minimum PFT-dependent C:N ratios of the leaves, stem, and root

451   components as follows.

452
$$a_i = \frac{1/C:N_{i,\min}}{1/C:N_{L,\min} + 1/C:N_{S,\min} + 1/C:N_{R,\min}} \ , i = L, S, R$$
(13)

453   For grasses, which do not have a stem component, equations (12) and (13) are modified

454   accordingly by removing the terms associated with the stem component.

455   Three additional rules override these general allocation rule specifically for deciduous

456   tree PFTs (or deciduous PFTs in general). First, no N allocation is made to leaves once leaf fall is

457   initiated for deciduous tree PFTs and plant N uptake is proportioned between stem and root

458   components based on their demands in a manner similar to equation (12). Second, for deciduous

459   tree PFTs, a fraction of leaf N is resorbed from leaves back into stem and root as follows

460
$$R_{L2R} = r_L \, LF_L \, \frac{N_{R,NS}}{N_{R,NS}+N_{S,NS}}$$
$$R_{L2S} = r_L \, LF_L \, \frac{N_{S,NS}}{N_{R,NS}+N_{S,NS}}$$
(14)

461

462   where r_L is the leaf resorption coefficient, as mentioned earlier, and LF_L is the leaf litter fall rate.

463   Third, and similar to resorption, at the time of leaf onset for deciduous tree PFTs, N is reallocated

464   to leaves (in conjunction with reallocated carbon as explained in Asaadi et al. (2018)) from stem

465   and root components.

466
$$R_{R2L} = \frac{R_{R2L,C}}{C:N_L} \, \frac{N_{R,NS}}{N_{R,NS}+N_{S,NS}}$$
$$R_{S2L} = \frac{R_{S2L,C}}{C:N_L} \, \frac{N_{S,NS}}{N_{R,NS}+N_{S,NS}}$$
(15)

467   where $R_{R2L,C}$ and $R_{S2L,C}$ represent reallocation of carbon from non-structural stem and root

468   components to leaves and division by $C:N_L$ converts the flux into N units. This reallocated N, at

469   the time of leaf onset, is proportioned between non-structural pools of stem and root according

470   to their sizes.

471   **3.3.6 N mineralization, immobilization, and humification**

472   Decomposition of litter ($R_{h,D}$) and soil organic matter ($R_{h,H}$) releases C to the atmosphere

473   and this flux is calculated by the heterotrophic respiration module of CLASSIC. The litter and soil

474   carbon decomposition rates used here are the same as in the standard model version (Melton

475   and Arora, 2016; their Table A3). The amount of N mineralized is calculated straightforwardly by

476   division with the current C:N ratios of the respective pools and contributes to the NH_4^+ pool.

$$M_{D,NH4} = \frac{R_{h,D}}{C:N_D}$$
477   (16)
$$M_{H,NH4} = \frac{R_{h,H}}{C:N_H}$$

478   An implication of mineralization contributing to the NH_4^+ pool, in addition to BNF and fertilizer

479   inputs that also contribute solely to the NH_4^+ pool, is that the simulated NH_4^+ pool is typically

480   larger than the NO_3^- pool. The exception is the dry and arid regions where the lack of

481   denitrification, as discussed below in Section 3.4.2., leads to a build-up of the NO_3^- pool.

482   Immobilization of mineral N from the NH_4^+ and NO_3^- pools into the soil organic matter

483   pool is meant to keep the soil organic matter C:N ratio ($C:N_H$) at its specified value of 13 for all

484   PFTs in a manner similar to Wania et al. (2012) and Zhang et al. (2018). A value of 13 is within the

485   range of observation-based estimates which vary from about 8 to 25 (Zinke et al., 1998; Tipping

486   et al., 2016). Although $C:N_H$ varies geographically, the driving factors behind this variability

487   remain unclear. It is even more difficult to establish if increasing atmospheric CO_2 is changing

488    $C:N_H$ given the large heterogeneity in soil organic C and N densities, and the difficulty in

489   measuring small trends for such large global pools. We therefore make the assumption that the

490    $C:N_H$ does not change with time. An implication of this assumption is that as GPP increases with

491   increasing atmospheric CO_2 rises, and plant litter becomes enriched in C with increasing C:N ratio

492 of litter, more and more N is locked up in the soil organic matter pool because its C:N ratio is

493 fixed. As a result, mineral N pools of NH_4^+ and NO_3^- decrease in size and plant N content

494 subsequently follows. This is consistent with studies of plants grown in elevated CO_2

495 environment. For example, Cotrufo et al. (1998) summarize results from 75 studies and find an

496 average 14% reduction in N concentration for above-ground tissues. Wang et al. (2019) find

497 increased C concentration by 0.8–1.2% and a reduction in N concentration by 7.4–10.7% for rice

498 and winter wheat crop rotation system under elevated CO_2. Another implication of using

499 specified fixed $C:N_H$ is that it does not matter if plant N uptake or immobilization is given

500 preferred access to the mineral N pool since in the long term, by design, N will accumulate in the

501 soil organic matter in response to atmospheric CO_2 increase.

502 Immobilization from both the NH_4^+ and NO_3^- pools (gN m^{-2} day^{-1}) is calculated in

503 proportion to their pool sizes, employing the fixed $C:N_H$ ratio as

$$O_{NH4} = \max\left(0, \left(\frac{C_H}{C:N_H} - N_H\right)\frac{N_{NH4}}{N_{NH4}+N_{NO3}}\right) k_O$$
$$O_{NO3} = \max\left(0, \left(\frac{C_H}{C:N_H} - N_H\right)\frac{N_{NO3}}{N_{NH4}+N_{NO3}}\right) k_O$$

504

(17)

505 where k_O is rate constant with a value of 1.0 day^{-1}. Finally, the carbon flux of humified litter from

506 the litter to the soil organic matter pool ($H_{C,D2H}$) is also associated with a corresponding N flux

507 that depends on the C:N ratio of the litter pool.

$$H_{N,D2H} = \frac{H_{C,D2H}}{C:N_D}$$

508

(18)

509 **3.4 N cycling in mineral pools and N outputs**

510   This section presents the parameterizations of nitrification (which results in transfer of N

511   from the NH_4^+ to the NO_3^- pool) and the associated gaseous fluxes of N_2O and NO (referred to as

512   nitrifier denitrification), gaseous fluxes of N_2O, NO, and N_2 associated with denitrification,

513   volatilization of NH_4^+ into NH_3, and leaching of NO_3^- in runoff.

3.4.1 Nitrification

515   Nitrification, the oxidative process converting ammonium to nitrate, is driven by microbial

516   activity and as such constrained both by high and low soil moisture (Porporato et al., 2003). At

517   high soil moisture content there is little aeration of soil and this constrains aerobic microbial

518   activity, while at low soil moisture content microbial activity is constrained by moisture

519   limitation. In CLASSIC, the heterotrophic respiration from soil carbon is constrained similarly but

520   rather than using soil moisture the parameterization is based on soil matric potential (Arora,

521   2003; Melton et al., 2015). Here, we use the exact same parameterization. In addition to soil

522   moisture, nitrification (gN m^{-2} day^{-1}) is modelled as a function of soil temperature and the size

523   of the NH_4^+ pool as follows

$$I_{NO3} = \eta \, f_I(T_{0.5})f_I(\psi) \, N_{NH4} \qquad (19)$$

525   where η is the nitrification coefficient (day^{-1}, see Table A1), $f_I(\psi)$ is the dimensionless soil

526   moisture scalar that varies between 0 and 1 and depends on soil matric potential (ψ), $f_I(T_{0.5})$ is

527   the dimensionless soil temperature scalar that depends on soil temperature ($T_{0.5}$) averaged over

528   the top 0.5 m soil depth over which nitrification is assumed to occur (following Xu-Ri and Prentice,

529   2008), and N_{NH4} is the ammonium pool size (gN m^{-2}), as mentioned earlier. Both $f_I(T_{0.5})$ and

530    $f_I(\psi)$ are parameterized following Arora (2003) and Melton et al. (2015). $f_I(T_{0.5})$ is a Q_{10} type

531   function with a temperature dependent Q_{10}

$$f_I(T_{0.5}) = Q_{10,I}^{(T_{0.5}-20)/10}, Q_{10,I} = 1.44 + 0.56\left(\tanh\left(0.075(46 - T_{0.5})\right)\right) \tag{20}$$

533   The reference temperature for nitrification is set to 20 °C following Lin et al. (2000). $f_I(\psi)$ is

534   parameterized as a step function of soil matric potential (ψ) as

$$f_I(\psi) = \begin{cases} 0.5 & \text{if } \psi \leq \psi_{sat} \\ 1 - 0.5\frac{\log(0.4)-\log(\psi)}{\log(0.4)-\log(\psi_{sat})} & \text{if } 0.4 > \psi \geq \psi_{sat} \\ 1 & \text{if } 0.6 \geq \psi \geq 0.4 \\ 1 - 0.8\frac{\log(\psi)-\log(0.6)}{\log(100)-\log(0.6)} & \text{if } 100 > \psi > 0.6 \\ 0.2 & \text{if } \psi > 100 \end{cases} \tag{21}$$

536   where the soil matric potential (ψ) is found, following Clapp and Hornberger (1978), as a function

537   of soil moisture (θ)

$$\psi(\theta) = \psi_{sat}\left(\frac{\theta}{\theta_{sat}}\right)^{-B}. \tag{22}$$

539   Saturated matric potential (ψ_{sat}), soil moisture at saturation (i.e., porosity) (θ_{sat}), and the

540   parameter B are calculated as functions of percent sand and clay in soil following Clapp and

541   Hornberger (1978) as shown in Melton et al. (2015). The soil moisture scalar $f_I(\psi)$ is calculated

542   individually for each soil layer and then averaged over the soil depth of 0.5 m over which

543   nitrification is assumed to occur.

544   Gaseous fluxes of NO (I_{NO}) and N_2O (I_{N2O}) associated with nitrification, and generated

545   through nitrifier denitrification, are assumed to be directly proportional to the nitrification flux

546   (I_{NO3}) as

$$547 \qquad \begin{aligned} I_{NO} &= \eta_{NO}\ I_{NO3} \\ I_{N2O} &= \eta_{N2O}\ I_{NO3}. \end{aligned} \qquad (23)$$

548   where η_{NO} and η_{N2O} are dimensionless fractions (see Table A1) which determine what fractions

549   of nitrification flux are emitted as NO and N_2O.

550   **3.4.2 Denitrification**

551   Denitrification is the stepwise microbiological reduction of nitrate to NO, N_2O, and ultimately to

552   N_2 in complete denitrification. Unlike nitrification, however, denitrification is primarily an

553   anaerobic process (Tomasek et al., 2017) and therefore occurs when soil is saturated. As a result,

554   we use a different soil moisture scalar than for nitrification. Similar to nitrification, denitrification

555   is modelled as a function of soil moisture, soil temperature and the size of the NO_3^- pool as follows

556   to calculate the gaseous fluxes of NO, N_2O, and N_2.

$$557 \qquad \begin{aligned} E_{NO} &= \mu_{NO}\ f_E(T_{0.5})\ f_E(\theta)\ N_{NO3} \\ E_{N2O} &= \mu_{N2O}\ f_E(T_{0.5})\ f_E(\theta)\ N_{NO3} \\ E_{N2} &= \mu_{N2}\ f_E(T_{0.5})\ f_E(\theta)\ N_{NO3} \end{aligned} \qquad (24)$$

558   where μ_{NO}, μ_{N2O}, and μ_{N2} are coefficients (day^{-1}, see Table A1) that determine daily rates of

559   emissions of NO, N_2O, and N_2. The temperature scalar $f_E(T_{0.5})$ is exactly the same as the one for

560   nitrification $(f_I(T_{0.5}))$ since denitrification is also assumed to occur over the same 0.5 m soil

561   depth. The soil moisture scalar $f_E(\theta)$ is given by

$$562 \qquad \begin{aligned} f_E(\theta) &= 1 - \tanh\left(2.5\ \left(\tfrac{1-w(\theta)}{1-w_d}\right)^2\right) \\ w(\theta) &= \max\left(0, \min\left(1, \tfrac{\theta-\theta_w}{\theta_f-\theta_w}\right)\right) \end{aligned} \qquad (25)$$

563   where *w* is the soil wetness that varies between 0 and 1 as soil moisture varies between wilting

564   point (θ_w) and field capacity (θ_f), and w_d (see Table A1) is the threshold soil wetness for

565   denitrification below which very little denitrification occurs. Since arid regions are characterized

566   by low soil wetness values, typically below w_d, this leads to build up of the NO_3^- pool in arid

567   regions.

568   **3.4.3 NO_3^- leaching**

569   Leaching is the loss of water-soluble ions through runoff. In contrast to positively charged

570   NH_4^+ ions (i.e. cations), the NO_3^- ions do not bond to soil particles because of the limited exchange

571   capacity of soil for negatively charged ions (i.e., anions). As a result, leaching of N in the form of

572   NO_3^- ions is a common water quality problem, particularly over cropland regions. The leaching

573   flux (L_{NO3}, gN m^{-2} day^{-1}) is parameterized to be directly proportional to baseflow (b_t, Kg m^{-2} s$^-$

574   ^{1}) calculated by the physics module of CLASSIC and the size of the NO_3^- pool (N_{NO3}, gN m^{-2}).

575   Baseflow is the runoff rate from the bottommost soil layer.

$$L_{NO3} = 86400 \, \varphi \, b_t \, N_{NO3} \tag{26}$$

577   where the multiplier 86400 converts units to per day, and φ is the leaching coefficient (m^2 Kg^{-1},

578   see Table A1) that can be thought of as the soil particle surface area (m^2) that 1 Kg of water (or

579   about 0.001 m^3) can effectively wash to leach the nutrients.

580   **3.4.4 NH₃ volatilization**

581   NH_3 volatilization (V_{NH3}, gN m^{-2} day^{-1}) is parametrized as a function of pool size of NH_4^+,

582   soil temperature, soil pH, aerodynamic and boundary layer resistances, and atmospheric NH_3

583   concentration in a manner similar to Riddick et al. (2016) as

584
$$V_{NH4} = \vartheta \; 86400 \; \frac{1}{r_a + r_b} \left(\chi - [NH_{3,a}] \right) \tag{27}$$

585   where ϑ is the dimensionless NH_3 volatilization coefficient (see Table A1) which is set to less than

586   1 to account for the fact that a fraction of ammonia released from the soil is captured by

587   vegetation, r_a (s m^{-1}) is the aerodynamic resistance calculated by the physics module of CLASSIC,

588   χ is the ammonia (NH_3) concentration at the interface of the top soil layer and the atmosphere

589   (g m^{-3}), $[NH_{3,a}]$ is the atmospheric NH_3 concentration specified at 0.3×10^{-6} g m^{-3} following

590   Riddick et al. (2016), 86400 converts flux units from gN m^{-2} s^{-1} to gN m^{-2} day^{-1}, and r_b (s m^{-1}) is

591   the boundary layer resistance calculated following Thom (1975) as

592
$$r_b = 6.2 \, u_*^{-0.67} \tag{28}$$

593   where u_* (m/s) is the friction velocity provided by the physics module of CLASSIC. The ammonia

594   (NH_3) concentration at surface (χ), in a manner similar to Riddick et al. (2016), is calculated as

595
$$\chi = 0.26 \frac{N_{NH4}}{1 + K_H + K_H [H^+]/K_{NH4}} \tag{29}$$

596   where the coefficient 0.26 is the fraction of ammonium in the top 10 cm soil layer assuming

597   exponential distribution of ammonium along the soil depth (given by $3e^{-3z}$, where z is the soil

598   depth), K_H (dimensionless) is the Henry's law constant for NH_3, K_{NH4} (mol L^{-1}) is the dissociation

599   equilibrium constant for aqueous NH_3, and H^+ (mol L^{-1}) is the concentration of hydrogen ion

600   that depends on the soil pH ($H^+ = 10^{-pH}$). K_H and K_{NH4} are modelled as functions of soil

601   temperature of the top 10 cm soil layer ($T_{0.1}$) following Riddick et al. (2016) as

$$K_H = 4.59\, T_{0.1} \exp\left(4092 \left(\frac{1}{T_{0.1}} - \frac{1}{T_{ref,v}}\right)\right)$$

602   (30)

$$K_{NH4} = 5.67 \times 10^{-10} \exp\left(-6286 \left(\frac{1}{T_{0.1}} - \frac{1}{T_{ref,v}}\right)\right)$$

603   where $T_{ref,v}$ is the reference temperature of 298.15 K.

604

3.5 Coupling of C and N cycles

606   As mentioned earlier, the primary objective of coupling of C and N cycles is to be able to

607   simulate V_{cmax} as a function of leaf N content (N_L) for each PFT. This coupling is represented

608   through the following relationship

609                              $V_{cmax} = \Lambda\, (\Gamma_1 N_L + \Gamma_2)$ (31)

610   where Γ_1 (13 µmol CO_2 gN^{-1} s^{-1}) and Γ_2 (8.5 µmol CO_2 m^{-2} s^{-1}) are global constants, except for

611   the broadleaf evergreen tree PFT for which a lower value of Γ_1 (5.1 µmol CO_2 gN^{-1} s^{-1}) is used as

612   discussed below. Λ (≤ 1) is a scalar that reduces calculated V_{cmax} when C:N ratio of any plant

613   component ($C{:}N_i, i = L, S, R$) exceeds its specified maximum value ($C{:}N_{i,\max}, i = L, S, R$) (see

614   Table AA1).

$$\Lambda = \exp\left(-\omega\, k_\Lambda\right)$$
$$\omega = e_L b_L + e_S b_S + e_R b_R$$

615   (32)

$$e_i = \max\left(0, C{:}N_i - C{:}N_{i,\max}\right)$$

$$b_i = \frac{1/C{:}N_{i,\max}}{1/C{:}N_{L,\max}+1/C{:}N_{S,\max}+1/C{:}N_{R,\max}}, i = L, S, R \qquad (33)$$

616

617 where k_Λ is a dimensionless parameter (see Table A1) and ω is dimensionless term that

618 represents excess C:N ratios above specified maximum thresholds ($e_i, i = L, S, R$) weighted by

619 $b_i, i = L, S, R$. When plant components do not exceed their specified maximum C:N ratio

620 thresholds, e_i is zero and Λ is one. When plants components exceed their specified maximum

621 C:N ratio thresholds, Λ starts reducing below one. This decreases V$_{cmax}$ and thus photosynthetic

622 uptake which limits the rate of increase of C:N ratio of plant components, depending on the value

623 of k_Λ.

624   The linear relationship between photosynthetic capacity and N_L (Evans, 1989; Field and

625 Mooney, 1986; Garnier et al., 1999) (used in equation 31) and between photosynthetic capacity

626 and leaf chlorophyll content (Croft et al., 2017) is empirically observed. We have avoided using

627 PFT-dependent values of Γ_1 and Γ_2 for easy optimization of these parameter values but also

628 because such an optimization can potentially hide other model deficiencies. More importantly,

629 using PFT-independent values of Γ_1 and Γ_2 yields a more elegant framework whose successful

630 evaluation will provide confidence in the overall model structure.

631   As shown later in the results section, using Γ_1 and Γ_2 as global constants yields GPP values

632 that are higher in the tropical region than an observation-based estimate. This is not surprising

633 since tropical and mid-latitude regions are known to be limited by P (Vitousek, 1984; Aragão et

634 al., 2009; Vitousek et al., 2010; Du et al., 2020) and our framework currently doesn't model P

635 cycle explicitly. An implication of productivity that is limited by P is that changes in N_L are less

636   important. In the absence of explicit treatment of the P cycle, we therefore simply use a lower

637   value of Γ_1 for the broadleaf evergreen tree PFT which, in our modelling framework, exclusively

638   represents a tropical PFT. Although, a simple way to express P limitation, this approach yields the

639   best comparison with observation-based GPP, as shown later, because the effect of P limitation

640   is most pronounced in the high productivity tropical regions.

641   The second pathway of coupling between the C and N cycles occurs through

642   mineralization of litter and soil organic matter. During periods of higher temperature,

643   heterotrophic C respiration fluxes increase from the litter and soil organic matter pools and this

644   in turn implies an increased mineralization flux (via equation 16) leading to more mineral N

645   available for plants to uptake.

646   **4.0 Methodology**

647   **4.1 Model simulations and input data sets**

648   We perform CLASSIC model simulations with the N cycle for the pre-industrial period

649   followed by several simulations for the historical 1851-2017 period to evaluate the model's

650   response to different forcings, as summarized below. The simulation for the pre-industrial period

651   uses forcings that correspond to year 1850 and the model is run for thousands of years until its

652   C and N pools come into equilibrium. Global thresholds of net atmosphere-land C flux of 0.05

653   Pg/yr and net atmosphere-land N flux of 0.5 Tg N/yr are used to ensure the model pools have

654   reached equilibrium. The pre-industrial simulation, therefore, yields the initial conditions from

655   which the historical simulations for the period 1851-2017 are launched. To spin the mineral N

656   pools to their initial values, the plant N uptake and other organic processes were turned off while

657 the model used specified values of V_{cmax} and only the inorganic part of N cycle was operative.

658 Once the inorganic mineral soil N pools reached near equilibrium, the organic processes were

659 turned on. The model also uses an accelerated spin up procedure for the slow pools of soil organic

660 matter and mineral N. The input and output terms are multiplied by a factor greater than one

661 and this magnifies the change in pool size and therefore accelerates the spin up. Once the model

662 pools reach near equilibrium, the factor is set back to one.

663 To evaluate the model's response to various forcings over the historical period we

664 perform several simulations turning on one forcing at a time as summarized in Table 1. The

665 objective of these simulations is to see if the model response to individual forcings is consistent

666 with expectations. For example, in the CO2-only simulation only atmospheric CO_2 concentration

667 increases over the historical period, while all other forcings stay at their 1850 levels. In the N-

668 DEP-only simulation only N deposition increases over the historical period, and similarly for other

669 runs in Table 1. A "FULL" simulations with all forcings turned on is then also performed which we

670 compare to the original model without a N cycle which uses the photosynthesis downregulation

671 parameterization (termed "ORIGINAL" in Table 1). Finally, a separate pre-industrial simulation is

672 also performed that uses the same Γ_1 and Γ_2 globally (FULL-no-implicit-P-limitation). This

673 simulation is used to illustrate the effect of neglecting P limitation for the broadleaf evergreen

674 tree PFT in the tropics.

675 For the historical period, the model is driven with time-varying forcings that include CO_2

676 concentration, population density (used by the fire module of the model for calculating

677 anthropogenic fire ignition and suppression), land cover, and meteorological data. In addition,

678 for the N cycle module, the model requires time-varying atmospheric N deposition and fertilizer

679   data. The atmospheric CO_2 and meteorological data (CRU-JRA) are same as those used for the

680   TRENDY model intercomparison project for terrestrial ecosystem models for year 2018 (Le Quéré

681   et al., 2018). The CRU-JRA meteorological data is based on 6-hourly Japanese Reanalysis (JRA).

682   However, since reanalysis data typically do match observations they are adjusted for monthly

683   values based on the Climate Research Unit (CRU) data. This yields a blended product with sub-

684   daily temporal resolution that comes from the reanalysis and monthly means/sums that match

685   the CRU data to yield a meteorological product that can be used by models that require sub-daily

686   or daily meteorological forcing. These data are available for the period 1901-2017. Since no

687   meteorological data are available for the 1850-1900 period, we use 1901-1925 meteorological

688   data repeatedly for this duration and also for the pre-industrial spin up. The assumption is that

689   since there is no significant trend in the CRU-JRA data over this period, these data can be reliably

690   used to spin up the model to equilibrium. The land cover data used to force the model are based

691   on a geographical reconstruction of the historical land cover driven by the increase in crop area

692   following Arora and Boer (2010) but using the crop area data prepared for the Global Carbon

693   Project (GCP) 2018 following Hurtt et al. (2006). Since land cover is prescribed, the competition

694   between PFTs for space for the simulations reported here is switched off. The population data

695   for the period 1850-2017 are based on Klein Goldewijk et al. (2017) and obtained from

696   ftp://ftp.pbl.nl/../hyde/hyde3.2/baseline/zip/. The time-independent forcings consist of soil

697   texture and permeable depth data.

698   Time-varying atmospheric N deposition and fertilizer data used over the historical period

699   are also specified as per the TRENDY protocol. The fertilizer data are based on the N_2O model

700   intercomparison project (NMIP) (Tian et al., 2018) and available for the period 1860-2014. For

701   the period before 1860, 1860 fertilizer application rates are used. For the period after 2014,

702   fertilizer application rates for 2014 are used. Atmospheric N deposition data are from input4MIPs

703   (https://esgf-node.llnl.gov/search/input4mips/) and are the same as used by models

704   participating in CMIP6 for the historical period (1850-2014). For years 2015-2017 the N

705   deposition data corresponding to those from representative concentration pathway (RCP) 8.5

706   scenario are used. Figure 2 shows the time series of global annual values of externally specified

707   fertilizer input, and deposition of ammonium and nitrate, based on the TRENDY protocol, for the

708   six primary simulations. Geographical distribution of these inputs are also shown for the last 20

709   years from the FULL simulation corresponding to the 1998-2017 period. In Figure 2 (panels a, c

710   and e) ammonium and nitrate deposition, and fertilizer input stay at their pre-industrial level for

711   simulations in which these forcings do not increase over the historical period. As mentioned

712   earlier, N deposition is split evenly into ammonium and nitrate. The values in parenthesis in

713   Figure 2a legend, and in subsequent time series plots, show average values over the 1850s, the

714   last 20 years (1998-2017) of the simulations, and the change between these two periods. The

715   present day values of fertilizer input and N deposition are consistent with other estimates

716   available in the literature (Table 2). The fertilizer input rate in the simulation with all forcings

717   except land use change (FULL-no-LUC, blue line), that is with no increase in crop area over its

718   1850 value, is 50 Tg N yr^{-1} compared to 91 Tg N yr^{-1} in the FULL simulation, averaged over the

719   1998-2017 period. The additional 41 Tg N yr^{-1} of fertilizer input occurs in the FULL simulation due

720   to the increase in crop area but also due to the increasing fertilizer application rates over the

721   historical period. Geographical distribution of the fertilizer application rates in Figure 2b shows

722   that they are concentrated in regions with crop area and with values as high as 16 gN m^{-2} yr^{-1}

723   especially in eastern China. The N deposition rates (Figure 2d, 2f) are more evenly distributed

724   geographicaly than the fertilizer applications rates, as would be expected, since emissions are

725   transported downstream from their point sources. Areas with high emissions like the eastern

726   United States, India, eastern China, and Europe, however, still stand out as areas that receive

727   higher N deposition.

728   **4.2 Evaluation data sources**

729   We compare globally-summed annual values of N pools and fluxes with observations and

730   other models, and where available their geographical distribution and seasonality. In general,

731   however, much less observation-based data are available to evaluate simulated terrestrial N

732   cycle components than for C cycle components. As a result, N pools and fluxes are primarily

733   compared to results from both observation-based studies and other modelling studies

734   (Bouwman et al., 2013; Fowler et al., 2013; Galloway et al., 2004; Vitousek et al., 2013; Zaehle,

735   2013). Since the primary purpose of the N cycle in our framework is to constrain the C cycle, we

736   also compare globally-summed annual values of GPP and net atmosphere-land CO_2 flux, and their

737   zonal distribution with available observation-based and other estimates. The observation-based

738   estimate of GPP is from Beer et al. (2010), who apply diagnostic models to extrapolate ground-

739   based carbon flux tower observations from about 250 stations to the global scale. Observation-

740   based net atmosphere-land CO_2 flux is from Global Carbon Project's 2019 assessment

741   (Friedlingstein et al., 2019).

742   **5.0 Results**

743   **5.1 N inputs**

744   Figure 3 (panels a, c, e) shows the time series of annual values BNF and its natural and

745   anthropogenic components from the six primary simulations summarized in Table 1. BNF stays

746   at its pre-industrial value of around 80 Tg N yr^{-1} in the CO2-only and N-DEP-only simulations. In

747   the CLIM-only (indicated by magenta coloured line) and the FULL-no-LUC (blue line) simulations

748   the change in climate, associated with increases in temperature and precipitation over the 1901-

749   2017 period (see Figure A2 in the appendix), increases BNF to about 85 Tg N yr^{-1}. In our

750   formulation (equation 3) BNF is positively impacted by increases in temperature and

751   precipitation. In the LUC+FERT-only simulation (dark green line) the increase in crop area

752   contributes to an increase in global BNF with a value around 110 Tg N yr^{-1} for the present day,

753   since a higher BNF per unit crop area is assumed than for natural vegetation. Finally, in the FULL

754   simulation (red line) the 1998-2017 average value is around 117 Tg N yr^{-1} due both to changes in

755   climate over the historical period and the increase in crop area. Our present day value of global

756   BNF is broadly consistent with other modelling and data-based studies as summarized is Table 2.

757   Panels c and e in Figure 3 show the decomposition of the total terrestrial BNF into its natural

758   (over non-crop PFTs) and anthropogenic (over C_3 and C_4 crop PFTs) components. The increase in

759   crop area over the historical period decreases natural BNF from its pre-industrial value of 59 to

760   54 Tg N yr^{-1} for the present day as seen for the LUC+FERT-only simulation (green line) in Figure

761   3c, while anthropogenic BNF over agricultural area increases from 21 to 56 Tg N yr^{-1} (Figure 3e).

762   Figure 3c and 3e show that the increase in BNF (Figure 3a) in the FULL simulation is caused

763   primarily by an increase in crop area. Our present day values of natural and anthropogenic BNF

764   are also broadly consistent with other modelling and data-based studies as summarized in Table

765   2.

766   Figure 3 (panels b, d, and f) shows the geographical distribution of simulated BNF and its

767   natural and anthropogenic components. The geographical distribution of BNF (Figure 3a) looks

768   very similar to the current distribution of vegetation (not shown) with warm and wet regions

769   showing higher values than cold and dry regions since BNF is parameterized as a function of

770   temperature and soil moisture. Anthropogenic BNF only occurs in regions where crop area exists

771   according to the specified land cover and it exhibits higher values than natural BNF in some

772   regions because of its higher value per unit area (see section 3.2.1).

773   At the global scale, and for the present day, natural BNF (59 Tg N yr^{-1}) is overwhelmed by

774   anthropogenic sources: anthropogenic BNF (60 Tg N yr^{-1}), fertilizer input (91.7 Tg N yr^{-1}), and

775   atmospheric N deposition increase since the pre-industrial era (~45 Tg N yr^{-1}). Currently humanity

776   fixes more N than the natural processes (Vitousek, 1994).

777   **5.2 C and N pools, fluxes response to historical changes in forcings**

778   To understand the model response to changes in various forcings over the historical

779   period we first look at the evolution of global values of primary C and N pools, and fluxes, shown

780   in Figures 4 through 8. Figure 4a shows the time evolution of global annual GPP values, the

781   primary flux of C into the land surface, for the six primary simulations, the ORIGINAL simulation

782   performed with the model version with no N cycle, and the ORIG-UNCONST simulation with no

783   photosynthesis downregulation (see Table 1). The unconstrained increase in GPP (35.6 Pg C yr^{-1}

784   over the historical period) in the ORIG-UNCONST simulation (dark cyan line) is governed by the

785   standard photosynthesis model equations following Farquhar et al. (1980) and Collatz et al.

786   (1992) for C$_3$ and C$_4$ plants, respectively. Downregulation of photosynthesis in the ORIGINAL

787   simulation (purple line) is modelled on the basis of equation (1), while in the FULL simulation (red

788   line) photosynthesis downregulation results from a decrease in V_{cmax} values (Figure 5d) due to a

789   decrease in leaf N content (Figure 5b). We will compare the FULL and ORIGINAL simulations in

790   more detail later. The simulations with individual forcings, discussed below, provide insight into

791   the combined response of GPP to all forcings in the FULL simulation.

5.2.1 Response to increasing CO_2

793   The response of C and N cycles to increasing CO_2 in the CO2-only simulation (orange lines

794   in Figure 4) is the most straightforward to interpret. A CO_2 increase causes GPP to increase by 7.5

795   Pg C yr^{-1} above its pre-industrial value (Figure 4a), which in turn causes vegetation (Figure 4b),

796   leaf (Figure 4c), and soil (Figure 4d) carbon mass to increase as well. The vegetation and leaf N

797   amounts (orange line, Figures 5a and 5b), in contrast, decrease in response to increasing CO_2.

798   This is because N gets locked up in the soil organic matter pool (Figure 5c) in response to an

799   increase in the soil C mass (due to the increasing GPP), litter inputs which are now rich in C (due

800   to CO_2 fertilization) but poor in N (since N inputs are still at their pre-industrial level), and the fact

801   that the C:N ratio of the soil organic matter is fixed at 13. This response to elevated CO_2 which

802   leads to increased C and decreased N in vegetation is consistent with meta-analysis of 75 field

803   experiments of elevated CO_2 (Cotrufo et al., 1998). A decrease in N in leaves (orange line, Figure

804   5b) leads to a concomitant decrease in maximum carboxylation capacity (V_{cmax}) (orange line,

805   Figure 5d) and as a result GPP increases at a much slower rate in the CO2-only simulation than in

806   the ORIG-UNCONST simulation (Figure 4a). Due to the N accumulation in the soil organic matter

807   pool, the NH_4^+ and NO_3^- (Figures 5e and 5f) pools also decrease in size in the CO2-only simulation.

808  Figure 6 shows the time series of N demand, plant N uptake and its split between passive

809 and active N uptakes. The plant N demand in the CO2-only simulation (Figure 6a, orange line)

810 increases from its pre-industrial value of 1512 Tg N/yr to 1639 Tg N/yr for the present day since

811 the increasing C input from increasing GPP requires higher N input to maintain preferred

812 minimum C:N ratio of plant tissues. However, since mineral N pools decrease in size over the

813 historical period in this simulation (Figures 5e and 5f), the total plant N uptake (Figure 6b)

814 reduces. Passive plant N uptake is directly proportional to pool sizes of NH_4^+ and NO_3^- and

815 therefore it reduces in response to increasing CO_2. Active plant N uptake, which compensates for

816 insufficient passive N uptake compared to the N demand, also eventually starts to decline as it

817 also depends on mineral N pool sizes. The eventual result of increased C supply and reduced N

818 supply is an increase in the C:N ratio of all plant components and litter (Figure 7). The

819 preindustrial total N uptake of around 960 Tg N/yr (Figure 6b) is lower than the preindustrial N

820 demand (1512 Tg N/yr, Figure 6a) despite the sum of global NH_4 and NO_3 pool sizes being around

821 4000 Tg N (Figures 5e and 5f). This is because of the mismatch between where the pools are high

822 and where the vegetation actually grows and the fact that plant N uptake is limited by its rate.

823 As a result, in our model, even in the preindustrial era vegetation is N limited.

824  Figure 8 shows the net mineralization flux (the net transfer of mineralized N from litter

825 and humus pools to the mineral N pools as a result of the decomposition of organic matter),

826 nitrification (N flux from NH_4^+ to the NO_3^- pool), and the gaseous and leaching losses from the

827 mineral pools. The net mineralization flux reduces in the CO2-only simulation (Figure 8a, orange

828 line) as N gets locked up in the soil organic matter. A reduction in the NH_4^+ pool size in response

829 to increasing CO_2 also yields a reduction in the nitrification flux over the historical period (Figure

830   8b, orange line) since nitrification depends on the NH_4^+ pool size (equation 19). Finally, leaching

831   from the NO_3^- pool (Figure 8c), NH_3 volatilization (Figure 8d), and the gaseous losses associated

832   with nitrification from the NH_4^+ pool (Figure 8e) and denitrification from the NO_3^- pool (Figure 8f)

833   all reduce in response to reduction in pool sizes of NH_4+ and NO_3- in the CO2-only simulation.

834   **5.2.2 Response to changing climate**

835   The perturbation due to climate change alone over the historical period in the CLIM-only

836   simulation (magenta coloured lines in Figures 4 to 8) is smaller than that due to increasing CO_2.

837   In Figure 4a, changes in climate over the historical period increase GPP slightly by 3.60 Pg C yr^{-1}

838   which in turn slightly increases vegetation (including leaf) C mass (Figure 4b,c). The litter and soil

839   carbon mass (Figure 4d), however, decrease slightly due to increased decomposition rates

840   associated with increasing temperature (see Figure A2b). Both the increase in BNF due to

841   increasing temperature (magenta line in Figure 2a), and the reduction in litter and soil N mass

842   (Figure 5c) due to increasing decomposition and higher net N mineralization (Figure 8a, magenta

843   line), make more N available. This results in a slight increase in vegetation and leaf N mass

844   (Figures 5a and 5b) and the NH_4^+ (Figure 5e) pool which is the primary mineral pool in soils under

845   vegetated regions. The global NO_3^- pool, in contrast, decreases in the CLIM-only simulation

846   (Figure 5f) with the reduction primarily occurring in arid regions where the NO_3^- amounts are very

847   large (see Figure 9 that shows the geographical distribution of the primary C and N pools). The

848   geographical distribution of NH_4^+ (Figure 9a) generally follows the geographical distribution of

849   BNF, but with higher values in areas where cropland exists and where N deposition is high. The

850   geographical distribution of NO_3^- (Figure 9b) generally shows lower values than NH_4^+ except in

851   the desert regions where lack of denitrification leads to a large buildup of the NO_3^- pool (as

852   explained earlier in section 3.4.2). Although Figure 9 shows the geographical distribution of

853   mineral N pools from the FULL simulation, the geographical distribution of pools are broadly

854   similar between different simulations with obvious differences such as lack of hot spots of N

855   deposition and fertilizer input in simulations in which these forcings stay at their pre-industrial

856   levels. Figure 9 also shows the simulated geographical distribution of C and N pools in the

857   vegetation and soil organic matter. The increase in GPP due to changing climate increases the N

858   demand (Figure 6a, magenta line) but unlike the CO2-only simulation, the plant N uptake

859   increases since the NH_4^+ and NO_3^- pools increase in size over the vegetated area in response to

860   increased mineralization (Figure 8a, magenta line) and increased BNF (Figure 3a, magenta line).

861   The increase in plant N uptake comes from the increase in passive plant N uptake (Figure 6c)

862   while the active plant N uptake reduces (Figure 6d). Active and passive plant N uptakes are

863   inversely correlated. This is by design since active plant N uptake increases when passive plant N

864   uptake reduces and vice-versa, although eventually both depend on the size of available mineral

865   N pools. Enhancement of plant N uptake due to changes in climate, despite increases in GPP

866   associated with a small increase in V_{cmax} (Figure 5d), leads to a small reduction in the C:N ratio of

867   all plant tissues (Figure 7). The litter C:N, in contrast, shows a small increase since not all N makes

868   its way to the litter as a specified fraction of 0.54 (Table A1) leaf N is resorbed from deciduous

869   trees leaves prior to leaf fall (Figure 7e). Although the leaf C:N ratio decreases in the CLIM only

870   simulation, in response to increased BNF and increased mineralization, this decrease is not large

871   enough to overcome the effect of resorption and as a result the C:N litter increases.

872   Finally, the small increase in pool sizes of NH_4^+ and NO_3^- leads to a small increase in

873   leaching, volatilization, and gaseous losses associated with nitrification and denitrification (Figure

874   8).

875   **5.2.3 Response to N deposition**

876   The simulated response of GPP to changes in N deposition (brown line) over the historical

877   period is smaller than that for CO_2 and climate (Figure 4a). The small increase in GPP of 2.0 Pg C

878   yr^{-1} leads to commensurately small increases in vegetation (Figure 4b) and litter plus soil (Figure

879   4d) C mass. Vegetation and leaf N mass (Figure 5a,b) also increase in response to N deposition

880   and so do mineral pools of NH_4^+ and NO_3^- (Figure 5e,f). The increase in GPP in the simulation with

881   N deposition results from an increase in V_{cmax} rates (Figure 5d) associated with an increase in leaf

882   N content (Figure 5b). N demand increases marginally and so does plant N uptake in response to

883   N deposition (Figure 6). As would be intuitively expected, the C:N ratio of the whole plant, its

884   components of leaves, stem, and root, and litter decreases slightly in response to N deposition

885   (Figure 7). Net N mineralization, nitrification, leaching, volatilization, and gaseous losses

886   associated with nitrification and denitrification all increase in response to N deposition (Figure

887   8).

888   **5.2.4 Response to LUC and fertilizer input**

889   The simulated response to LUC, which reflects an increase in crop area, and increased

890   fertilizer deposition rates over the historical period is shown by dark green lines in Figures 4

891   through 8. The increase in fertilizer input is a much bigger perturbation to the N cycle system

892   than N deposition. Figure 2 shows that at the global scale the fertilizer inputs increase from 0 to

893   ~92 Tg N/yr over the historical period, while the combined NH_4^+ and NO_3^- N deposition rate

894   increases from around 20 to 65 Tg N/yr. In addition, because of higher per unit area BNF rates

895   over crop area than natural vegetation, the increase in crop area in this simulation leads to an

896   increase in anthropogenic BNF from about 20 to 56 Tg N/yr over the historical period. All together

897   increasing crop area and fertilizer inputs imply an additional ~130 Tg N/yr being input into the

898   terrestrial N cycle at the present day since the pre-industrial period, compared to an increase of

899   only 45 Tg N/yr for the N deposition forcing.

900   The global increase in fertilizer input over the historical period leads to higher NH_4^+ and

901   NO_3^- pools (Figures 5e and 5f). Although both fertilizer and BNF contribute to the NH_4^+ pool, the

902   NO_3^- pool also increases through the nitrification flux (Figure 8b). An increase in crop area over

903   the historical period results in deforestation of natural vegetation that reduces vegetation

904   biomass (Figure 4b). However, soil carbon mass also decreases (Figure 4d) despite higher litter

905   inputs. This is because a higher soil decomposition rate is assumed over cropland areas to

906   simulate soil carbon loss as empirical measurements of soil carbon show over deforested areas

907   which are converted to croplands (Wei et al., 2014). Fertilizer application only occurs over crop

908   areas which increases the V_{cmax} rates for crops and, as expected, this yields an increase in globally-

909   averaged V_{cmax} (Figure 5d). A corresponding large increase in leaf N content (Figure 5b) is,

910   however, not seen because vegetation (and therefore leaf) N (Figure 5a,b) is also lost through

911   deforestation. In addition, V_{cmax} is essentially a flux (expressed per unit leaf area) that is averaged

912   over the whole year while leaf and vegetation N pools are sampled at the end of each year and

913   all crops in the northern hemisphere above 30° N are harvested before the year end. Vegetation

914   N mass, in fact, decreases in conjunction with vegetation C mass (Figure 4b). Plant N demand

915   reduces (Figure 6a) and plant N uptake increases (Figure 6b) driven by crop PFTs in response to

916   fertilizer input, as would be intuitively expected. The increase in plant N uptake comes from the

917   increase in passive N uptake, in response to increases in pool sizes of NH_4^+ and NO_3^- over crop

918   areas, while active plant N uptake decreases since passive uptake can more than keep up with

919   the demand over cropland area. While the C:N ratio of vegetation biomass decreases over

920   cropland area in response to fertilizer input (not shown) this is not seen in the globally-averaged

921   C:N ratio of vegetation (Figure 7a) and its components because C and N are also lost through

922   deforestation and the fact that crop biomass is harvested. The C:N of the global litter pool,

923   however, decreases in response to litter from crops which gets rich in N as fertilizer application

924   rates increase. Finally, in Figure 8, global net N mineralization, nitrification, leaching,

925   volatilization, and gaseous losses associated with nitrification and denitrification all increase by

926   a large amount in response to an increase in fertilizer input.

927   **5.2.5 Response to all forcings**

928   We can now evaluate and understand the simulated response of the FULL simulation to

929   all forcings (red line in Figures 4 through 8). The increase in GPP in the FULL simulation (14.5 Pg

930   C/yr) in Figure 4a over the historical period is driven by GPP increase associated with increase in

931   CO_2 (7.5 Pg C/yr), changing climate (3.6 Pg C/yr), and N deposition (2.0 Pg C/yr). The increases

932   associated with these individual forcings add up to 13.1 Pg C/yr indicating that synergistic effects

933   between forcings contribute to the additional 1.4 Pg C/yr increase in GPP. The changes in

934   vegetation and soil plus litter carbon mass (Figures 4b and 4d) in the FULL simulation are similarly

935   driven by these three factors but, in addition, LUC contributes to decreases in vegetation and soil

936   carbon mass as natural vegetation is deforested to accommodate for increases in crop area.

937   Vegetation and leaf N mass (Figures 5a and 5b) decrease in the FULL simulation driven primarily

938   by the response to increasing CO_2 (orange line compared to the red line) while changes in litter

939   and soil N mass are affected variably by all forcings (Figure 5c). Changes in V_{cmax} (Figure 5d) are

940   similarly affected by all forcings: increasing CO_2 leads to a decrease in globally-averaged V_{cmax}

941   values while changes in climate, N deposition, and fertilizer inputs lead to increases in V_{cmax}

942   values with the net result being a small decrease over the historical period. The increase in global

943   NH_4^+ mass in the FULL simulation is driven primarily by the increase in fertilizer input (Figure 5e,

944   red versus green line) while the changes in NO_3^- mass are primarily the result of changes in

945   climate (Figure 5f, magenta line) which causes a decrease in NO_3^- mass from about 1940 to 1970

946   and N deposition and fertilizer input (Figure 5f, green and brown lines) which contribute to the

947   increase in NO_3^- mass later on in the historical period. The increase in N demand (Figure 6a) over

948   the historical period is also driven primarily by the increase in atmospheric CO_2. Plant N uptake

949   (Figure 6b) decreases in response to increasing CO_2 but increases in response to changes in

950   climate, N deposition, and fertilizer inputs such that the net change over the historical is a small

951   decrease. The increase in the C:N ratio of vegetation and its components (leaves, stem, and root)

952   is driven primarily by an increase in atmospheric CO_2 (Figure 7a, red versus orange line). Litter

953   C:N in the FULL simulation, in contrast, does not change substantially over the historical period

954   in a globally-averaged sense as the increase in the C:N ratio of litter associated with an increase

955   in atmospheric CO_2 is mostly compensated by the decrease associated with an increase in N

956   deposition and fertilizer application. The simulated change in global net N mineralization (Figure

957   8a) in the FULL simulation, over the historical period, is small since the decrease in net N

958   mineralization due to increasing CO_2 (orange line) is compensated by the increase caused by

959   changes in climate, N deposition, and fertilizer inputs (magenta, brown, and green lines

960   respectively). The remaining fluxes of nitrification, NO_3^- leaching, NH_3 volatilization, and gaseous

961   losses associated with nitrification and denitrification in the FULL simulation (Figure 8) are all

962   strongly influenced by fertilizer input (green line compared to red line).

963   Table 2 compares simulated values of all primary N pools and fluxes from the FULL

964   simulation with other modelling and quasi observation-based studies. Simulated values are

965   averaged over the 1998-2017 period. Where available, time-periods for other modelling and

966   quasi observation-based studies to which estimates correspond are also noted. For the most part

967   simulated pools and fluxes lie within the range of existing studies with the exception of N_2 and

968   NO emissions that are somewhat higher.

969   **5.2.6 Response to all forcings except LUC**

970   The FULL-no-LUC simulation includes all forcings except LUC (blue line in Figures 4

971   through 8) and corroborates several of the points mentioned above. In this simulation crop area

972   stays at its 1850 value. Figure 2b (blue line) shows increasing global fertilizer input in this

973   simulation despite crop area staying at its 1850 value since fertilizer application rates per unit

974   area increase over the historical period. In the absence of the LUC, vegetation C mass (Figure 4b)

975   and soil plus litter C (Figure 4d) and N (Figure 5c) are higher in the FULL-no-LUC compared to the

976   FULL simulation. N demand (Figure 6a) is slightly higher in FULL-no LUC than in FULL simulation

977   because there is more standing vegetation biomass that is responding to increasing CO_2. The

978   increase in volatilization, leaching, and gaseous losses associated with nitrification and

979   denitrification (Figures 8c-8f) are all primarily caused by increased fertilizer input over the

980   specified 1850 crop area. The increase in N losses associated with these processes, over the

981   historical period, is much lower in the FULL-no-LUC simulation than in the FULL simulation since

982   crop area stays at its 1850 values.

983   **5.3 Comparison of FULL and ORIGINAL simulations**

984   We now compare the results from the FULL simulation that includes the N cycle with that

985   from the ORIGINAL simulation that does not include the N cycle. Both simulations are driven with

986   all forcings over the historical period. Figure 4a shows that the global GPP values in the FULL (red

987   line) and ORIGINAL (purple line) simulations are quite similar although the rate of increase of GPP

988   in the FULL simulation is slightly higher than in the ORIGINAL simulation. As a result, simulated

989   global vegetation biomass is somewhat higher in the FULL simulation (Figure 4b). The simulated

990   global litter and soil carbon mass (Figure 4d) is, however, lower in the FULL simulation (1073 Pg

991   C) compared to the ORIGINAL simulation (1142 Pg C) and this decrease mainly comes from a

992   decrease at higher latitudes (not shown) due to a decrease in GPP (Figure 10a). The lower GPP in

993   the FULL simulation, combined with the slow decomposition at cold high latitudes, results in a

994   lower equilibrium for litter and soil carbon compared with the ORIGINAL simulation. Litter mass

995   contributes about 80 Pg C to the total dead carbon mass. Overall both estimates of 1073 Pg C

996   and 1142 Pg C are somewhat lower than the bulk density corrected estimate of 1230 Pg C based

997   on the Harmonized World Soil Database (HWSD) v.1.2 (Köchy et al., 2015). One reason for this is

998   that CLASSIC does not yet represent permafrost related soil C processes.

999   Figure 10a shows that the zonal distribution of GPP from the FULL and ORIGINAL

1000   simulations, for the 1998-2017 period, compares reasonably well to the observation-based

1001   estimate from Beer et al. (2010). The FULL simulation has slightly lower productivity at high-

1002   latitudes than the ORIGINAL simulation, as mentioned above. Overall, however, the inclusion of

1003   the N cycle does not change the zonal distribution of GPP in the model substantially, which is

1004   determined primarily by the geographical distribution of climate. Figure 10b compares the zonal

1005   distribution of GPP from the pre-industrial simulation (corresponding to 1850s) from the FULL

1006   and FULL-with-no-implicit-P-limitation simulations to illustrate the high GPP in the tropics where

1007   P and not N limitation affects GPP and the reason for choosing a lower value of Γ_1 in equation

1008   (31) for the broadleaf evergreen tree PFT.

1009   The global GPP in the ORIGINAL and FULL simulations averaged over the period 1998-

1010   2017 (120.0 and 120.4 PgC/yr, respectively) are around 15% lower compared to that in the ORIG-

1011   UNCONST simulation (142 PgC/yr), as shown in Figure 4a, yielding a global downregulation factor

1012   of about 0.85. Figure 10c shows how downregulation works in the ORIGINAL and FULL

1013   simulations in a zonally-averaged sense. Ratios of annual GPP averaged over the 1998-2017

1014   period from the ORIGINAL versus ORIG-UNCONST simulations, and FULL versus ORIG-UNCONST

1015   simulations were first calculated for each grid cell and then zonally-averaged over the land grid

1016   cells. Ratios can be misleading especially for grid cells with low values, for example, in the desert

1017   regions. In addition, these ratios also depend on the specified V_{cmax} values in the ORIG-UNCONST

1018   simulation. In Figure 10c, the purple line for the ORIGINAL simulation exhibits values around 0.8

1019   consistent with the global downregulation of around 0.85 and the fact that the same scalar

1020   downregulation multipler is used everywhere on the globe (equation 1). The red line for the FULL

1021   simulation, however, indicates a pattern of higher downregulation at high-latitudes. The peaks

1022   in red line, especially the one around 23°N (Sahara desert), are due to higher values in selected

1023   grid cells in dry and arid regions where the build-up of NO_3^- in the soil (due to reduced

1024   denitrification) increases V_{cmax} and thus GPP in the run with N cycle leading to higher ratios

1025   although the absolute GPP values still remain low.

1026   Figure 11a compares globally-summed net atmosphere-land CO_2 flux from the FULL,

1027   FULL-no-LUC, and ORIGINAL simulations with quasi observation-based estimates from the 2019

1028   Global Carbon Project (Friedlingstein et al., 2019). There are two kinds of estimates in Figure 11a

1029   from Friedlingstein et al. (2019): the first is the net atmosphere-land CO_2 flux for the decades

1030   spanning the 1960s to the 2000s which are shown as rectangular boxes with their corresponding

1031   mean values and ranges, and the second is the terrestrial sink from 1959 to 2018 (dark yellow

1032   line). Positive values indicate a sink of carbon over land and negative values a source. The

1033   difference between the net atmosphere-land CO_2 flux and the terrestrial sink is that the

1034   terrestrial sink minus the LUC emissions yields the net atmosphere-land CO_2 flux. The

1035   atmosphere-land CO_2 flux from the FULL-no-LUC simulation (blue line) is directly comparable to

1036   the terrestrial sink since 1959, since the FULL-no-LUC simulation includes no LUC, and shows that

1037   the simulated terrestrial sink compares fairly well to the estimates from Friedlingstein et al.

1038   (2019). Averaged over the period 1959-2017, the modelled and Global Carbon Project values are

1039   2.0 and 2.1 Pg C/yr, respectively. The net atmosphere-land CO_2 flux from the FULL simulation

1040   mostly lies within the uncertainty range for the five decades considered, although it is on the

1041   higher side compared to estimates from Friedlingstein et al. (2019). The reason for this is that

1042   LUC emissions in CLASSIC are much lower than observation-based estimates, as discussed below

1043   in context of Figure 11c. CLASSIC simulates LUC emissions only in response to changes in crop

1044   area whereas changes in pasture area and wood harvesting also contribute to LUC emissions. The

1045 net-atmosphere land CO_2 flux from the ORIGINAL simulation compares better with the estimates

1046 from Friedlingstein et al. (2019), than the FULL simulation, because the photosynthesis down-

1047 regulation parameter in the ORIGINAL simulation has been adjusted despite discrepancies in

1048 simulated LUC processes.

1049   Figure 11b compares the zonal distribution of simulated net atmosphere-land CO_2 flux

1050 from the FULL and ORIGINAL simulations with the model-mean and range from the terrestrial

1051 ecosystem models that participated in the 2019 TRENDY model intercomparison and contributed

1052 results to 2019 Global Carbon Project (Friedlingstein et al., 2019). The carbon sink simulated by

1053 CLASSIC in the northern hemisphere is broadly comparable to the model-mean estimate from

1054 the TRENDY models. However, in the tropics CLASSIC simulates a much stronger sink than the

1055 model-mean, likely because of its lower LUC emissions.

1056 **5.4 Contribution of forcings to land C sink and sources**

1057   Figure 11c shows cumulative net atmosphere-land CO_2 flux for the 1850-2017 period from

1058 the six primary simulations with N cycle. These simulations facilitate the attribution of carbon

1059 uptake and release over the historical period to various forcings. The cumulative terrestrial sink

1060 in the FULL-no-LUC simulation for the period 1850-2017 is simulated to be ~153 Pg C and this

1061 compares reasonably well with the estimate of 185 ± 50 Pg C for the period 1850-2014 from Le

1062 Quéré et al. (2018). Increase in CO_2 (~115 Pg C), change in climate (~3 Pg C), and N deposition

1063 (~19 Pg C) all contribute to this terrestrial sink. These three contributions add up to 137 Pg C so

1064 the additional 16 Pg C is contributed by the synergistic effects between the three forcings.

1065 Quantified in this way, the contribution of increasing CO_2 (115 out of 137 Pg C), climate change

1066   (3 out of 137 Pg C), and N deposition (19 out of 137 Pg C) to carbon uptake by land over the

1067   historical period (1850-2017) is calculated to be 84%, 2%, and 14%, respectively. Cumulative LUC

1068   emissions simulated for the period 1850-2017 by CLASSIC can be estimated using a negative

1069   cumulative net-atmosphere-land CO_2 flux of ~66 Pg C from the LUC+FERT-only simulation or by

1070   the differencing the FULL and FULL-no-LUC simulations (~71 Pg C). While LUC emissions are highly

1071   uncertain, both of these estimates are much lower than the 195 ± 75 Pg C estimate from Le Quéré

1072   et al. (2018).

1073   **6.0 Discussion and conclusions**

1074   The interactions between terrestrial C and N cycles are complex and our understanding

1075   of these interactions, and their representation in models, is based on empirical observations of

1076   various terrestrial ecosystem processes. In this paper, we have evaluated the response of these

1077   interactions by perturbing the coupled C and N cycle processes in the CLASSIC model with one

1078   forcing at a time over the historical period: 1) increase in CO_2, 2) change in climate, 3) increase in

1079   N deposition, and 4) LUC with increasing fertilizer input. These simulations are easier to interpret

1080   and the model response can be evaluated against both our conceptual knowledge as well as

1081   empirical observation-based data. Our assumption is that, if the model response to individual

1082   forcings is realistic and consistent with expectations based on empirical observations then the

1083   response of the model to all forcings combined will also be realistic and easier to interpret,

1084   although we do expect and see synergistic effects between forcings.

1085   The simulated response of coupled C and N cycles in CLASSIC to increasing atmospheric

1086 CO_2 is an increase in the C:N ratio of vegetation components due to an increase in their C content

1087   but also a decrease in their N content. This model response is conceptually consistent with a

1088   meta-analysis of 75 field experiments of elevated CO_2 as reported in Cotrufo et al. (1998) who

1089   find an average reduction in tissue N concentration of 14%. Most studies analyzed in the Cotrufo

1090   et al. (1998) meta-analysis used ambient CO_2 of around 350 ppm and elevated CO_2 of around

1091   650-700 ppm. In comparison, the plant N concentration in CLASSIC reduces by ~26% in response

1092   to a gradual increase in atmospheric CO_2 from 285 ppm to 407 ppm (an increase of 122 ppm)

1093   over the 1850-2017 period (whole plant C:N ratio increases from 142.6 to 194.1 in the CO2-only

1094   simulation, Figure 7a). These two estimates cannot be compared directly - the majority (59%) of

1095   Free-Air Carbon dioxide Enrichment (FACE) experiments last less than 3 years (Jones et al., 2014)

1096   and the vegetation experiences a large CO_2 change of around 300-350 ppm while the duration of

1097   our historical simulation is 167 years and the gradual increase in CO_2 of 122 ppm over the

1098   historical period is much smaller.

1099   The response of our model to CO_2 increase over the historical period is also consistent

1100   with the meta-analysis of McGuire et al. (1995) who report an average decrease in leaf N

1101   concentration of 21% in response to elevated CO_2 based on 77 studies, which is the primary

1102   reason for downregulation of photosynthetic capacity. The simulated decrease in leaf N

1103   concentration in our study for the CO2-only experiment is around 27% (leaf C:N ratio increases

1104   from 42.8 to 58.6 in the CO2-only simulation, Figure 7b). Although, the same caveats that apply

1105   to the comparison with the Cotrufo et al. (1998) study also apply to this comparison. The

1106   decrease in whole plant and leaf N concentrations in our results is conceptually consistent with

1107   the meta-analyses of McGuire et al. (1995) and Cotrufo et al. (1998). The decrease in whole plant

1108   N concentration in our CO2-only and FULL simulations is the result of an increase in both tissue

1109 C amount and a decrease in N amount. The decrease in tissue N amount is, in fact, necessary in

1110 our modelling framework to induce the required downregulation of photosynthesis to simulate

1111 the land carbon sink realistically over the historical period.

1112 The meta-analysis of Liang et al. (2016) reports an increase in above and belowground

1113 plant N pools in response to elevated CO_2 associated with increase in BNF but since their results

1114 are based on pool sizes they cannot be compared directly to the N concentration based results

1115 from McGuire et al. (1995) and Cotrufo et al. (1998). Liang et al. (2016) also report results from

1116 short-term ($\leq$ 3 years) and long-term (between 3 to 15 years) studies separately (their Figure 3).

1117 They show that the increase in total plant and litter N pools become smaller for long-term studies.

1118 Regardless, the difference in time scales of empirical studies and the real world is a caveat that

1119 will always make it difficult to evaluate model results over long time scales.

1120 The response of C and N cycles to changes in climate in our model (in the CLIM-only

1121 simulation) is also conceptually realistic. Globally, GPP increases in response to climate that

1122 gradually gets warmer and wetter (see Figure A2) and as a result vegetation biomass increases.

1123 Soil carbon mass, however, decreases (despite increase in NPP inputs) since warmer

1124 temperatures also increase heterotrophic respiration (not shown). As a result of increased

1125 decomposition of soil organic matter, net N mineralization increases and together with increased

1126 BNF the overall C:N ratio of vegetation and leaves decreases, which leads to a V_{cmax} increase. The

1127 small increase in V_{cmax}, due to increased mineralization, thus also contributes to an increase in

1128 GPP over and above that due to a change in climate alone, and therefore compensates for the

1129 amount of carbon lost due to increased soil organic matter decomposition associated with

1130 warmer temperatures. This behaviour is consistent with land C cycle models showing a reduction

1131 in the absolute value of the strength of the carbon-climate feedback when they include coupling

1132 of C and N cycles (Arora et al., 2020).

1133 The modelled differences in PFT specific values of V_{cmax}, in our framework, come through

1134 differences in simulated values of leaf N content (N_L) that depend on BNF (given that BNF is the

1135 primary natural source of N input into the coupled soil-vegetation system) but also differences

1136 in mineralization that are governed by climate. N_L values, however, also depend on leaf

1137 phenology, allocation of carbon and nitrogen, turnover rates, transpiration (which brings in N

1138 through passive uptake), and almost every aspect of plant biogeochemistry which affects a PFT's

1139 net primary productivity and therefore N demand. Modelled increases in GPP in response to N

1140 deposition come through an increase in leaf N content and therefore V_{cmax} values.

1141 Finally, changes in land use associated with an increase in crop area, and the associated

1142 increase in fertilizer application rates lead to the largest increase in NO_3^- leaching, NH_3

1143 volatilization, and gaseous losses associated with nitrification and denitrification among all

1144 forcings. Overall, the model response to perturbation by all individual forcings is realistic,

1145 conceptually expected, and of the right sign (positive or negative) although it is difficult to

1146 evaluate the magnitude of these responses in the absence of directly comparable observation-

1147 based estimates.

1148 Despite the model responses to individual forcings that appears consistent with our

1149 conceptual understanding of coupled C and N cycles, our modelling framework misses an

1150 important feedback process that has been observed in the FACE and other experiments related

1151 to changes in natural BNF. FACE sites and other empirical studies report an increase in natural

1152 BNF rates at elevated CO_2 (McGuire et al., 1995; Liang et al., 2016) and a decrease in natural BNF

1153 rates when additional N is applied to soils (Salvagiotti et al., 2008; Ochoa-Hueso et al., 2013). On

1154 a broad scale this is intuitively expected but the biological processes behind changes in BNF rates

1155 remain largely unclear. A response can still be parameterized even if the underlying physical and

1156 biological processes are not well understood. For instance, Goll et al. (2012) parameterize BNF as

1157 an increasing and saturating function of NPP, $BNF = 1.8\left(1.0 - exp(-0.003\ NPP)\right)$. This

1158 approach, however, does not account for the driver behind the increase in NPP - increasing

1159 atmospheric CO_2, change in environmental conditions (e.g., wetter and warmer conditions), or

1160 increased N deposition. Clearly, increasing BNF if the NPP increase is due to N deposition is

1161 inconsistent with empirical observations. Over the historical period an increase in atmospheric

1162 CO_2 has been associated with an increase in N deposition so to some extent changes in BNF due

1163 to both forcings will cancel each other. We realize the importance of changes in BNF, given it is

1164 the single largest natural flux of N into the coupled soil-vegetation system yet highly uncertain,

1165 and aim to address these issues in a future version of the model by exploring existing BNF

1166 formulations. Meyerholt et al. (2016), for example, demonstrate the uncertainty arising from the

1167 use of five different BNF parameterizations in the context of the O-CN model. They use

1168 formulations that parameterize BNF as a function of 1) evapotranspiration, 2) NPP, 3) leaf C:N

1169 ratio, that takes into account energy cost for N fixation (Fisher et al., 2010), 4) plant N demand,

1170 and 5) an optimality-based approach that follows Rastetter et al. (2001) in which BNF only occurs

1171 when the carbon cost of N fixation is lower than the carbon cost of root N uptake. The approach

1172 used in our study is closest to the one that is based on evapotranspiration but makes the

1173 distinction in BNF rates over natural and agricultural areas.

1174   The reduction of photosynthesis rates in response to N limitation is the most important

1175   linkage between C and N cycles and yet it too is parameterized differently across models. Given

1176   that leaf N content and photosynthetic capacity are strongly correlated (Evans, 1989; Field and

1177   Mooney, 1986; Garnier et al., 1999), photosynthesis downregulation due to N limitation reduces

1178   photosynthetic capacity, and thus the GPP flux. Yet models reduce both NPP (Wiltshire et al.,

1179   2020) and V_{cmax} rates, and thus GPP, (Zaehle and Friend, 2010; Wania et al., 2012; von Bloh et al.,

1180   2018) in reponse to N limitation. V_{cmax} rates may themselves be parameterized as a function leaf

1181   N content directly (von Bloh et al., 2018; Zaehle and Friend, 2010) or leaf C:N ratio (Wania et al.,

1182   2012). In this study, we have parameterized V_{cmax} rates as a function of leaf N content (equation

1183   31) since the use of leaf C:N ratio leads to an incorrect seasonal variation of V_{cmax}. If an increase

1184   in leaf C:N ratio, as a result of increase in atmospheric CO_2, leads to a decrease in V_{cmax} rates over

1185   the historical period then it implies that V_{cmax} is inversely related to leaf C:N ratios. Since leaf C:N

1186   ratio peak during the growing season (Li et al., 2017) this also implies V_{cmax} rates are lower during

1187   the growing season than at its start and this is in contrast to observations that show an increase

1188   in V_{cmax} during the growing season (e.g., see Fig. 1a of Bauerle et al. (2012)).

1189   Our framework assumes a constant C:N ratio of 13 for soil organic matter ($C:N_H$), an

1190   assumption also made in other models (e.g., Wania et al., 2012; Zhang et al., 2018). This

1191   assumption is also broadly consistent with Zhao et al. (2019) who attempt to model C:N of soil

1192   organic matter, among other soil properties, as a function of mean annual temperature and

1193   precipitation using machine learning algorithms (their Figure 2h). It is difficult to currently

1194   establish if increasing atmospheric CO_2 is changing $C:N_H$ given the large heterogeneity in soil

1195   organic C and N densities, and the difficulty in measuring small trends for such large global pools.

1196 A choice of a somewhat different value for all PFTs or had we chosen specified constant PFT-

1197 dependent values of $C{:}N_H$ is of relatively less importance in this context since the model is spun

1198 to equilibrium for 1850 conditions anyway. It is the change in $C{:}N_H$ over time that is of

1199 importance. The assumption of constant $C{:}N_H$ is the key to yielding a decrease in vegetation N

1200 mass, and therefore leaf N mass and V_{cmax}, as CO_2 increases, in our framework. Without a

1201 decrease in V_{cmax} in our modelling framework, in response to elevated CO_2, we cannot achieve

1202 the downregulation noted by McGuire et al. (1995) in their meta-analysis, and the simulated

1203 carbon sink over the historical period would be greater than observed as noted above. It is

1204 possible that we are simulating the reduction in leaf N mass, in response to elevated CO_2, for a

1205 wrong reason in which case our model processes need to be revisited based on additional

1206 empirical data. If our assumption of constant or extremely slowly changing $C{:}N_H$ is indeed

1207 severely unrealistic, this necessitates a point of caution that a realistic land carbon sink can be

1208 simulated over the historical period with such an assumption.

1209 Related to this assumption is also the fact that we cannot make decomposition rates of

1210 soil organic matter a function of its C:N ratio since it is assumed to be a constant. It is well known

1211 that after climate, litter and soil organic matter decomposition rates are controlled by their C:N

1212 ratio (Manzoni et al., 2008). Litter decomposition rates can still be made a function of its C:N ratio

1213 and we aim to do this for a future model version.

1214 The work presented in this study of coupling C and N cycles in CLASSIC yields a framework

1215 that we can build upon to make model processes more realistic, test the effect of various model

1216 assumptions, parameterize existing processes in other ways, include additional processes, and

1217 evaluate model response at FluxNet sites to constrain model parameters.

Appendix

A1. Budget equations for N pools

The rates of change of N in the NH_4^+ and NO_3^- pools (in gN m^{-2}), N_{NH4} and N_{NO3}, respectively, are given by

$$\frac{d\,N_{NH4}}{dt} = B_{NH4} + F_{NH4} + P_{NH4} + M_{D,NH4} + M_{H,NH4}$$

$$-U_{NH4} - (I_{NO3} + I_{N2O} + I_{NO}) - V_{NH3} - O_{NH4} \tag{A1}$$

$$\frac{d\,N_{NO3}}{dt} = P_{NO3} + I_{NO3} - L_{NO3} - U_{NO3} - (E_{N2} + E_{N2O} + E_{NO}) - O_{NO3} \tag{A2}$$

and all fluxes are represented in units of gN m^{-2} day^{-1}. B_{NH4} is the rate of biological N fixation which solely contributes to the NH_4^+ pool, F_{NH4} is the fertilizer input which is assumed to contribute only to the NH_4^+ pool, and P_{NH4} and P_{NO3} are atmospheric deposition rates that contribute to the NH_4^+ and NO_3^- pools, respectively. Biological N fixation, fertilizer input, and atmospheric deposition are the three routes through which N enters the coupled soil-vegetation system. $M_{D,NH4}$ and $M_{H,NH4}$ are the mineralization flux from the litter and soil organic matter pools, respectively, associated with their decomposition. We assume mineralization of humus and litter pools only contributes to the NH_4^+ pool. O_{NH4} and O_{NO3} indicate immobilization of N from the NH_4^+ and NO_3^- pools, respectively, to the humus N pool which implies microbes (that are not represented explicitly) are part of the humus pool. Combined together the terms $(M_{D,NH4} + M_{H,NH4} - O_{NH4} - O_{NO3})$ yield the net mineralization rate. V_{NH3} is the rate of ammonia (NH_3) volatilization and L_{NO3} is the leaching of N that occurs only from the NO_3^- pool.

1238   The positively charged ammonium ions are attracted to the negatively charged soil particles and

1239   as a result it is primarily the negatively charged nitrate ions that leach through the soil (Porporato

1240   et al., 2003; Xu-Ri and Prentice, 2008). U_{NH4} and U_{NO3} are uptakes of NH_4^+ and NO_3^- by plants,

1241   respectively. The nitrification flux from NH_4^+ to NO_3^- pool is represented by I_{NO3} which also results

1242   in the release of the nitrous oxide (N_2O), a greenhouse gas, and nitric oxide (NO) through nitrifier

1243   denitrification represented by the terms I_{N2O} and I_{NO}, respectively. Finally, E_{N2}, E_{N2O}, and E_{NO}

1244   are the gaseous losses of N_2 (nitrogen gas), N_2O, and NO from the NO_3^- pool associated with

1245   denitrification. N is thus lost through the soil-vegetation system via leaching in runoff and

1246   through gaseous losses of I_{N2O}, I_{NO}, E_{N2}, E_{N2O}, E_{NO}, and V_{NH3}.

1247   The structural and non-structural N pools in root are written as $N_{R,S}$ and $N_{R,NS}$,

1248   respectively, and similarly for stem ($N_{S,S}$ and $N_{S,NS}$) and leaves ($N_{L,S}$ and $N_{L,NS}$), and together the

1249   structural and non-structural pools make the total N pool in leaf ($N_L = N_{L,S} + N_{L,NS}$), root ($N_R =$

1250 $N_{R,S} + N_{R,NS}$), and stem ($N_S = N_{S,S} + N_{S,NS}$) components. The rate change equation for

1251   structural and non-structural N pools in root are given by

1252
$$\frac{d\,N_{R,NS}}{dt} = U_{NH4} + U_{NO3} + R_{L2R} - R_{R2L} - A_{R2L} - A_{R2S} - LF_{R,NS} - T_{R,NS2S} \tag{A3}$$

1253
$$\frac{d\,N_{R,S}}{dt} = T_{R,NS2S} - LF_{R,S} \tag{A4}$$

1254   Similar to the uptake of carbon by leaves and its subsequent allocation to root and stem

1255   components, N is taken up by roots and then allocated to leaves and stem. A_{R2L} and A_{R2S}

1256   represent the allocation of N from roots to leaves and stem, respectively. The terms R_{L2R} and

1257 R_{R2L} represent the reallocation of N between the non-structural components of root and leaves.

1258 R_{L2R} is the N reallocated from leaves to root representing resorption of a fraction of leaf N during

1259   leaf fall for deciduous tree PFTs. R_{R2L} indicates reallocation of N from roots to leaves (termed

1260   reallocation in Figure 2) at the time of leaf-out for deciduous tree PFTs. At times other than leaf-

1261   out and leaf-fall and for other PFTs these two terms are zero. $T_{R,NS2S}$ is the one way transfer of

1262   N from the non-structural to the structural root pool, and similar to the carbon pools, once N is

1263   converted to its structural form it cannot be converted back to its non-structural form. Finally,

1264   the litterfall due to turnover of roots occurs from both the structural ($LF_{R,S}$) and non-structural

1265   ($LF_{R,NS}$) N pools.

1266   The rate change equations for non-structural and structural components of leaves are

1267   written as

1268

$$\frac{d\,N_{L,NS}}{dt} = A_{R2L} - R_{L2R} - R_{L2S} + R_{R2L} + R_{S2L} - LF_{L,NS} - T_{L,NS2S} \qquad (A5)$$

1269

$$\frac{d\,N_{L,S}}{dt} = T_{L,NS2S} - LF_{L,S} \qquad (A6)$$

1270   where $T_{L,NS2S}$ is the one way transfer of N from the non-structural leaf component to its

1271   structural N pool and R_{S2L} indicates reallocation of N from stem to leaves (similar to R_{R2L}) at the

1272   time of leaf out for deciduous tree PFTs. Litterfall occurs from both the structural ($LF_{L,S}$) and non-

1273   structural ($LF_{L,NS}$) N pools of leaves, and all other terms have been previously defined.

1274   Finally, the rate change equations for non-structural and structural components of stem

1275   are written as

1276

$$\frac{d\,N_{S,NS}}{dt} = A_{R2S} + R_{L2S} - R_{S2L} - LF_{S,NS} - T_{S,NS2S} \qquad (A7)$$

1277

$$\frac{d\,N_{S,S}}{dt} = T_{S,NS2S} - LF_{S,S} \qquad (A8)$$

1278 where $LF_{S,NS}$ and $LF_{S,S}$ represent stem litter from the non-structural and structural components,

1279 $T_{S,NS2S}$ is the one way transfer of N from the non-structural stem component to its structural N

1280 pool. All other terms have been previously defined.

1281   Adding equations (6) through (11) yields rate of change of N in the entire vegetation pool

1282 (N_V) as

$$\frac{d\,N_V}{dt} = \frac{d\,N_{R,NS}}{dt} + \frac{d\,N_{R,S}}{dt} + \frac{d\,N_{L,NS}}{dt} + \frac{d\,N_{L,S}}{dt} + \frac{d\,N_{S,NS}}{dt} + \frac{d\,N_{S,S}}{dt} = \frac{d\,N_R}{dt} + \frac{d\,N_L}{dt} + \frac{d\,N_S}{dt}$$

1283 $$\begin{aligned}\frac{d\,N_V}{dt} &= U_{NH4} + U_{NO3} - LF_{R,NS} - LF_{R,S} - LF_{L,NS} - LF_{L,S} - LF_{S,NS} - LF_{S,S}\\ &= U_{NH4} + U_{NO3} - LF_R \qquad\qquad - LF_L \qquad\qquad - LF_S\end{aligned}$$

                  (A9)

1284 which indicates how the dynamically varying vegetation N pool is governed by mineral N uptake

1285 from the NH_4^+ and NO_3^- pools and litterfall from the structural and non-structural components of

1286 the leaves, stem, and root pools. LF_R is the total N litter generation from the root pool and sum

1287 of litter generation from its structural and non-structural components ($LF_R = LF_{R,S} + LF_{R,NS}$),

1288 and similarly for the leaves (LF_L) and the stem (LF_S) pools.

1289   The rate change equations for the organic N pools in the litter (N_D) and soil (N_H) pools

1290 are written as follows.

1291 $$\frac{d\,N_D}{dt} = LF_R + LF_L + LF_S - H_{N,D2H} - M_{D,NH4} \qquad\qquad (A10)$$

1292 $$\frac{d\,N_H}{dt} = H_{N,D2H} + O_{NH4} + O_{NO3} - M_{H,NH4} \qquad\qquad (A11)$$

1293 where $H_{N,D2H}$ is the transfer of humidified organic matter from litter to the soil organic matter

1294 pool, and all other terms have been previously defined.

1295

1296

Acknowledgments

We are grateful and thank Joe Melton and Paul Bartlett for their comments on an earlier version
of this manuscript.

1300

Code/Data availability

Model code for the operational CLASSIC model can be obtained from
https://gitlab.com/cccma/classic. Changes made to the operational version to include N cycle
and the results shown here can be obtained from the second author.

1305

Author contributions

A.A. implemented the N cycle in the CLASSIC code, put together all the N cycle related input
data, and performed all the simulations. V.A. and A.A. wrote the manuscript.

1309

Competing interests

There are no competing interests.

1312

1313

1314
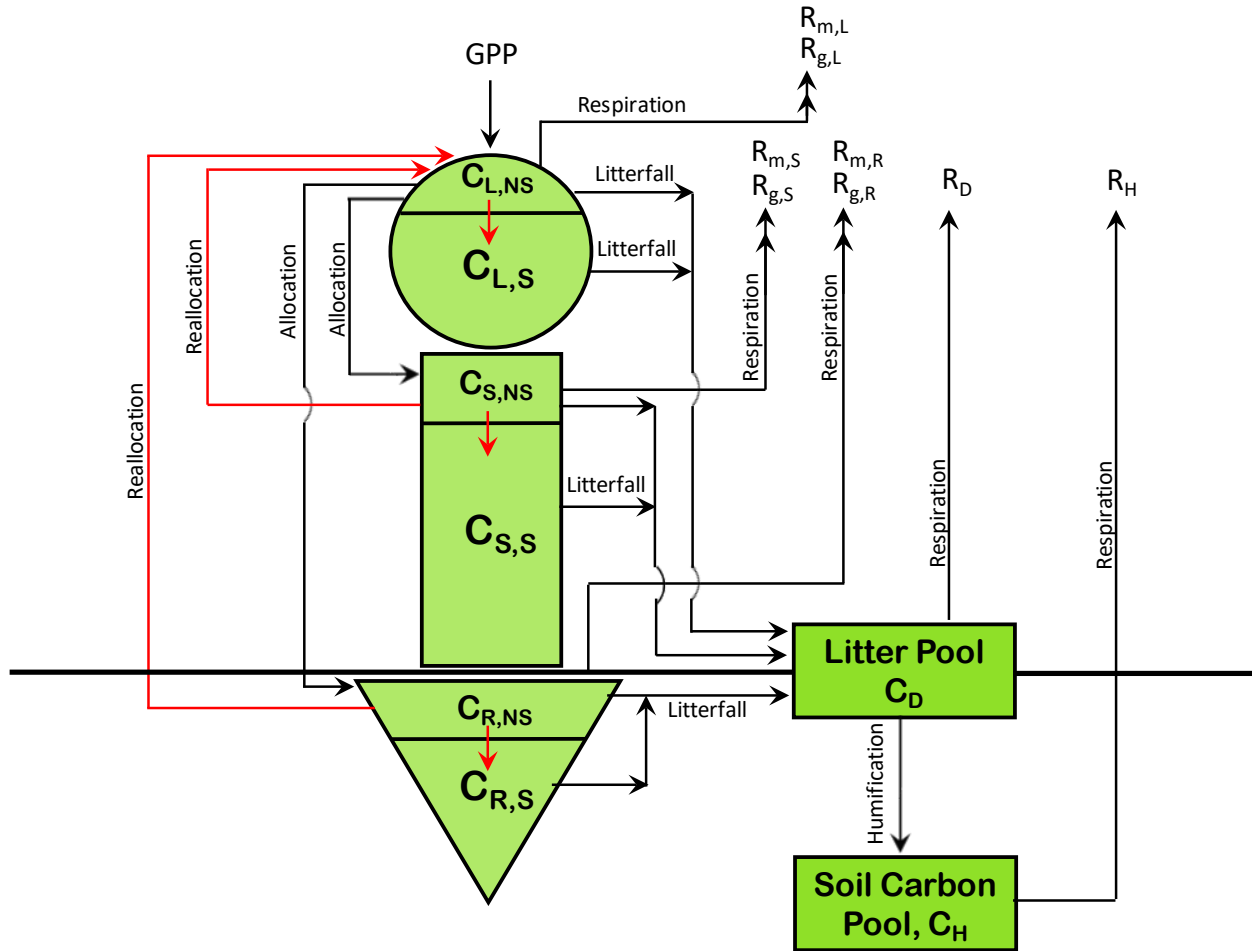
1315

1316

1317 Figure A1: The structure of CLASSIC model used in this study, upon which the N cycle is
1318 implemented, with its carbon pools and fluxes. The fluxes of non-structural carbon are shown in
1319 red colour.

1320

1321

1322

1323

1324

1325
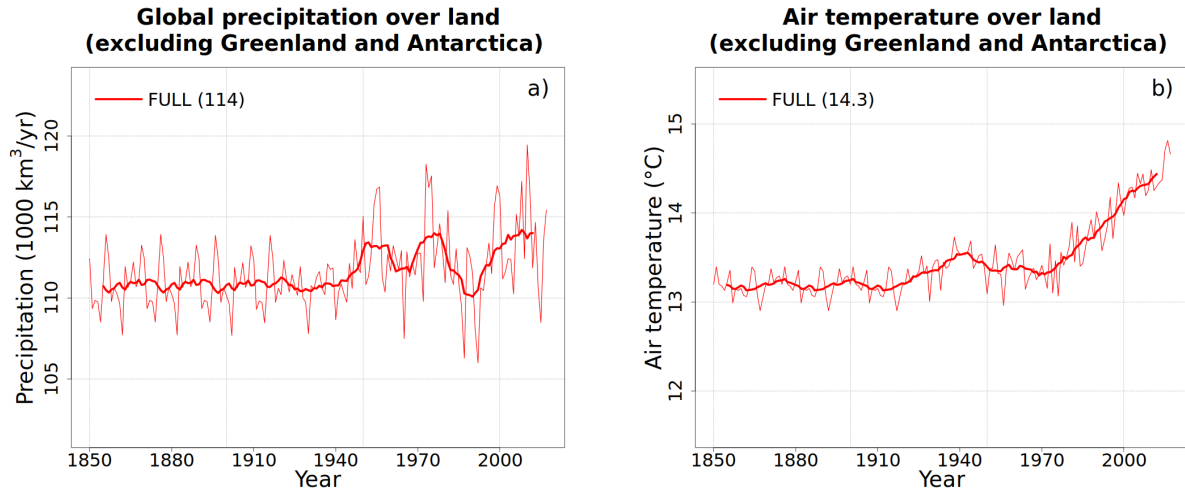
1326

1327

1328   Figure A2: Annual values of global precipitation (a) and air temperature (b) over land in the
1329   CRU-JRA reanalysis data that are used to drive the model. The data are available for the period
1330   1901-2017. In the absence of meterological data, the period 1851-1900 uses the data from the
1331   period 1901-1925 twice. The thin lines are the annual values and the thick line their 10 year
1332   running mean.

1333

1334 **Table A1**: Model parameters for various model parameterizations. Corresponding equation in which the
1335 parameter appears in the main text is also noted. Model parameters may be scalar or an array (if they
1336 are PFT dependent) in which case they are written according to the following structure in the table
1337 below.

Needleleaf evergreen	Needleleaf deciduous	
Broadleaf evergreen	Broadleaf deciduous cold	Broadleaf deciduous drought
C_3 crop	C_4 crop	
C_3 grass	C_4 grass	

1338 .

Model parameter	Eqn	Description	Units	Value(s)		
Biological N fixation						
α_c	3	BNF rate for crop PFTs	gN m^{-2} day^{-1}	0.00217		
α_n	3	BNF rate for natural PFTs	gN m^{-2} day^{-1}	0.00037		
Plant N demand						
$C:N_{L,min}$	4	Minimum C:N ratio for leaves	dimensionless	25 20 16 13	22 18 20 18	18
$C:N_{S,min}$	4	Minimum C:N ratio for stem	dimensionless	450 430 285 –	450 430 285 –	430
$C:N_{R,min}$	4	Minimum C:N ratio for root	dimensionless	45 35 30 30	45 35 35 35	35
Plant uptake						
β	6	Mineral N distribution coefficient	dimensionless	0.5		
ε	8	Fine root efficiency	gN gC^{-1} day^{-1}	4.92E-5		
$k_{p,\frac{1}{2}}$	8	Half saturation constant	gN m^{-3}	3		
Litterfall						
r_L	11	Leaf resorption coefficient	dimensionless	0.54		
Nitrification						
η	19	Nitrification coefficient	day^{-1}	7.33E-4		

Symbol	Eq.	Description	Units	Value
η_{NO}	23	Fraction of nitrification flux emitted as NO	dimensionless	7.03E-5
η_{N2O}	23	Fraction of nitrification flux emitted as N_2O	dimensionless	2.57E-5
Denitrification				
μ_{NO}	24	Fraction of denitrification flux emitted as NO	day^{-1}	3.872E-4
μ_{N2O}	24	Fraction of denitrification flux emitted as N_2O	day^{-1}	1.408E-4
μ_{N2}	24	Fraction of denitrification flux emitted as N_2	day^{-1}	3.872E-3
w_d	24	Soil wetness threshold below which very little denitrification occurs	dimensionless	0.3
Leaching				
φ	26	Leaching coefficient	$m^2\ Kg^{-1}$	1.15E-3
NH_3 volatilization				
ϑ	27	NH_3 volatilization coefficient	dimensionless	0.54
Coupling of C and N cycles				
Γ_1	31	Parameter for calculating V_{cmax} from leaf N content	$\mu mol\ CO_2\ gN^{-1}\ s^{-1}$	13 (all PFTs except broadleaf evergreen tree) 5.1 (for broadleaf evergreen tree)
Γ_2	31	Parameter for calculating V_{cmax} from leaf N content	$\mu mol\ CO_2\ m^{-2}\ s^{-1}$	8.5
k_Λ	32	Parameter for constraining V_{cmax} increase when C:N ratios exceed their maximum limit	dimensionless	0.05
$C:N_{L,max}$	33	Maximum C:N ratio for leaves	dimensionless	60 50 55 40 40 40 50 35 50
$C:N_{S,max}$	33	Maximum C:N ratio for stem	dimensionless	800 800 670 670 670 500 500

				–	–	
$C:N_{R,max}$	33	Maximum C:N ratio for root	dimensionless	90 70 60 60	90 70 70 70	70

1339

1340

1341 **Table 1**: Historical simulations performed over the period 1851-2017 to evaluate the model's
1342 response to various forcings. All forcings are time varying. All forcings are also spatially explicit
1343 except atmospheric CO_2 for which a globally constant value is specified.

1344

Simulation name	Forcing that varies over the historical period	N cycle
Primary simulations performed to evaluate N cycle response to various forcings		
1. CO2-only	Atmospheric CO_2 concentration	Runs with N cycle
2. CLIM-only	1901-1925 meteorological data are used twice over the 1850-1900 period. For the 1901-2017 period, meteorological data for the correct year is used.	
3. LUC+FERT-only	Land cover with increasing crop area, and fertilizer application rates over the crop area	
4. N-DEP-only	N deposition of ammonia and nitrate	
5. FULL	All forcings	
6. FULL-no-LUC	All forcings except increasing crop area	

Other simulations		
7. ORIGINAL	All forcings	Runs without N cycle using the original model configuration.
8. ORIG-UNCONST	All forcings but with downregulation turned off	
9. FULL-no-implicit-P-limitation	All forcings but using same Γ_1 and Γ_2 globally	Run with N cycle

1345

1346

1347

1348 **Table 2**: Comparison of simulated global N pools and fluxes, from the FULL simulation, with other
1349 modelling and quasi observation-based studies (references for which are noted as superscripts
1350 and listed below the table). The time-periods to which the other modelling and quasi
1351 observation-based estimates correspond are also noted, where available. The estimates are for
1352 land. Simulated fluxes and pool corresponds to the period 1997-2018.

1353

N pool and fluxes	This study (1998-2017)	Other model and quasi observation-based estimates
N inputs (Tg N yr^{-1})		
BNF	119	118[a] 99[b] (2001-2010) 138.5[c] (early 1990s) 128.9[d] (2000-2009) 104-118[e] 92[f] (year 2000)
Natural BNF	59	58[a] 107[c] (early 1990s) 30-130[e] 39[f] (year 2000)
Anthropogenic BNF	60	60[a] 31.5[c] (early 1990s) 14-89[e] 53[f] (year 2000)
Fertilizer input	91 (based on TRENDY protocol)	100[a] 100[b] (2001-2010) 100[c] (early 1990s) 83[f] (year 2000)
N deposition	66 (based on TRENDY protocol)	70[a] 56-62[b] 63.5[c] (early 1990s) 69[f] (year 2000)
N pools (Tg N yr^{-1})		
Vegetation	3034	1,780[d] (2000s) 3,800[g] (1990s) 5,300[h] 2,940[i] (1990s)
Litter and soil	77161	106,000[d] (2000s) 100,000[g] (1990s) 56,800[h] 113,000[i] (1990s)
Ammonia	1924	163.7[d] (2000s) 361[h] 1200[i] (1990s)
Nitrate	2974	2,778[d] (2000s) 580[h] 14,800[i] (1990s)
N fluxes related to N cycling (Tg N yr^{-1})		
Plant uptake	940	618[d] (2000s) 1,127[g] (1990s) 1,084[h] 873[i] (1990s)
Net mineralization	947	
Mineralization	2045	1,678[d] (2000s)
Immobilization	1097	1,177[d] (2000s)
Nitrification	239	

N losses (Tg N yr^{-1})			
NO$_3$- Leaching	53.5		97.1[b] (2001-2010) 62.8[d] (2000s) 77.0[g] (1990s)
NH$_3$ Volatilization	53.9		124.9[b] (2001-2010) 52.6[c] (early 1990s) 20.4[d] (2000s)
N$_2$ from denitrification	114.2		105.8[b] (2001-2010) 68[f] (year 2000)
N$_2$O from denitrification	4.2	12.6	8.7[b] (2001-2010) 10.9[c] (early 1990s) 13.0[a]
N$_2$O from nitrification	8.4		
NO from denitrification	11.4	34.3	24.8[c] (early 1990s) 26.8[g] (1990s)
NO from nitrification	22.9		

1354

1355 [a]Fowler et al. (2013), [b]Zaehle (2013), [c]Galloway et al. (2004), [d]von Bloh et al. (2018), [e]Galloway et al.
1356 (2013), [f]Bouwman et al. (2013), [g]Zaehle et al. (2010), [h]Xu-Ri and Prentice (2008), [i]Wania et al. (2012)

1357

1358

1359
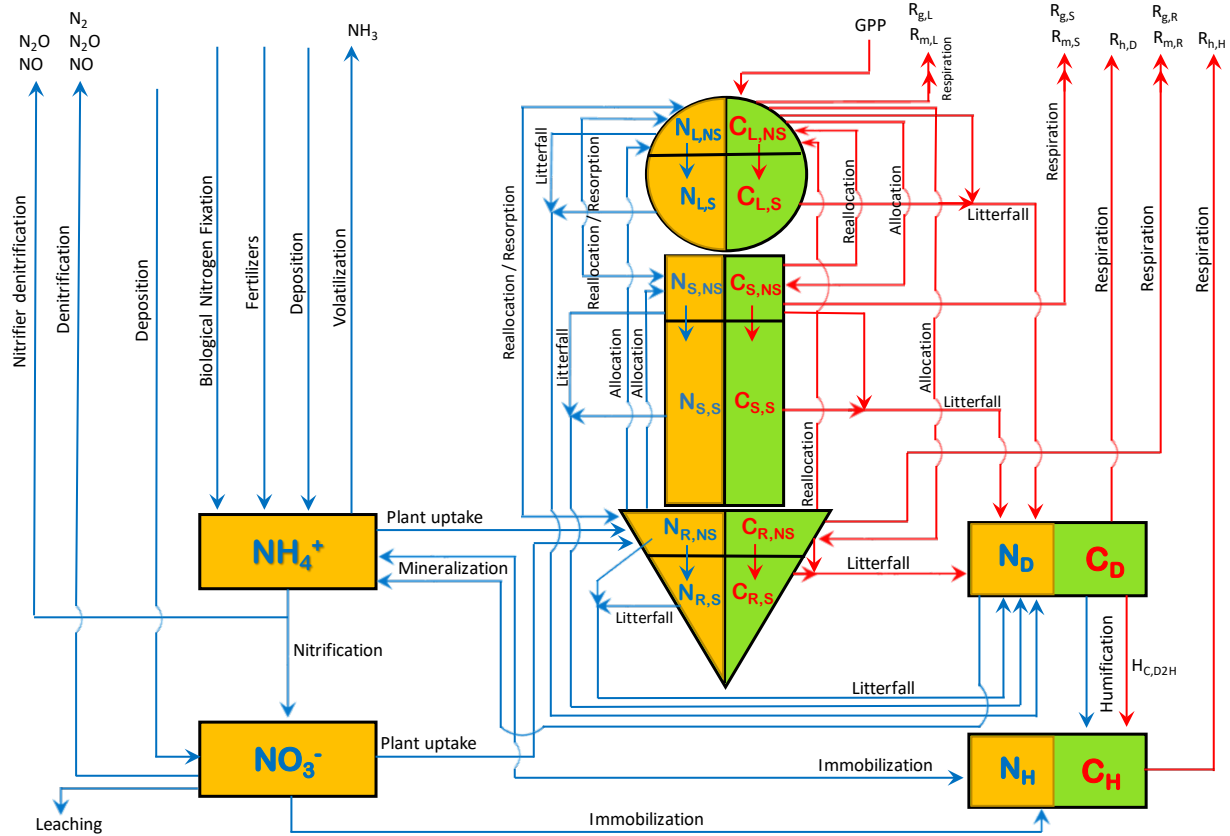
1360

1361 Figure 1: The structure of CLASSIC model used in this study. The eight prognostic carbon pools
1362 are shown in green colour and carbon fluxes in red colour. The ten prognostic nitrogen pools are
1363 shown in orange colour and nitrogen fluxes are shown in blue colour.

1364

1365
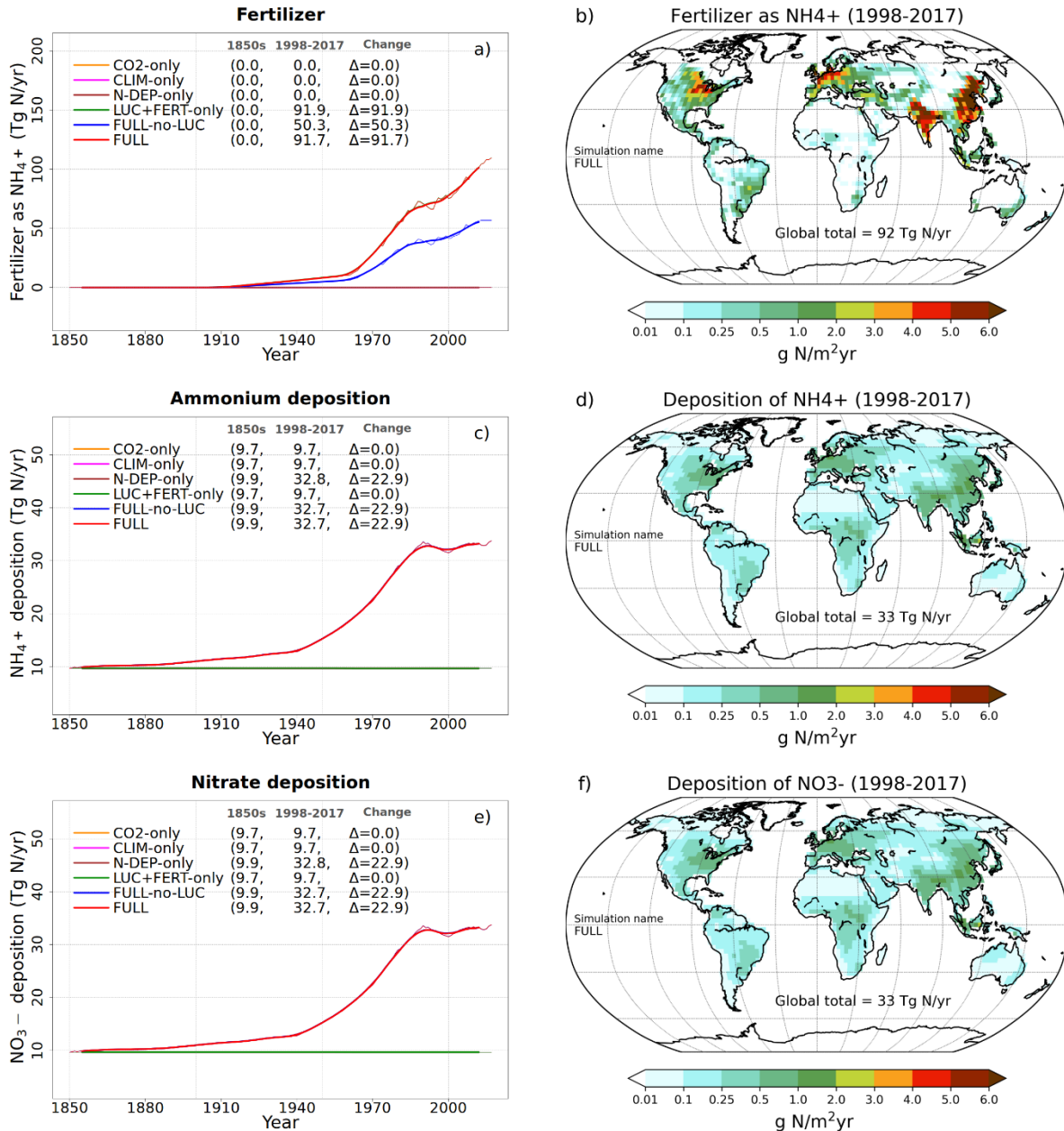
Figure 2: Time series and geographical distribution of global annual values of externally specified N inputs. Fertilizer input (a, b), atmospheric deposition of ammonium (c, d) and atmospheric deposition of nitrate (e, f). The values in the parenthesis for legend entries in the time series plots show averages for the 1850s, the 1998-2017 period, and the change between these two periods. The thin lines in the time series plots show the annual values and the thick lines their 10-year moving average. The geographical plots show the average values over the last 20-years of the FULL simulation corresponding to the 1998-2017 period. Note that in the time series plots lines from some simulations are hidden behind lines from other simulations and this can be inferred from the legend entries which shows averages for the 1850s, the 1998-2017 period.
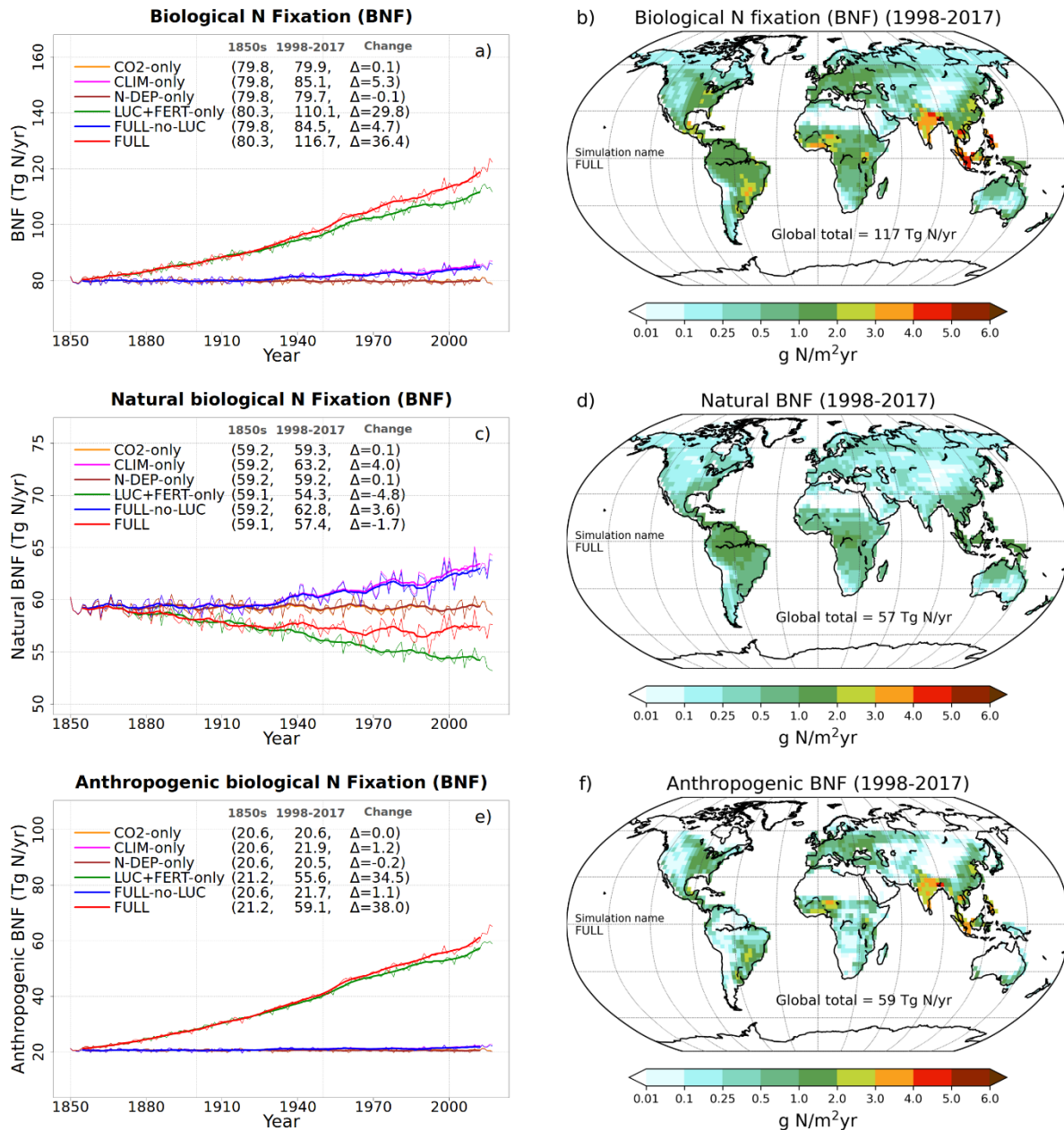
Figure 3: Time series and geographical distribution of annual values biological N fixation (BNF) (a,b) and its natural (c, d) and anthropogenic (e, f) components. The values in the parenthesis for legend entries in the time series plots show averages for the 1850s, the 1998-2017 period, and the change between these two periods. The thin lines in the time series plots show the annual values and the thick lines their 10-year moving average. The geographical plots show the average values over the last 20-years of the FULL simulation corresponding to the 1998-2017 period. Note that in the time series plots lines from some simulations are hidden behind lines from other simulations and this can be inferred from the legend entries which shows averages for the 1850s, the 1998-2017 period.

1385
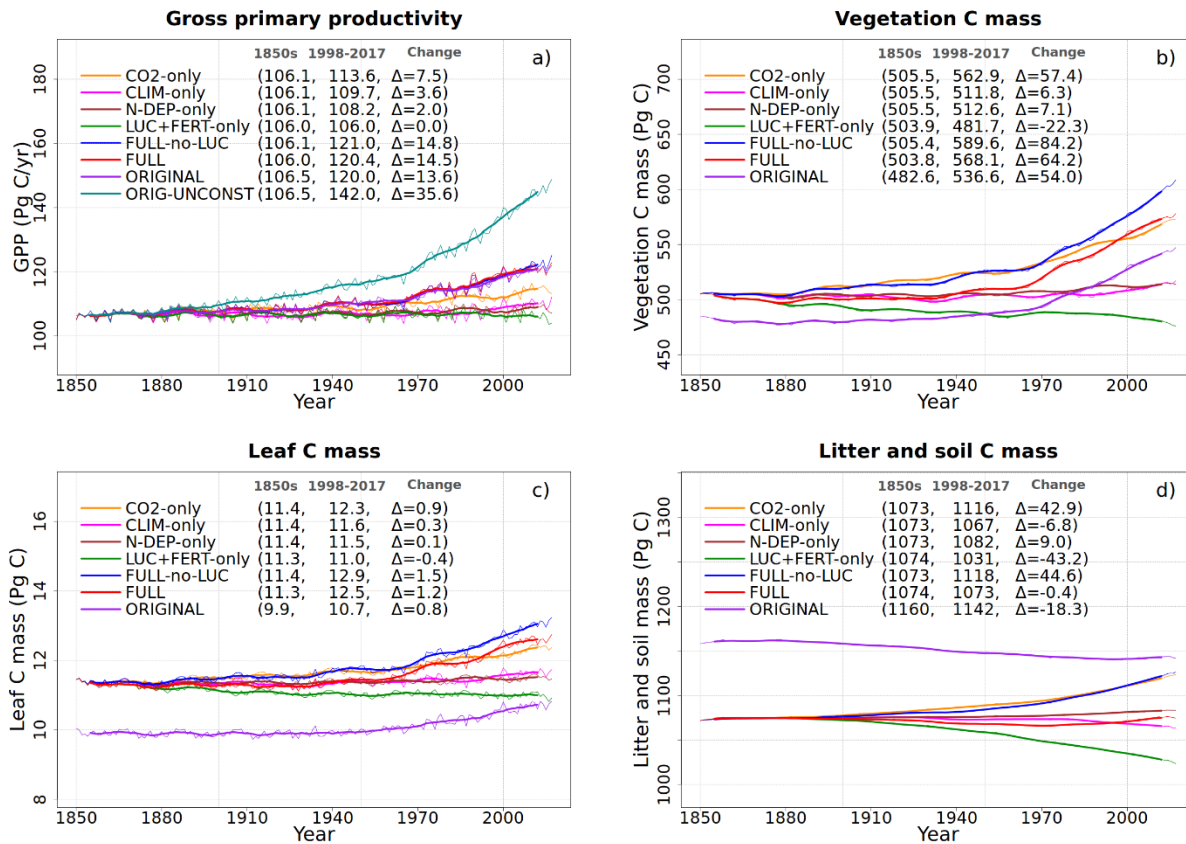
1386

1387   Figure 4: Global annual values of gross primary productivity (a), vegetation carbon (b), leaf
1388   carbon (c), and litter and soil carbon (d) for the primary simulations performed. The values in
1389   the parenthesis for legend entries show averages for the 1850s, the 1998-2017 period, and the
1390   change between 1850s and 1998-2017 periods. The thin lines show the annual values and the
1391   thick lines their 10-year moving average.

1392
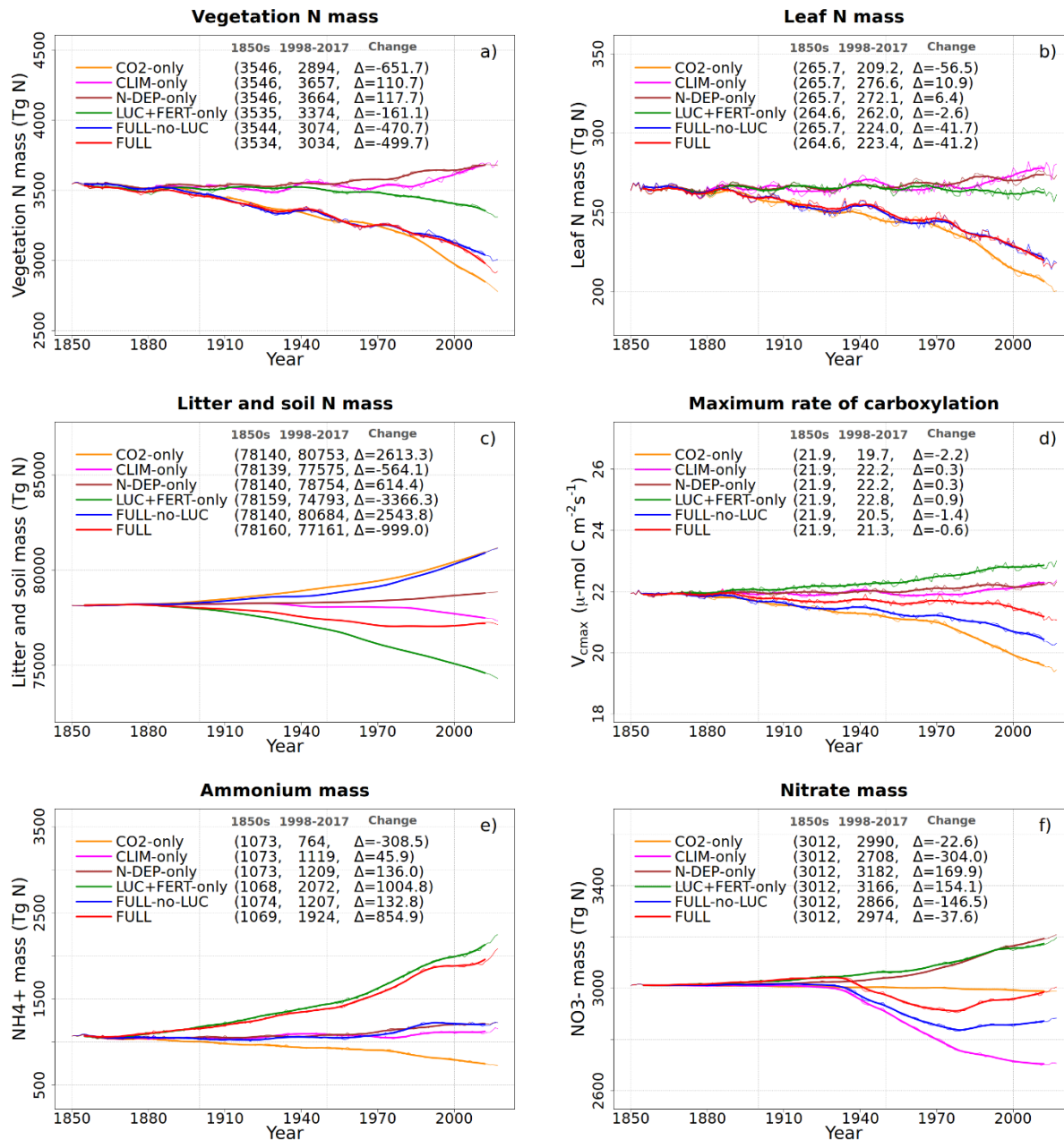
Figure 5: Global annual values of N in vegetation (a), leaves (b), litter and soil organic matter (c) pools, V_{cmax} (d), and ammonium (e), and nitrate (f) pools for the primary simulations performed. The values in the parenthesis for legend entries show averages for the 1850s, the 1998-2017 period, and the change between 1850s and 1998-2017 periods. The thin lines show the annual values and the thick lines their 10-year moving average.
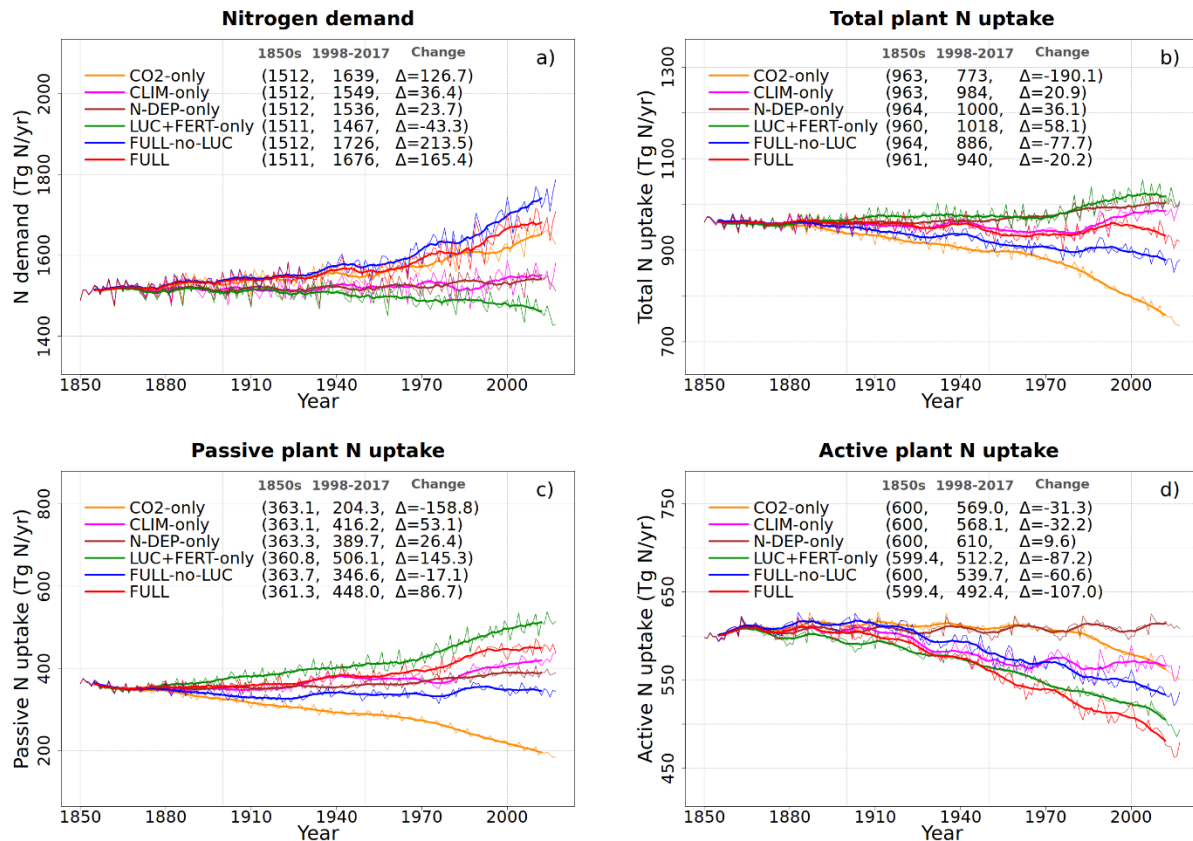
Figure 6: Global annual values of N demand (a), total plant N uptake (b) and its split into passive (c) and active (d) components for the primary simulations performed. The values in the parenthesis for legend entries show averages for the 1850s, the 1998-2017 period, and the change between 1850s and 1998-2017 periods. The thin lines show the annual values and the thick lines their 10-year moving average.

1409
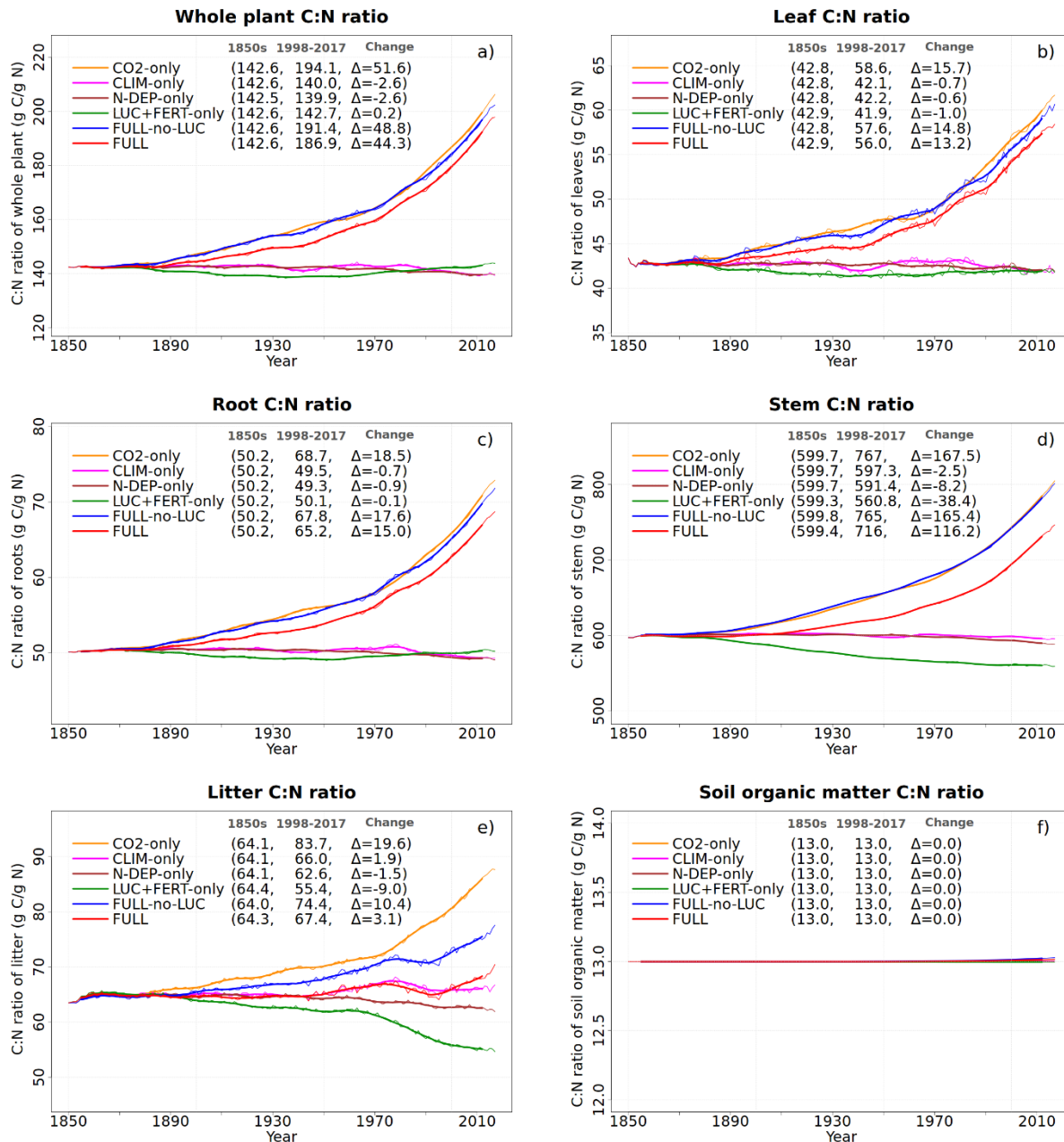
1410

Figure 7: Global annual values of C:N ratios for whole plant (a), leaves (b) , root (c), stem (d), litter (e) and soil organic matter (f) pools from the primary six simulations. The values in the parenthesis for legend entries show averages for the 1850s, the 1998-2017 period, and the change between 1850s and 1998-2017 periods. The thin lines show the annual values and the thick lines their 10-year moving average.

1411
1412
1413
1414
1415

1416

1417
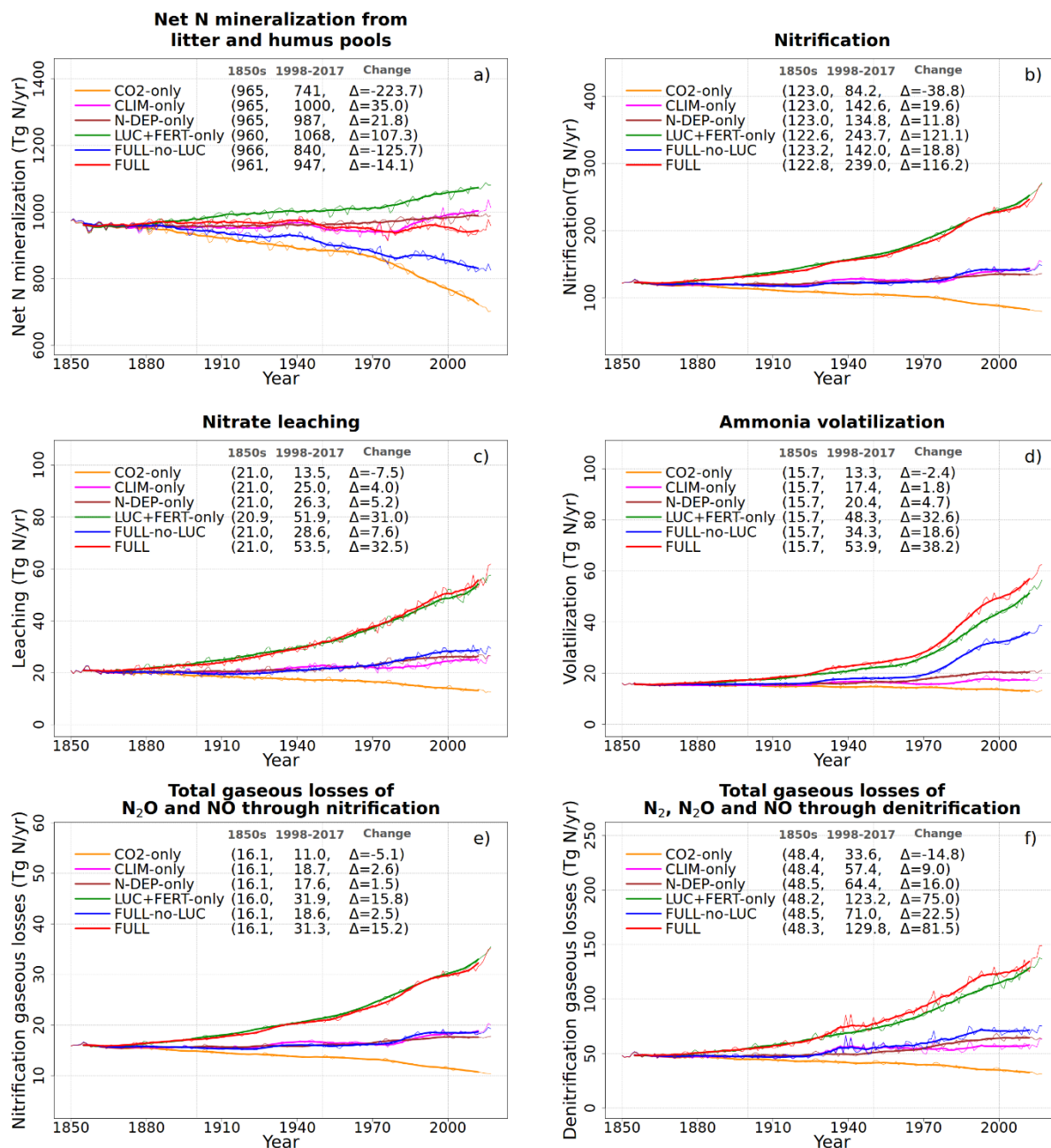
1418

Figure 8: Global annual values of net mineralization (a), nitrification (b), NO_3^- leaching (c), NH_3 volatilization (d), and gaseous losses associated with nitrification (e) and denitrification (f) from the primary six simulations. The values in the parenthesis for legend entries show averages for the 1850s, the 1998-2017 period, and the change between 1850s and 1998-2017 periods. The thin lines show the annual values and the thick lines their 10-year moving average.

1424
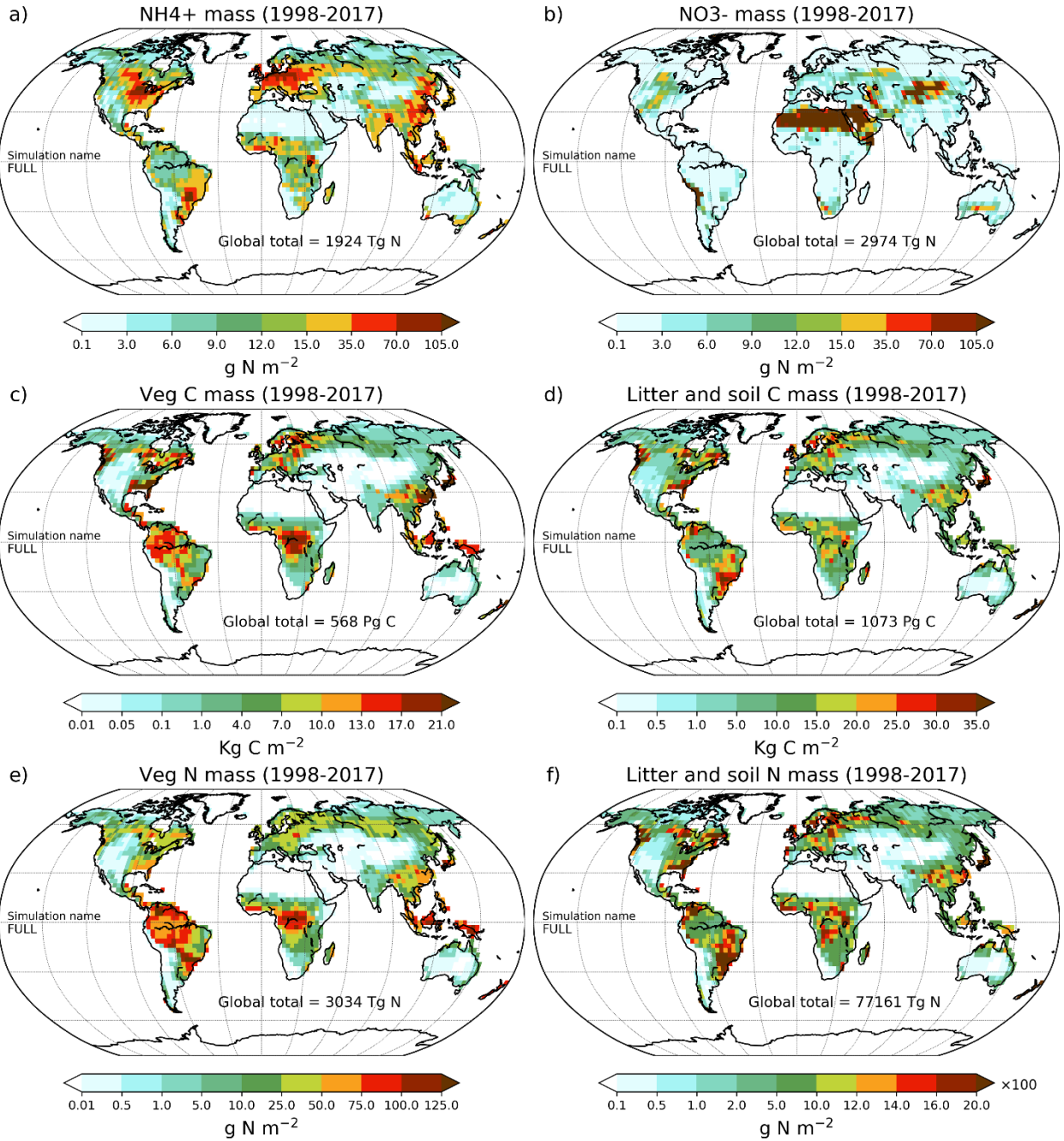
1425

Figure 9: Geographical distribution of primary C and N pools. Ammonium (a), nitrate (b),
vegetation C mass (c), litter and soil C mass (d), vegetation N mass (e), and litter and soil N mass
(f). The global total values shown are averaged over the 1998-2017 period.

1429

1430

1431
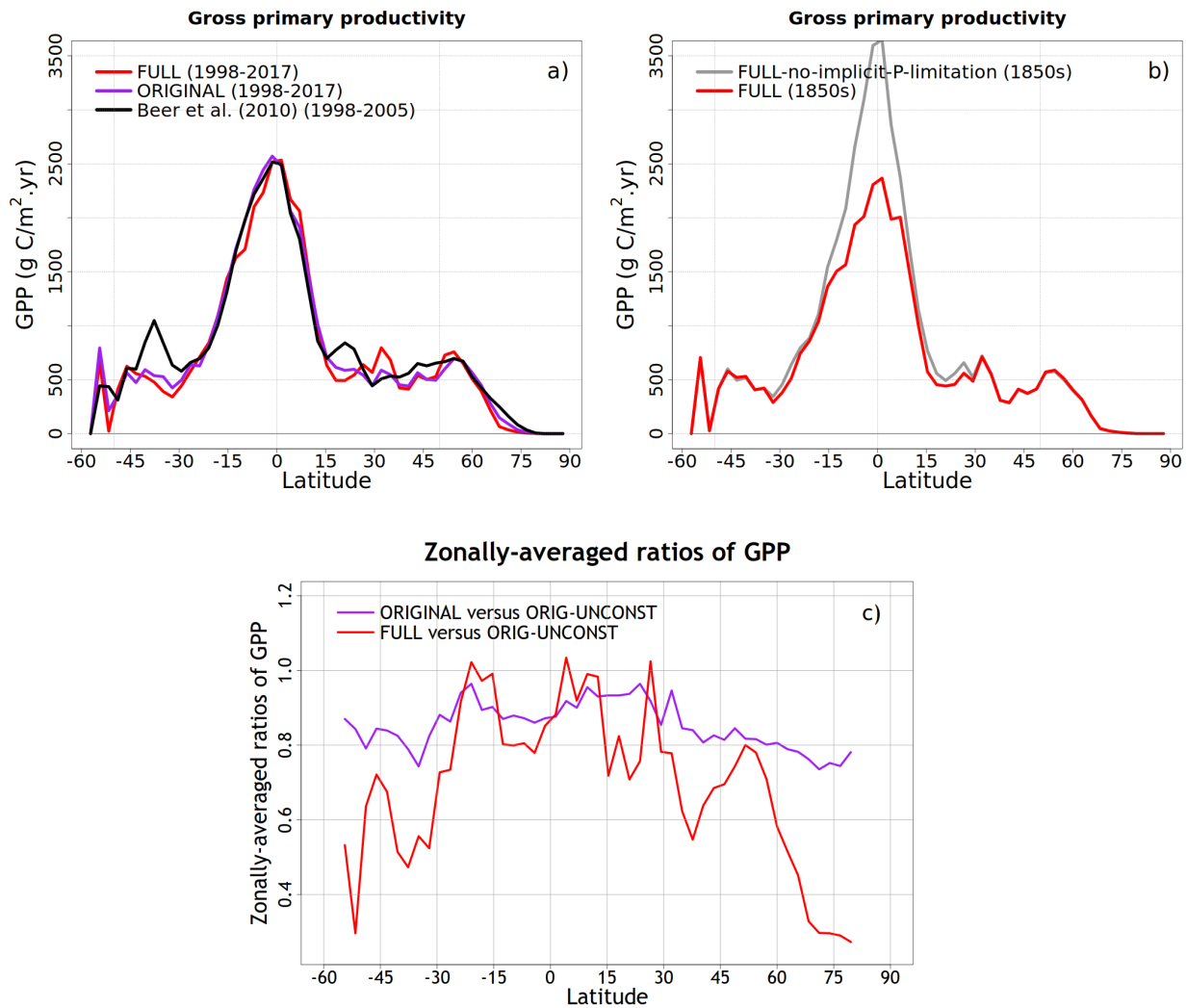
Figure 10: Comparison of zonal distribution of gross primary productivity (GPP) and the effect of GPP downregulation compared to the ORIG-UNCONST simulation. Panel (a) compares zonal distribution of GPP from FULL and ORIGINAL simulations with observation-based estimate from Beer at al. (2010) for the present day. Panel (b) compares the zonal distribution of GPP from the pre-industrial simulation, corresponding to 1850 conditions, from the FULL and FULL-no-implicit-P-limitation simulations to illustrate the effect of not reducing the Γ_1 parameter for calculating V_{cmax} for the broadleaf evergreen tree PFT that implicitly accounts for phosphorus limitation. Panel (c) shows the zonally-averaged ratios of GPP from the ORIGINAL and FULL simulations versus those from the ORIG-UNCONST simulations to illustrate how downregulation acts in the ORIGINAL and FULL simulations.

1442

1443
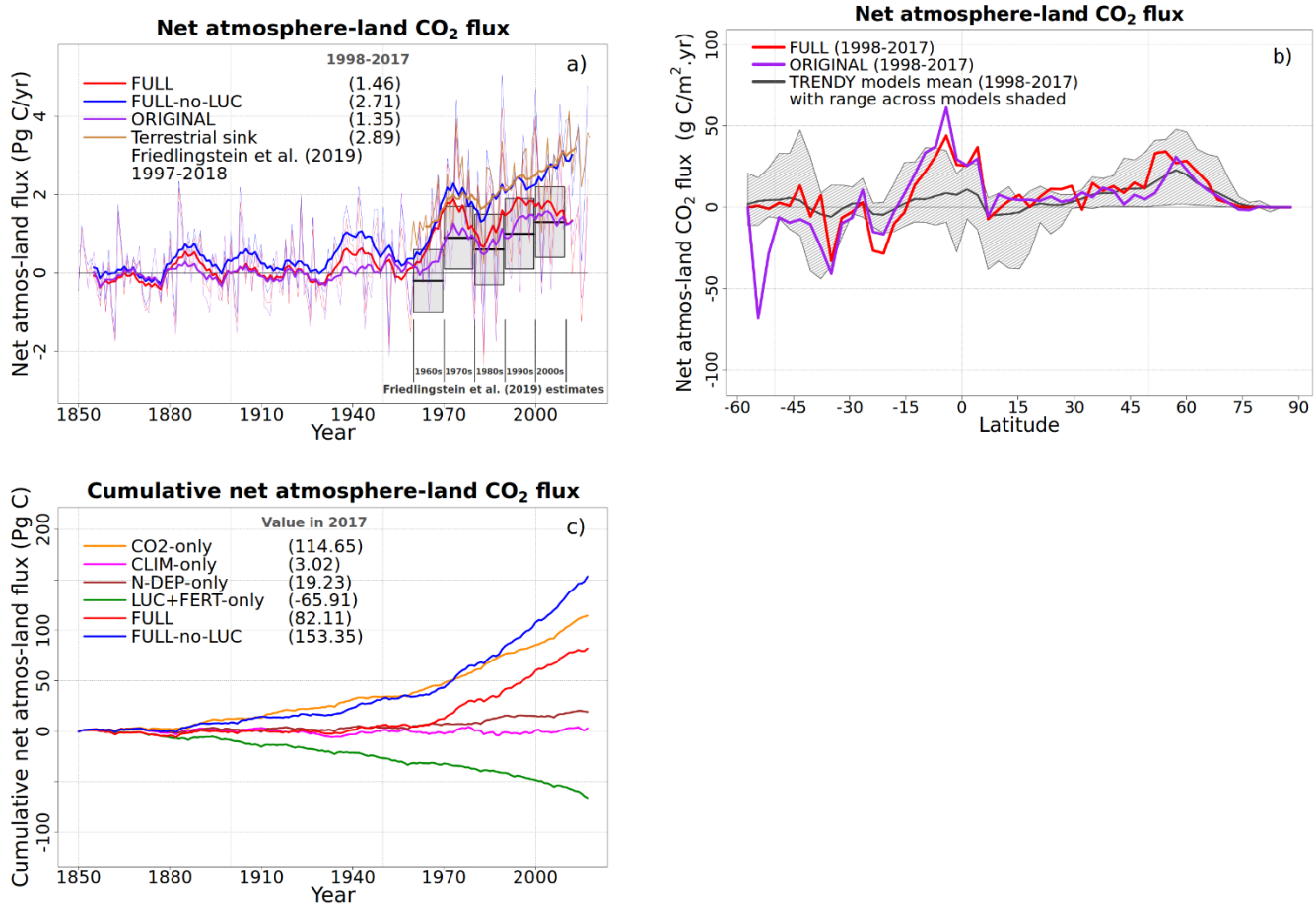
1444

1445 Figure 11: Comparison of simulated net atmosphere-land CO_2 flux from various simulations.

1446 Panel (a) compares globally-summed values of net atmosphere-land CO_2 flux from FULL, FULL-

1447 no-LUC simulation, and ORIGINAL simulations with estimate of terrestrial sink (dark yellow line)

1448 and net atmosphere-land CO2 flux (grey bars) from Friedlingstein et al. (2019). The thin lines

1449 show the annual values and the thick lines their 10-year moving average. Panel (b) compares

1450 zonal distribution of net atmosphere-land CO_2 flux from FULL and ORIGINAL simulations with

1451 the range from TRENDY models that contributed to the Friedlingstein et al. (2019) study. Panel

1452 (c) shows cumulative values of net atmosphere-land CO_2 flux from the six primary simulations

1453 to investigate the contribution of each forcing to the cumulative land carbon sink over the

1454 historical period.

1455

References

1456

1457 Alexandrov, G. and Oikawa, T.: TsuBiMo: a biosphere model of the CO2-fertilization effect, Clim. Res.,
1458 19(3), 265–270, 2002.

1459 Aragão, L. E. O. C., Malhi, Y., Metcalfe, D. B., Silva-Espejo, J. E., Jiménez, E., Navarrete, D., Almeida, S.,
1460 Costa, A. C. L., Salinas, N., Phillips, O. L., Anderson, L. O., Alvarez, E., Baker, T. R., Goncalvez, P. H.,
1461 Huamán-Ovalle, J., Mamani-Solórzano, M., Meir, P., Monteagudo, A., Patiño, S., Peñuela, M. C., Prieto,
1462 A., Quesada, C. A., Rozas-Dávila, A., Rudas, A., Silva Jr., J. A. and Vásquez, R.: Above- and below-ground
1463 net primary productivity across ten Amazonian forests on contrasting soils, Biogeosciences, 6(12), 2759–
1464 2778, doi:10.5194/bg-6-2759-2009, 2009.

1465 Arneth, A., Harrison, S. P., Zaehle, S., Tsigaridis, K., Menon, S., Bartlein, P. J., Feichter, J., Korhola, A.,
1466 Kulmala, M., O'Donnell, D., Schurgers, G., Sorvari, S. and Vesala, T.: Terrestrial biogeochemical feedbacks
1467 in the climate system, Nat. Geosci., 3(8), 525–532, doi:10.1038/ngeo905, 2010.

1468 Arora, V. K.: Simulating energy and carbon fluxes over winter wheat using coupled land surface and
1469 terrestrial ecosystem models, Agric. For. Meteorol., 118(1), 21–47, doi:https://doi.org/10.1016/S0168-
1470 1923(03)00073-X, 2003.

1471 Arora, V. K. and Boer, G. J.: A Representation of Variable Root Distribution in Dynamic Vegetation
1472 Models, Earth Interact., 7(6), 1–19, doi:10.1175/1087-3562(2003)007<0001:AROVRD>2.0.CO;2, 2003.

1473 Arora, V. K. and Boer, G. J.: A parameterization of leaf phenology for the terrestrial ecosystem
1474 component of climate models, Glob. Change Biol., 11(1), 39–59, doi:10.1111/j.1365-2486.2004.00890.x,
1475 2005.

1476 Arora, V. K. and Boer, G. J.: Uncertainties in the 20th century carbon budget associated with land use
1477 change, Glob. Change Biol., 16(12), 3327–3348, doi:10.1111/j.1365-2486.2010.02202.x, 2010.

1478 Arora, V. K. and Melton, J. R.: Reduction in global area burned and wildfire emissions since 1930s
1479 enhances carbon uptake by land, Nat. Commun., 9(1), 1326, doi:10.1038/s41467-018-03838-0, 2018.

1480 Arora, V. K., Boer, G. J., Christian, J. R., Curry, C. L., Denman, K. L., Zahariev, K., Flato, G. M., Scinocca, J.
1481 F., Merryfield, W. J. and Lee, W. G.: The Effect of Terrestrial Photosynthesis Down Regulation on the
1482 Twentieth-Century Carbon Budget Simulated with the CCCma Earth System Model, J. Clim., 22(22),
1483 6066–6088, doi:10.1175/2009JCLI3037.1, 2009.

1484 Arora, V. K., Scinocca, J. F., Boer, G. J., Christian, J. R., Denman, K. L., Flato, G. M., Kharin, V. V., Lee, W. G.
1485 and Merryfield, W. J.: Carbon emission limits required to satisfy future representative concentration
1486 pathways of greenhouse gases, Geophys. Res. Lett., 38(5), doi:10.1029/2010GL046270, 2011.

1487 Arora, V. K., Boer, G. J., Friedlingstein, P., Eby, M., Jones, C. D., Christian, J. R., Bonan, G., Bopp, L.,
1488 Brovkin, V., Cadule, P., Hajima, T., Ilyina, T., Lindsay, K., Tjiputra, J. F. and Wu, T.: Carbon–Concentration
1489 and Carbon–Climate Feedbacks in CMIP5 Earth System Models, J. Clim., 26(15), 5289–5314,
1490 doi:10.1175/JCLI-D-12-00494.1, 2013.

1491 Arora, V. K., Katavouta, A., Williams, R. G., Jones, C. D., Brovkin, V., Friedlingstein, P., Schwinger, J., Bopp,
1492 L., Boucher, O., Cadule, P., Chamberlain, M. A., Christian, J. R., Delire, C., Fisher, R. A., Hajima, T., Ilyina,

1493   T., Joetzjer, E., Kawamiya, M., Koven, C. D., Krasting, J. P., Law, R. M., Lawrence, D. M., Lenton, A.,
1494   Lindsay, K., Pongratz, J., Raddatz, T., Séférian, R., Tachiiri, K., Tjiputra, J. F., Wiltshire, A., Wu, T. and
1495   Ziehn, T.: Carbon–concentration and carbon–climate feedbacks in CMIP6 models and their comparison
1496   to CMIP5 models, Biogeosciences, 17(16), 4173–4222, doi:10.5194/bg-17-4173-2020, 2020.

1497   Asaadi, A., Arora, V. K., Melton, J. R. and Bartlett, P.: An improved parameterization of leaf area index
1498   (LAI) seasonality in the Canadian Land Surface Scheme (CLASS) and Canadian Terrestrial Ecosystem
1499   Model (CTEM) modelling framework, Biogeosciences, 15(22), 6885–6907, doi:10.5194/bg-15-6885-2018,
1500   2018.

1501   Bauerle, W. L., Oren, R., Way, D. A., Qian, S. S., Stoy, P. C., Thornton, P. E., Bowden, J. D., Hoffman, F. M.
1502   and Reynolds, R. F.: Photoperiodic regulation of the seasonal pattern of photosynthetic capacity and the
1503   implications for carbon cycling, Proc. Natl. Acad. Sci., 109(22), 8612–8617,
1504   doi:10.1073/pnas.1119131109, 2012.

1505   Beer, C., Reichstein, M., Tomelleri, E., Ciais, P., Jung, M., Carvalhais, N., Rödenbeck, C., Arain, M. A.,
1506   Baldocchi, D., Bonan, G. B., Bondeau, A., Cescatti, A., Lasslop, G., Lindroth, A., Lomas, M., Luyssaert, S.,
1507   Margolis, H., Oleson, K. W., Roupsard, O., Veenendaal, E., Viovy, N., Williams, C., Woodward, F. I. and
1508   Papale, D.: Terrestrial Gross Carbon Dioxide Uptake: Global Distribution and Covariation with Climate,
1509   Science, 329(5993), 834–838, 2010.

1510   von Bloh, W., Schaphoff, S., Müller, C., Rolinski, S., Waha, K. and Zaehle, S.: Implementing the nitrogen
1511   cycle into the dynamic global vegetation, hydrology, and crop growth model LPJmL (version 5.0), Geosci.
1512   Model Dev., 11(7), 2789–2812, doi:10.5194/gmd-11-2789-2018, 2018.

1513   Bouwman, A. F., Beusen, A. H. W., Griffioen, J., Van Groenigen, J. W., Hefting, M. M., Oenema, O., Van
1514   Puijenbroek, P. J. T. M., Seitzinger, S., Slomp, C. P. and Stehfest, E.: Global trends and uncertainties in
1515   terrestrial denitrification and N2O emissions, Philos. Trans. R. Soc. B Biol. Sci., 368(1621), 20130112,
1516   doi:10.1098/rstb.2013.0112, 2013.

1517   Cao, M., Zhang, Q. and Shugart, H. H.: Dynamic responses of African ecosystem carbon cycling to climate
1518   change, Clim. Res., 17(2), 183–193, 2001.

1519   Clapp, R. B. and Hornberger, G. M.: Empirical equations for some soil hydraulic properties, Water
1520   Resour. Res., 14(4), 601–604, doi:10.1029/WR014i004p00601, 1978.

1521   Cleveland, C. C., Townsend, A. R., Schimel, D. S., Fisher, H., Howarth, R. W., Hedin, L. O., Perakis, S. S.,
1522   Latty, E. F., Von Fischer, J. C., Elseroad, A. and Wasson, M. F.: Global patterns of terrestrial biological
1523   nitrogen (N2) fixation in natural ecosystems, Glob. Biogeochem. Cycles, 13(2), 623–645,
1524   doi:10.1029/1999GB900014, 1999.

1525   Collatz, G., Ribas-Carbo, M. and Berry, J.: Coupled Photosynthesis-Stomatal Conductance Model for
1526   Leaves of C4 Plants, Funct. Plant Biol., 19(5), 519–538, 1992.

1527   Cotrufo, M. F., Ineson, P. and Scott, AndY.: Elevated CO2 reduces the nitrogen concentration of plant
1528   tissues, Glob. Change Biol., 4(1), 43–54, doi:10.1046/j.1365-2486.1998.00101.x, 1998.

1529 Croft, H., Chen, J. M., Luo, X., Bartlett, P., Chen, B. and Staebler, R. M.: Leaf chlorophyll content as a
1530 proxy for leaf photosynthetic capacity, Glob. Change Biol., 23(9), 3513–3524, doi:10.1111/gcb.13599,
1531 2017.

1532 Du, E., Terrer, C., Pellegrini, A. F. A., Ahlström, A., van Lissa, C. J., Zhao, X., Xia, N., Wu, X. and Jackson, R.
1533 B.: Global patterns of terrestrial nitrogen and phosphorus limitation, Nat. Geosci., 13(3), 221–226,
1534 doi:10.1038/s41561-019-0530-4, 2020.

1535 Evans, J. R.: Photosynthesis and nitrogen relationships in leaves of C3 plants, Oecologia, 78(1), 9–19,
1536 doi:10.1007/BF00377192, 1989.

1537 Eyring, V., Bony, S., Meehl, G. A., Senior, C. A., Stevens, B., Stouffer, R. J. and Taylor, K. E.: Overview of
1538 the Coupled Model Intercomparison Project Phase 6 (CMIP6) experimental design and organization,
1539 Geosci. Model Dev., 9(5), 1937–1958, doi:10.5194/gmd-9-1937-2016, 2016.

1540 Faria, T., Wilkins, D., Besford, R. T., Vaz, M., Pereira, J. S. and Chaves, M. M.: Growth at elevated CO2
1541 leads to down-regulation of photosynthesis and altered response to high temperature in Quercus suber
1542 L. seedlings, J. Exp. Bot., 47(11), 1755–1761, doi:10.1093/jxb/47.11.1755, 1996.

1543 Farquhar, G. D., von Caemmerer, S. and Berry, J. A.: A biochemical model of photosynthetic CO2
1544 assimilation in leaves of C3 species, Planta, 149(1), 78–90, doi:10.1007/BF00386231, 1980.

1545 Field, C. and Mooney, H.: The Photosynthesis-Nitrogen Relationship in Wild Plants, Biol. Int., 13, 25–56,
1546 1986.

1547 Fisher, J. B., Sitch, S., Malhi, Y., Fisher, R. A., Huntingford, C. and Tan, S.-Y.: Carbon cost of plant nitrogen
1548 acquisition: A mechanistic, globally applicable model of plant nitrogen uptake, retranslocation, and
1549 fixation: CARBON COST OF PLANT N ACQUISITION, Glob. Biogeochem. Cycles, 24(1), n/a-n/a,
1550 doi:10.1029/2009GB003621, 2010.

1551 Fowler, D., Coyle, M., Skiba, U., Sutton, M. A., Cape, J. N., Reis, S., Sheppard, L. J., Jenkins, A., Grizzetti,
1552 B., Galloway, J. N., Vitousek, P., Leach, A., Bouwman, A. F., Butterbach-Bahl, K., Dentener, F., Stevenson,
1553 D., Amann, M. and Voss, M.: The global nitrogen cycle in the twenty-first century, Philos. Trans. R. Soc. B
1554 Biol. Sci., 368(1621), 20130164, doi:10.1098/rstb.2013.0164, 2013.

1555 Friedlingstein, P., Cox, P., Betts, R., Bopp, L., von Bloh, W., Brovkin, V., Cadule, P., Doney, S., Eby, M.,
1556 Fung, I., Bala, G., John, J., Jones, C., Joos, F., Kato, T., Kawamiya, M., Knorr, W., Lindsay, K., Matthews, H.
1557 D., Raddatz, T., Rayner, P., Reick, C., Roeckner, E., Schnitzler, K.-G., Schnur, R., Strassmann, K., Weaver,
1558 A. J., Yoshikawa, C. and Zeng, N.: Climate–Carbon Cycle Feedback Analysis: Results from the C4MIP
1559 Model Intercomparison, J. Clim., 19(14), 3337–3353, doi:10.1175/JCLI3800.1, 2006.

1560 Friedlingstein, P., Jones, M. W., O'Sullivan, M., Andrew, R. M., Hauck, J., Peters, G. P., Peters, W.,
1561 Pongratz, J., Sitch, S., Le Quéré, C., Bakker, D. C. E., Canadell, J. G., Ciais, P., Jackson, R. B., Anthoni, P.,
1562 Barbero, L., Bastos, A., Bastrikov, V., Becker, M., Bopp, L., Buitenhuis, E., Chandra, N., Chevallier, F.,
1563 Chini, L. P., Currie, K. I., Feely, R. A., Gehlen, M., Gilfillan, D., Gkritzalis, T., Goll, D. S., Gruber, N.,
1564 Gutekunst, S., Harris, I., Haverd, V., Houghton, R. A., Hurtt, G., Ilyina, T., Jain, A. K., Joetzjer, E., Kaplan, J.
1565 O., Kato, E., Klein Goldewijk, K., Korsbakken, J. I., Landschützer, P., Lauvset, S. K., Lefèvre, N., Lenton, A.,
1566 Lienert, S., Lombardozzi, D., Marland, G., McGuire, P. C., Melton, J. R., Metzl, N., Munro, D. R., Nabel, J.
1567 E. M. S., Nakaoka, S.-I., Neill, C., Omar, A. M., Ono, T., Peregon, A., Pierrot, D., Poulter, B., Rehder, G.,

1568   Resplandy, L., Robertson, E., Rödenbeck, C., Séférian, R., Schwinger, J., Smith, N., Tans, P. P., Tian, H.,
1569   Tilbrook, B., Tubiello, F. N., van der Werf, G. R., Wiltshire, A. J. and Zaehle, S.: Global Carbon Budget
1570   2019, Earth Syst. Sci. Data, 11(4), 1783–1838, doi:10.5194/essd-11-1783-2019, 2019.

1571   Galloway, J. N., Dentener, F. J., Capone, D. G., Boyer, E. W., Howarth, R. W., Seitzinger, S. P., Asner, G. P.,
1572   Cleveland, C. C., Green, P. A., Holland, E. A., Karl, D. M., Michaels, A. F., Porter, J. H., Townsend, A. R. and
1573   Vöosmarty, C. J.: Nitrogen Cycles: Past, Present, and Future, Biogeochemistry, 70(2), 153–226,
1574   doi:10.1007/s10533-004-0370-0, 2004.

1575   Galloway, J. N., Leach, A. M., Bleeker, A. and Erisman, J. W.: A chronology of human understanding of
1576   the nitrogen cycle[†], Philos. Trans. R. Soc. B Biol. Sci., 368(1621), 20130120,
1577   doi:10.1098/rstb.2013.0120, 2013.

1578   Garnier, E., Salager, J.-L., Laurent, G. and Sonie, L.: Relationships between photosynthesis, nitrogen and
1579   leaf structure in 14 grass species and their dependence on the basis of expression, New Phytol., 143(1),
1580   119–129, doi:10.1046/j.1469-8137.1999.00426.x, 1999.

1581   Gerber, S., Hedin, L. O., Oppenheimer, M., Pacala, S. W. and Shevliakova, E.: Nitrogen cycling and
1582   feedbacks in a global dynamic land model, Glob. Biogeochem. Cycles, 24(1),
1583   doi:10.1029/2008GB003336, 2010.

1584   Goll, D. S., Brovkin, V., Parida, B. R., Reick, C. H., Kattge, J., Reich, P. B., van Bodegom, P. M. and
1585   Niinemets, Ü.: Nutrient limitation reduces land carbon uptake in simulations with a model of combined
1586   carbon, nitrogen and phosphorus cycling, Biogeosciences, 9(9), 3547–3569, doi:10.5194/bg-9-3547-
1587   2012, 2012.

1588   Goyal, S. S. and Huffaker, R. C.: Nitrogen toxicity in plants, in Nitrogen in Crop Production, pp. 97–118,
1589   American Society of Agronomy, Madison, WI., 1984.

1590   Hungate, B. A., Dukes, J. S., Shaw, M. R., Luo, Y. and Field, C. B.: Nitrogen and Climate Change, Science,
1591   302(5650), 1512–1513, doi:10.1126/science.1091390, 2003.

1592   Hurtt, G. C., Frolking, S., Fearon, M. G., Moore, B., Shevliakova, E., Malyshev, S., Pacala, S. W. and
1593   Houghton, R. A.: The underpinnings of land-use history: three centuries of global gridded land-use
1594   transitions, wood-harvest activity, and resulting secondary lands, Glob. Change Biol., 12(7), 1208–1229,
1595   doi:10.1111/j.1365-2486.2006.01150.x, 2006.

1596   Jiang, M., Zaehle, S., De Kauwe, M. G., Walker, A. P., Caldararu, S., Ellsworth, D. S. and Medlyn, B. E.: The
1597   quasi-equilibrium framework revisited: analyzing long-term CO2 enrichment responses in plant–soil
1598   models, Geosci. Model Dev., 12(5), 2069–2089, doi:10.5194/gmd-12-2069-2019, 2019.

1599   Jones, A. G., Scullion, J., Ostle, N., Levy, P. E. and Gwynn-Jones, D.: Completing the FACE of elevated CO2
1600   research, Environ. Int., 73, 252–258, doi:https://doi.org/10.1016/j.envint.2014.07.021, 2014.

1601   Jones, C. D., Arora, V., Friedlingstein, P., Bopp, L., Brovkin, V., Dunne, J., Graven, H., Hoffman, F., Ilyina,
1602   T., John, J. G., Jung, M., Kawamiya, M., Koven, C., Pongratz, J., Raddatz, T., Randerson, J. T. and Zaehle,
1603   S.: C4MIP – The Coupled Climate–Carbon Cycle Model Intercomparison Project: experimental protocol
1604   for CMIP6, Geosci. Model Dev., 9(8), 2853–2880, doi:10.5194/gmd-9-2853-2016, 2016.

1605   Kattge, J., Knorr, W., Raddatz, T. and Wirth, C.: Quantifying photosynthetic capacity and its relationship
1606   to leaf nitrogen content for global-scale terrestrial biosphere models, Glob. Change Biol., 15(4), 976–
1607   991, doi:10.1111/j.1365-2486.2008.01744.x, 2009.

1608   Klein Goldewijk, K., Beusen, A., Doelman, J. and Stehfest, E.: Anthropogenic land use estimates for the
1609   Holocene – HYDE 3.2, Earth Syst. Sci. Data, 9(2), 927–953, doi:10.5194/essd-9-927-2017, 2017.

1610   Köchy, M., Hiederer, R. and Freibauer, A.: Global distribution of soil organic carbon – Part 1: Masses and
1611   frequency distributions of SOC stocks for the tropics, permafrost regions, wetlands, and the world, SOIL,
1612   1(1), 351–365, doi:10.5194/soil-1-351-2015, 2015.

1613   Kurz, W. A., Beukema, S. J. and Apps, M. J.: Estimation of root biomass and dynamics for the carbon
1614   budget model of the Canadian forest sector, Can. J. For. Res., 26(11), 1973–1979, doi:10.1139/x26-223,
1615   1996.

1616   Le Quéré, C., Andrew, R. M., Friedlingstein, P., Sitch, S., Hauck, J., Pongratz, J., Pickers, P. A., Korsbakken,
1617   J. I., Peters, G. P., Canadell, J. G., Arneth, A., Arora, V. K., Barbero, L., Bastos, A., Bopp, L., Chevallier, F.,
1618   Chini, L. P., Ciais, P., Doney, S. C., Gkritzalis, T., Goll, D. S., Harris, I., Haverd, V., Hoffman, F. M.,
1619   Hoppema, M., Houghton, R. A., Hurtt, G., Ilyina, T., Jain, A. K., Johannessen, T., Jones, C. D., Kato, E.,
1620   Keeling, R. F., Goldewijk, K. K., Landschützer, P., Lefèvre, N., Lienert, S., Liu, Z., Lombardozzi, D., Metzl,
1621   N., Munro, D. R., Nabel, J. E. M. S., Nakaoka, S., Neill, C., Olsen, A., Ono, T., Patra, P., Peregon, A., Peters,
1622   W., Peylin, P., Pfeil, B., Pierrot, D., Poulter, B., Rehder, G., Resplandy, L., Robertson, E., Rocher, M.,
1623   Rödenbeck, C., Schuster, U., Schwinger, J., Séférian, R., Skjelvan, I., Steinhoff, T., Sutton, A., Tans, P. P.,
1624   Tian, H., Tilbrook, B., Tubiello, F. N., van der Laan-Luijkx, I. T., van der Werf, G. R., Viovy, N., Walker, A.
1625   P., Wiltshire, A. J., Wright, R., Zaehle, S. and Zheng, B.: Global Carbon Budget 2018, Earth Syst. Sci. Data,
1626   10(4), 2141–2194, doi:10.5194/essd-10-2141-2018, 2018.

1627   Leith, H.: Modeling the primary productivity of the world, in Primary Productivity of the Biosphere (H.
1628   Leith and R. H. Whittaker, Eds.), pp. 237–263, Springer-Verlag, Berlin and New York., 1975.

1629   Li, H., Crabbe, M., Xu, F., Wang, W., Niu, R., Gao, X., Zhang, P. and Chen, H.: Seasonal Variations in
1630   Carbon, Nitrogen and Phosphorus Concentrations and C:N:P Stoichiometry in the Leaves of Differently
1631   Aged Larix principis-rupprechtii Mayr. Plantations, Forests, 8(10), 373, doi:10.3390/f8100373, 2017.

1632   Liang, J., Qi, X., Souza, L. and Luo, Y.: Processes regulating progressive nitrogen limitation under elevated
1633   carbon dioxide: a meta-analysis, Biogeosciences, 13(9), 2689–2699, doi:10.5194/bg-13-2689-2016, 2016.

1634   Lin, B.-L., Sakoda, A., Shibasaki, R., Goto, N. and Suzuki, M.: Modelling a global biogeochemical nitrogen
1635   cycle in terrestrial ecosystems, Ecol. Model., 135(1), 89–110, doi:https://doi.org/10.1016/S0304-
1636   3800(00)00372-0, 2000.

1637   Manzoni, S., Jackson, R. B., Trofymow, J. A. and Porporato, A.: The Global Stoichiometry of Litter
1638   Nitrogen Mineralization, Science, 321(5889), 684–686, doi:10.1126/science.1159792, 2008.

1639   McGuire, A. D., Melillo, J. M. and Joyce, L. A.: The role of nitrogen in the response of forests net primary
1640   production to elevated atmospheric carbon dioxide, Annu. Rev. Ecol. Syst., 26(1), 473–503,
1641   doi:10.1146/annurev.es.26.110195.002353, 1995.

1642 Melton, J. R. and Arora, V. K.: Competition between plant functional types in the Canadian Terrestrial
1643 Ecosystem Model (CTEM) v. 2.0, Geosci Model Dev, 9(1), 323–361, doi:10.5194/gmd-9-323-2016, 2016.

1644 Melton, J. R., Shrestha, R. K. and Arora, V. K.: The influence of soils on heterotrophic respiration exerts a
1645 strong control on net ecosystem productivity in seasonally dry Amazonian forests, Biogeosciences, 12(4),
1646 1151–1168, doi:10.5194/bg-12-1151-2015, 2015.

1647 Melton, J. R., Arora, V. K., Wisernig-Cojoc, E., Seiler, C., Fortier, M., Chan, E. and Teckentrup, L.: CLASSIC
1648 v1.0: the open-source community successor to the Canadian Land Surface Scheme (CLASS) and the
1649 Canadian Terrestrial Ecosystem Model (CTEM) – Part 1: Model framework and site-level performance,
1650 Geosci. Model Dev. Discuss., 2019, 1–40, doi:10.5194/gmd-2019-329, 2019.

1651 Meyerholt, J., Zaehle, S. and Smith, M. J.: Variability of projected terrestrial biosphere responses to
1652 elevated levels of atmospheric CO2 due to uncertainty in biological nitrogen fixation, Biogeosciences,
1653 13(5), 1491–1518, doi:10.5194/bg-13-1491-2016, 2016.

1654 Ochoa-Hueso, R., Maestre, F. T., Ríos, A. [de los, Valea, S., Theobald, M. R., Vivanco, M. G., Manrique, E.
1655 and Bowker, M. A.: Nitrogen deposition alters nitrogen cycling and reduces soil carbon content in low-
1656 productivity semiarid Mediterranean ecosystems, Environ. Pollut., 179, 185–193,
1657 doi:https://doi.org/10.1016/j.envpol.2013.03.060, 2013.

1658 O'Hara, G. W.: The Role of Nitrogen Fixation in Crop Production, J. Crop Prod., 1(2), 115–138,
1659 doi:10.1300/J144v01n02_05, 1998.

1660 Porporato, A., D'Odorico, P., Laio, F. and Rodriguez-Iturbe, I.: Hydrologic controls on soil carbon and
1661 nitrogen cycles. I. Modeling scheme, Adv. Water Resour., 26(1), 45–58,
1662 doi:https://doi.org/10.1016/S0309-1708(02)00094-5, 2003.

1663 Rastetter, E. B., Vitousek, P. M., Field, C., Shaver, G. R., Herbert, D. and gren, G. I.: Resource Optimization
1664 and Symbiotic Nitrogen Fixation, Ecosystems, 4(4), 369–388, doi:10.1007/s10021-001-0018-z, 2001.

1665 Reich, P. B., Hungate, B. A. and Luo, Y.: Carbon-Nitrogen Interactions in Terrestrial Ecosystems in
1666 Response to Rising Atmospheric Carbon Dioxide, Annu. Rev. Ecol. Evol. Syst., 37(1), 611–636,
1667 doi:10.1146/annurev.ecolsys.37.091305.110039, 2006a.

1668 Reich, P. B., Hobbie, S. E., Lee, T., Ellsworth, D. S., West, J. B., Tilman, D., Knops, J. M. H., Naeem, S. and
1669 Trost, J.: Nitrogen limitation constrains sustainability of ecosystem response to CO2, Nature, 440(7086),
1670 922–925, doi:10.1038/nature04486, 2006b.

1671 Riddick, S., Ward, D., Hess, P., Mahowald, N., Massad, R. and Holland, E.: Estimate of changes in
1672 agricultural terrestrial nitrogen pathways and ammonia emissions from 1850 to present in
1673 the\hack\newline Community Earth System Model, Biogeosciences, 13(11), 3397–3426, doi:10.5194/bg-
1674 13-3397-2016, 2016.

1675 Salvagiotti, F., Cassman, K. G., Specht, J. E., Walters, D. T., Weiss, A. and Dobermann, A.: Nitrogen
1676 uptake, fixation and response to fertilizer N in soybeans: A review, Field Crops Res., 108(1), 1–13,
1677 doi:https://doi.org/10.1016/j.fcr.2008.03.001, 2008.

1678 Sanz-Sáez, Á., Erice, G., Aranjuelo, I., Nogués, S., Irigoyen, J. J. and Sánchez-Díaz, M.: Photosynthetic
1679 down-regulation under elevated CO2 exposure can be prevented by nitrogen supply in nodulated alfalfa,
1680 J. Plant Physiol., 167(18), 1558–1565, doi:https://doi.org/10.1016/j.jplph.2010.06.015, 2010.

1681 Still, C. J., Berry, J. A., Collatz, G. J. and DeFries, R. S.: Global distribution of C3 and C4 vegetation: Carbon
1682 cycle implications, Glob. Biogeochem. Cycles, 17(1), 6–1, doi:10.1029/2001GB001807, 2003.

1683 Swart, N. C., Cole, J. N. S., Kharin, V. V., Lazare, M., Scinocca, J. F., Gillett, N. P., Anstey, J., Arora, V.,
1684 Christian, J. R., Hanna, S., Jiao, Y., Lee, W. G., Majaess, F., Saenko, O. A., Seiler, C., Seinen, C., Shao, A.,
1685 Sigmond, M., Solheim, L., von Salzen, K., Yang, D. and Winter, B.: The Canadian Earth System Model
1686 version 5 (CanESM5.0.3), Geosci. Model Dev., 12(11), 4823–4873, doi:10.5194/gmd-12-4823-2019,
1687 2019.

1688 Thom, A. S.: Momentum, mass and heat exchange of plant communities, in Vegetation and the
1689 atmosphere, Vol. 1, Principles, edited by Monteith, J. L., Academic Press, London., 1975.

1690 Thornton, P. E., Lamarque, J.-F., Rosenbloom, N. A. and Mahowald, N. M.: Influence of carbon-nitrogen
1691 cycle coupling on land model response to CO2 fertilization and climate variability, Glob. Biogeochem.
1692 Cycles, 21(4), doi:10.1029/2006GB002868, 2007.

1693 Tian, H., Yang, J., Lu, C., Xu, R., Canadell, J. G., Jackson, R. B., Arneth, A., Chang, J., Chen, G., Ciais, P.,
1694 Gerber, S., Ito, A., Huang, Y., Joos, F., Lienert, S., Messina, P., Olin, S., Pan, S., Peng, C., Saikawa, E.,
1695 Thompson, R. L., Vuichard, N., Winiwarter, W., Zaehle, S., Zhang, B., Zhang, K. and Zhu, Q.: The Global
1696 N2O Model Intercomparison Project, Bull. Am. Meteorol. Soc., 99(6), 1231–1251, doi:10.1175/BAMS-D-
1697 17-0212.1, 2018.

1698 Tipping, E., Somerville, C. J. and Luster, J.: The C:N:P:S stoichiometry of soil organic matter,
1699 Biogeochemistry, 130(1), 117–131, doi:10.1007/s10533-016-0247-z, 2016.

1700 Tomasek, A., Kozarek, J. L., Hondzo, M., Lurndahl, N., Sadowsky, M. J., Wang, P. and Staley, C.:
1701 Environmental drivers of denitrification rates and denitrifying gene abundances in channels and riparian
1702 areas, Water Resour. Res., 53(8), 6523–6538, doi:10.1002/2016WR019566, 2017.

1703 Verseghy, D. L.: Class—A Canadian land surface scheme for GCMS. I. Soil model, Int. J. Climatol., 11(2),
1704 111–133, doi:10.1002/joc.3370110202, 1991.

1705 Verseghy, D. L., McFarlane, N. A. and Lazare, M.: Class—A Canadian land surface scheme for GCMS, II.
1706 Vegetation model and coupled runs, Int. J. Climatol., 13(4), 347–370, doi:10.1002/joc.3370130402,
1707 1993.

1708 Vitousek, P. M.: Litterfall, Nutrient Cycling, and Nutrient Limitation in Tropical Forests, Ecology, 65(1),
1709 285–298, doi:10.2307/1939481, 1984.

1710 Vitousek, P. M.: Beyond Global Warming: Ecology and Global Change, Ecology, 75(7), 1861–1876,
1711 doi:10.2307/1941591, 1994.

1712 Vitousek, P. M. and Howarth, R. W.: Nitrogen limitation on land and in the sea: How can it occur?,
1713 Biogeochemistry, 13(2), 87–115, doi:10.1007/BF00002772, 1991.

1714 Vitousek, P. M., Porder, S., Houlton, B. Z. and Chadwick, O. A.: Terrestrial phosphorus limitation:
1715 mechanisms, implications, and nitrogen–phosphorus interactions, Ecol. Appl., 20(1), 5–15,
1716 doi:10.1890/08-0127.1, 2010.

1717 Vitousek, P. M., Menge, D. N. L., Reed, S. C. and Cleveland, C. C.: Biological nitrogen fixation: rates,
1718 patterns and ecological controls in terrestrial ecosystems, Philos. Trans. R. Soc. B Biol. Sci., 368(1621),
1719 20130119, doi:10.1098/rstb.2013.0119, 2013.

1720 Wang, J., Liu, X., Zhang, X., Li, L., Lam, S. K. and Pan, G.: Changes in plant C, N and P ratios under elevated
1721 [CO2] and canopy warming in a rice-winter wheat rotation system, Sci. Rep., 9(1), 5424,
1722 doi:10.1038/s41598-019-41944-1, 2019.

1723 Wania, R., Meissner, K. J., Eby, M., Arora, V. K., Ross, I. and Weaver, A. J.: Carbon-nitrogen feedbacks in
1724 the UVic ESCM, Geosci. Model Dev., 5(5), 1137–1160, doi:10.5194/gmd-5-1137-2012, 2012.

1725 Wei, X., Shao, M., Gale, W. and Li, L.: Global pattern of soil carbon losses due to the conversion of
1726 forests to agricultural land, Sci. Rep., 4, 4062, 2014.

1727 Wiltshire, A. J., Burke, E. J., Chadburn, S. E., Jones, C. D., Cox, P. M., Davies-Barnard, T., Friedlingstein, P.,
1728 Harper, A. B., Liddicoat, S., Sitch, S. A. and Zaehle, S.: JULES-CN: a coupled terrestrial Carbon-Nitrogen
1729 Scheme (JULES vn5.1), Geosci. Model Dev. Discuss., 2020, 1–40, doi:10.5194/gmd-2020-205, 2020.

1730 Xu-Ri and Prentice, I. C.: Terrestrial nitrogen cycle simulation with a dynamic global vegetation model,
1731 Glob. Change Biol., 14(8), 1745–1764, doi:10.1111/j.1365-2486.2008.01625.x, 2008.

1732 Zaehle, S.: Terrestrial nitrogen and carbon cycle interactions at the global scale, Philos. Trans. R. Soc. B
1733 Biol. Sci., 368(1621), 20130125, doi:10.1098/rstb.2013.0125, 2013.

1734 Zaehle, S. and Friend, A. D.: Carbon and nitrogen cycle dynamics in the O-CN land surface model: 1.
1735 Model description, site-scale evaluation, and sensitivity to parameter estimates: SITE-SCALE
1736 EVALUATION OF A C-N MODEL, Glob. Biogeochem. Cycles, 24(1), n/a-n/a, doi:10.1029/2009GB003521,
1737 2010.

1738 Zaehle, S., Friend, A. D., Friedlingstein, P., Dentener, F., Peylin, P. and Schulz, M.: Carbon and nitrogen
1739 cycle dynamics in the O-CN land surface model: 2. Role of the nitrogen cycle in the historical terrestrial
1740 carbon balance: NITROGEN EFFECTS ON GLOBAL C CYCLING, Glob. Biogeochem. Cycles, 24(1), n/a-n/a,
1741 doi:10.1029/2009GB003522, 2010.

1742 Zeng, H., Jia, G. and Epstein, H.: Recent changes in phenology over the northern high latitudes detected
1743 from multi-satellite data, Environ. Res. Lett., 6(4), 045508, 2011.

1744 Zhang, H., Goll, D. S., Manzoni, S., Ciais, P., Guenet, B. and Huang, Y.: Modeling the effects of litter
1745 stoichiometry and soil mineral N availability on soil organic matter formation using CENTURY-CUE (v1.0),
1746 Geosci. Model Dev., 11(12), 4779–4796, doi:10.5194/gmd-11-4779-2018, 2018.

1747 Zhao, X., Yang, Y., Shen, H., Geng, X. and Fang, J.: Global soil–climate–biome diagram: linking surface soil
1748 properties to climate and biota, Biogeosciences, 16(14), 2857–2871, doi:10.5194/bg-16-2857-2019,
1749 2019.

1750 Zhu, Z., Piao, S., Myneni, R. B., Huang, M., Zeng, Z., Canadell, J. G., Ciais, P., Sitch, S., Friedlingstein, P.,
1751 Arneth, A., Cao, C., Cheng, L., Kato, E., Koven, C., Li, Y., Lian, X., Liu, Y., Liu, R., Mao, J., Pan, Y., Peng, S.,
1752 Penuelas, J., Poulter, B., Pugh, T. A. M., Stocker, B. D., Viovy, N., Wang, X., Wang, Y., Xiao, Z., Yang, H.,
1753 Zaehle, S. and Zeng, N.: Greening of the Earth and its drivers, Nat. Clim Change, 6(8), 791–795, 2016.

1754 Zinke, P. J., Stangenberger, A. G., Post, W. M., Emanuel, W. R. and Olson, J. S.: Global Organic Soil
1755 Carbon and Nitrogen, Tech. Rep. ORNL/TM-8857, Oak Ridge National Laboratory, Oak Ridge, Tennessee,
1756 USA. [online] Available from: https://doi.org/10.3334/ORNLDAAC/221, 1998.

1757

1758

1759